OLD DOMINION UNIVERSITY RESEARCH FOUNDATION

DEPARTMENT OF PHYSICS
SCHOOL OF SCIENCES AND HEALTH PROFESSIONS
OLD DOMINION UNIVERSITY
NORFOLK, VIRGINIA

Technical Report PTR-81-1

RADIATION STUDIES OF OPTICAL AND ELECTRONIC COMPONENTS USED IN ASTRONOMICAL SATELLITE STUDIES

By

Jacob Becher, Principal Investigator

and

R.L. Kernell, Coinvestigator

Final Report
For the period ending July 31, 1980

Prepared for the
National Aeronautics and Space Administration
Goddard Space Flight Center
Greenbelt, Maryland

Under
Research Grant NSG 5053
Dr. Thomas N. Kelsall, Technical Monitor
Science Directorate, Code 603

January 1981

DEPARTMENT OF PHYSICS
SCHOOL OF SCIENCES AND HEALTH PROFESSIONS
OLD DOMINION UNIVERSITY
NORFOLK, VIRGINIA

Technical Report PTR-81-1

RADIATION STUDIES OF OPTICAL AND ELECTRONIC COMPONENTS USED IN ASTRONOMICAL SATELLITE STUDIES

By

Jacob Becher, Principal Investigator

and

R.L. Kernell, Coinvestigator

Final Report
For the period ending July 31, 1980

Prepared for the
National Aeronautics and Space Administration
Goddard Space Flight Center
Greenbelt, Maryland 20771

Under
Research Grant NSG 5053
Dr. Thomas N. Kelsall, Technical Monitor
Science Directorate, Code 603

Submitted by the
Old Dominion University Research Foundation
P.O. Box 6369
Norfolk, Virginia 23508

January 1981

TABLE OF CONTENTS

TABLE OF CONTENTS - CONCLUDED

LIST OF TABLES

LIST OF FIGURES

LIST OF FIGURES - CONTINUED

LIST OF FIGURES - CONCLUDED

RADIATION STUDIES OF OPTICAL AND ELECTRONIC COMPONENTS USED IN ASTRONOMICAL SATELLITE STUDIES

By

Jacob Becher[1] and R.L. Kernell[2]

INTRODUCTION

This report discusses work performed under National Aeronautics and Space Administration (NASA) grant NSG 5053 involving radiation studies of electro-optical components used in satellite astronomy, with particular emphasis on the International Ultraviolet Explorer (IUE). A previous analysis for the IUE project (see Boeing Report No. D180-18486-1), which used radiation models as the basis for shielding calculations, indicated the need for experimental testing of components in a radiation environment simulating a typical orbit. In performing these irradiations, we used radioactive sources in our laboratory and particle accelerators at the Space Radiations Effects Laboratory (SREL), Goddard Space Flight Center (GSFC), and the University of Maryland. The synchronous orbit of the IUE carries the satellite through Earth's outer electron belt. We used a 40-mCi ^{90}Sr source, which we calibrated at the National Bureau of Standards, to simulate these electrons. A 5-mCi source of ^{60}Co was used to simulate bremmstrahlung. The 10-MeV electron Linac at SREL and the 1.7-MeV electron Van de Graaff at GSFC were used to investigate the energy dependence of radiation effects and to perform radiations at a high flux rate. The 100-MeV proton cyclotron at the University of Maryland was used to simulate cosmic rays.

This report first presents results for three instrument systems of the IUE and then reports measurements for specific components. The three instrument systems for which results are reported are the ultraviolet converter, the fine error sensor (FES), and the SEC vidicon camera tube.

---

[1]Associate Professor, Department of Physics, Old Dominion University, Norfolk, Virginia 23508.

[2]Professor, Department of Physics, Old Dominion University, Norfolk, Virginia 23508.

Components for which measurements are reported are optical glasses, electronic components, silicon photodiodes, and UV window materials.

ULTRAVIOLET CONVERTER

Description

In a rather standard configuration, the first component encountered by photons incident on a UV sensor is a converter which transforms the UV photon into a photon of a longer wavelength. This conversion increases the efficiency of detection by a photomultiplier tube or other detecting device to which the converter is coupled. We have investigated three proximity focused UV converters, one of which had been flight tested for use on the IUE satellite. These converters, which are also called image intensifiers, consist of a MgF_2 input window, CsTe photocathode, aluminum antihalation layer, P11 phosphor (Ag activated ZnS), and a fiber optic output window. A UV photon incident on the photocathode produces a photoelectron which is then accelerated through a potential of several kV before impinging on the phosphor. The accelerating potential amplifies the signal by virtue of the fact that several photons are produced by each photoelectron incident on the phosphor.

The weak signals which the UV converter is designed to detect may be masked by background radiation which can activate the UV converter and produce a false output. The possibility of electron-induced luminescence in the UV converter is of specific interest to the IUE project because the IUE's spectrographs use as sensors a converter/SEC compound system and because the IUE orbit passes through Earth's outer electron belt. We present results obtained with a ^{90}Sr button, with a 3.5-MeV Linac electron beam, and then with a Van de Graaff beam ranging from 0.5 to 1.6 MeV. These results show that a significant noise signal occurs when the converter is bombarded with electrons.

Experimental Results

Figure 1 shows the experimental arrangement used in a darkened room to irradiate the UV converter with electrons from a 40-mCi ^{90}Sr source. The various experiments consisted of exposing the converter to radiation

and measuring the light output of the converter's phosphor. The detectors used to measure the light output were the Pritchard photometer, RCA 931A, 1P21, and 1P28, and ITT FW130 photomultiplier tubes. Data were taken using a number of different linear arrangements of figure 1. Configuration A consisted of the 40-mCi source, the UV converter, and a PMT. Configurations B and C were the same as A except that a thin aluminum foil was placed between the converter and the PMT in B while in C the aluminum foil was positioned between the converter and the ^{90}Sr source. The essential difference between these two configurations is that the aluminum foil in B does not permit the photon output from the converter to strike the PMT. This permitted us to distinguish between a PMT current due to photons from the UV converter and a PMT current associated with direct electron irradiation of the PMT. For each of the three configurations the voltage to the converter could be on or off. The difference in the on and off results permitted us to distinguish between a radiation-induced yield resulting from direct excitation of the phosphor and a yield associated with radiation-induced emission from the CsTe photocathode. The distance between the electron source and converter was fixed at 3.5 cm so as to give approximately the flux (2×10^7 e/cm^2-sec) expected in the IUE's passage through Earth's outer electron belt.

The first UV converter investigated was Bendix model No. BX 8025-441-344 operated at 6 kV and coupled to a selected RCA 1P28 PMT. Upon exposure to the 40-mCi source, signals well above the system's overall dark current (2×10^{-9} amp) were observed. That the signal was not due to a luminous discharge in air was indicated by the fact that an aluminum foil placed in front of the converter did not affect the signal, whereas the PMT current dropped to its dark level when the foil was placed between the converter and PMT. In order to verify that the PMT signal was associated with the luminous output of the converter, measurements were made using configuration A with the distance between the converter and PMT being varied from 10 to 50 cm. The observed PMT current obeyed the inverse square law, thus implying that the air was not strongly absorbing and that the photon source was located at the UV converter. A similar response to electron

irradiation was observed with a Bendix model 407X converter operated at 5 kV and coupled to an EMI 978-3A tube having a quartz window.

It is useful to determine the incident UV photon flux which would produce the same phosphor light output (or PMT current) as that produced by the ^{90}Sr. This was accomplished by replacing the ^{90}Sr with a UV source, measuring the UV flux incident on the converter, and comparing the phosphor output (as indicated by the PMT current) with that produced when the ^{90}Sr was in place. Specifically, we used the 254-nm line of Hg to illuminate the converter and measured the resulting photomultiplier current as a function of the distance r between the UV source and converter. This photomultiplier current varied as r^{-2}. We then used the UV source to illuminate an NBS calibrated photodiode (RbTe cathode, MgF_2 window) and measured the photodiode current (and hence incident UV flux) as a function of the distance r between the UV source and photodiode. This last measurement was checked with a UV intensity meter. The data showed that the incident UV flux varied as r^{-2}. Thus a relation was established between the incident UV flux and the resulting current in the PMT which monitored the light output of the converter's phosphor. This relation enabled us to calculate the incident UV photon flux needed to produce a given photomultiplier current. Using the measured PMT currents resulting from the ^{90}Sr intensity of 2×10^7 e/cm^2-sec, we determined that the equivalent UV fluxes were of the order of 10^8 and 10^7 photons/cm^2-sec for the converter with voltage on and off, respectively.

We used the electron beam of the GSFC Van de Graaff to investigate the energy dependence of the radiation-induced signal in the converter. In this experiment the converter (ITT model No. F4122) was placed in a vacuum to reduce the possibility of arcing. Figure 2 shows the response of the converter as a function of incident electron energy. There is very little effect below 0.4 MeV. The radiation-induced signal increases almost linearly from 0.5 to 1.4 MeV. The signal continues to increase, but at a slightly slower rate, from 1.4 to 1.8 MeV. At the higher energies an appreciable signal was observed when the converter voltage was off. This suggests that part of the effect observed at higher energy may be due to direct activation of the phosphor by electrons

which have penetrated the converter. It is instructive to compare these experimental results with those expected if the electron-induced response is due to Cerenkov production in the MgF_2 window of the UV converter. The Cerenkov yield was calculated on the assumption that multiple reflections in the MgF_2 could be ignored and that there was no Fresnel partial reflection at the interface between the MgF_2 window and the CsTe photocathode. This latter assumption seems plausible because the CsTe is deposited directly onto the MgF_2 window. A typical quantum efficiency was used for the CsTe in order to determine the converter output which would be produced by Cerenkov radiation in the MgF_2. The calculated converter output is shown in figure 2.

Both our data and the results of Viehmann (Applied Optics 14, 2101, 1975) suggest that both fluorescence and Cerenkov radiation contribute to the observed converter signal. However, the results shown in figure 2 indicate that Cerenkov radiation is the dominant effect.

FINE ERROR SENSOR

Introduction

The purpose of the FES is to keep the telescope pointed in the desired direction. The FES used on the IUE consists of a magnetically focused image dissector tube (ITT Model No. F4012-RP, S-20 photocathode, quartz window) incorporated into a full optical/electronic system designed to provide precise target acquisition. As the field of view of the FES is limited to a small solid angle, the device must be capable of detecting small signals. Because the FES must have an unobstructed field of view, it is difficult to shield against Earth's Van Allen belt electrons, cosmic rays, and solar flare particles. This is especially true for the focusing optics of the FES. Hence it is important to investigate the effects of radiation on the FES.

Two types of experiments were performed involving radiation of the FES with an electron source simulating Earth's outer electron belt. In the first experiment the dark current and spectral response of the Image Dissector Tube (IDT) were measured before and after exposure to our 40-mCi source of ^{90}Sr. In the second experiment the

dark current was determined during exposure of the tube to electrons from the ^{90}Sr source, and then during irradiation with electrons from the Van de Graaff at GSFC. The experimental results of the irradiation of a set of Schott glasses proposed for use in the focusing optics of the FES are discussed later in this report.

Permanent Degradation Effects

A technique was devised for studying degradation effects of electron irradiation of the IDT. The FES electronics test package, which was constructed by our personnel in collaboration with GSFC, detects signals from a small portion (2.7×10^{-4} cm^2) of the photocathode. The position of the area observed on the photocathode can be selected by varying the settings on horizontal and vertical deflection potentiometers that control the current to the focus solenoids. The FES electronics has a pulse amplitude discriminator to reject low amplitude noise pulses. Neutral density filters were used in conjunction with a regulated brightness source to set the discriminator threshold just above the noise level. The output pulses passed by the discriminator were counted by a Beckman frequency meter and recorded on a Digitec printer.

To determine the characteristics and response of the tube, the photocathode was illuminated with a spectra-regulated 9-foot lambert brightness source. The brightness source was used in conjunction with three filters (428, 530, and 630 nm with respective bandwidths of 3, 5, and 5 nm) in order to obtain a measure of the quantum efficiency of the photocathode. The photocathode surface was scanned by varying the vertical and horizontal deflection potentiometers. Five respresentative groups, each containing five sample spots, were selected on the basis of their variation in signal level and their location on the photocathode surface. The physical location of the viewing areas and their correspondence with the vertical and horizontal deflection potentiometer settings were known approximately from calibration curves obtained during building and testing of the electronics for the FES. Figure 3 shows the surface of the photocathode and the location of the five groups of five sample spots. The lines connecting the points indicate the five groups of positions which were chosen to represent the photocathode surface. Counts were taken at each of the 25 sample spots with

the brightness source on and off. Successive samplings of the 25 surface spots with the IDT first installed in its mount and then removed and installed again showed that the data were reproducible to within 3 percent.

The technique just described was used to determine light (brightness source on) and dark (brightness source off) counting rates for each of the 25 positions. About 40 dark counts/sec were observed for each position. The IDT was then removed from its mount and its surface was exposed to a 40-mCi ^{90}Sr source for 25 hours to give a flux of approximately 10^{12} e/cm^2. This is approximately the flux which would be incident on an unshielded IDT in about four days in Earth's outer belt. The photocathode was scanned immediately following irradiation and then again one day later. A typical set of data is shown in figure 4, which gives the count rate observed with the light on for each of the 25 positions on the surface. These data were obtained with the 530-nm filter; similar results (including low and high count rates at the same positions) were obtained with the 428- and 630-nm filters. It is instructive to determine the area response of the photocathode by summing the count rate over the five individual positions for each of the groups shown in figure 3. The results so obtained are shown in table 1. The variation in the summed count rate from one filter to another is due to differences in the transmission and bandwidth of the filters and to the quantum efficiency of the photocathode. We note that for a given filter the summed count rate is nearly the same for each area except for the one encompassing positions 1 through 5. The variation in count rates among individual positions in figure 4 and among the groups of positions in table 1 can be understood in terms of the manufacturer's specification that the output be uniform (within 20 percent) over 80 percent of the photocathode diameter. The region of uniform output is shown in figure 3. Thus the low count rates for points 1, 2, and 7 in figure 4 are expected as they are located near the edge of the photocathode surface. This effect is also evident in table 1, which shows a substantially lower integrated count rate over the area which includes positions 1 and 2. The high count rate at points 5 and 8 may be due to blemishes on the photocathode surface.

The effects of irradiation are also shown in figure 4. The results indicate that some degradation has occurred after exposure to 1×10^{12} e/cm^2. For the 530-nm filter data shown in figure 4, the degradation is between 5 and 6 percent. Another indication of the amount of degradation is given in table 1, where the count rate summed over all 25 positions is shown for each of the filters. The summed count rates for the pre-irradiation and postirradiation scans indicate a degradation of about five to eight percent, but the summed count rates for the scans performed one day after irradiation are within three percent of the pre-irradiation values. This suggests that the irradiation-induced degradation is not permanent and appears to recover in about a day.

Real-Time Interference Effects

In order to study real-time effects for the FES, the count rates at positions 19 and 20 (see fig. 3) were monitored before, during, and after irradiation of the IDT. The measurements were performed in a dark room, and no external light source was used to illuminate the photocathode. The count rate before and after exposure to radiation was about 10 counts/sec. Exposure to radiation from the ^{90}Sr source had a significant effect on the measured signal. Various flux rates were obtained by changing the distance between the calibrated ^{90}Sr source and the IDT. For the distances involved here, absorption and scattering by the air have very little effect on the emitted electrons. We found that the CR increases almost linearly at a rate of about 1.4×10^{-4} counts/electron/cm^2 for flux rates ranging from 0.1 to 1.3×10^{13} e/cm^2-sec. There is some deviation from linearity at the higher flux rates; this is probably due to saturation of the electronics in the IDT. As each pixel has an area of 2.7×10^{-4} cm^2, the count rate for the linear portion of the graph corresponds to 0.5 counts per incident electron.

Similar experiments utilizing the 2-MeV Van de Graaff accelerator at GSFC have been performed. In addition to observing the effects produced by varying the incident electron flux, the energy dependence of the radiation-induced count rate was investigated. The Van de Graaff results indicate that at 1.1 MeV the radiation-induced count rate varies

linearly with incident electron flux rate. For a given flux rate, we found that the CR increases linearly with electron energy between 0.5 and 1.1 MeV.

SEC CAMERA TUBE

An electrostatically focused Westinghouse SEC vidicon camera tube is used on the IUE to store an image for subsequent transmission to Earth. As the IUE spends several hours in Earth's outer electron belt during one orbit, tests were performed to determine the effect of this exposure on the stored image. An image was placed on the KCl target of a flight-rated tube (WX-32224) at GSFC. The tube and attached fiber optics plate were then flown to Old Dominion University for irradiation with our ^{90}Sr source. Exposure to radiation began approximately three hr after implantation of the image. The tube was exposed to a total flux of about 1.7×10^{11} e/cm^2 at a rate of about 1.4×10^7 e/cm^2-sec. This dosage and rate are equivalent to those expected for the IUE in one orbit in the outer radiation belt. After irradiation, the tube was immediately taken back to GSFC to assess the effects of electron radiation on the stored image. Although the irradiation did not produce a serious deterioration of the image, a pulse height analysis of the readout before and after irradiation showed that there was an increase in the relative number of small pulses. This indicates a general increase of the background signal.

OPTICAL GLASSES

Introduction

We measured electron-induced degradation for glasses commonly used in optical systems of astronomical satellites. Corning 7052 and 7056 glasses were two samples investigated. After irradiation with 2×10^{13} e/cm^2 from ^{90}Sr, the 7052 glass had a transmission at 300 nm equal to 25 percent of its unirradiated value. This increased rapidly to 75 percent at 500 nm and increased more gradually to 90 percent at 700 nm.

Schott glasses similar to those used in the FES were investigated in detail. Samples were irradiated with monoenergetic electron beams from 2 to 7 MeV and at dosages up to 10^{14} e/cm^2, which corresponds approximately to a 1-year IUE orbit without shielding. The degradation was largest at the shorter wavelengths. At the highest dose, the transmission at 400 nm was about 15 percent of the unirradiated value. The transmission results were used to calculate the degradation which would be experienced by a detecting system, consisting of an S-20 photocathode behind one of the FES glasses, used to view a star with an assumed temperature. These calculations resulted in recommendations to the IUE Project regarding optimum arrangement of glasses in the FES.

We also investigated degradation in glasses irradiated with protons. The Schott glasses commonly used in space technology were irradiated with 85-MeV protons to fluxes from 10^{11} to 10^{14} p/cm^2. Determinations were made of the absorption bands in each glass, the growth of the induced absorption as a function of total dose, and the growth in the density of the color centers (electrons or positive holes trapped at specific sites in the glass network) versus total dose. Similar analyses were performed on data we previously obtained from electron irradiation of these same three types of glass. While it was found in this investigation that electrons and protons produce absorption bands with peaks at the same energies for any one glass, other evidence from this study points to differences in the saturation levels of the induced absorption produced by each type of radiation. These results were published in Applied Optics (M.F. Bartusiak and J. Becher, Appl. Opt. 18, 3342, 1979). A copy of this paper is attached (see Appendix A). Some aspects of this work which are not reported in detail in the paper are discussed below. This material is taken largely from the thesis of Marcia F. Bartusiak, who received her Master of Science degree from ODU in 1979.

When any material is subjected to radiation, two main effects occur: atomic displacement and ionization. In displacement, the incoming particle or photon displaces an atom of the material from its normal lattice position. In highly structured materials such as crystals, this can change certain physical properties. But, since most ceramic materials have an amorphous structure, displacement effects play a minor role in determining

the transmission response of a glass to radiation environments. Ionization is the dominant factor for glasses.

In ionization, the incoming radiation detaches electrons from atoms of the material, allowing them to move through the atomic network. In glass these free electrons and resulting positive holes can then be trapped in such defects as ion vacancies, impurities, or nonbridging oxygens. For example, an electron could become bound to a negative ion vacancy in the glass lattice. Once the charge carriers are trapped, they are capable of absorbing light by electronic transitions; the exact frequency will depend on the environment surrounding the trapped electron or hole. These optically active sites are known as color centers.

Experimental Details

The glass samples were irradiated with protons from the isochronous cyclotron at the University of Maryland. An energy of 85 MeV was selected since the ∿2.8-cm proton range for glass at that energy was much greater than the 0.2-cm thickness of the samples, thus providing a relatively uniform energy deposition throughout the glass sample.

The proton beam was directed to a circular scattering chamber which was approximately 1.5 m (60 in.) in diameter and 0.9-m (36-in.) high. Before irradiation, the glass samples and a scintillator were mounted on a 5.1 × 22.9 cm (2 × 9 in.) ladder which was affixed to a platform in the center of the chamber. This platform could be rotated under external control so that the glass surfaces were normal to the beam line to within a tenth of a degree (see fig. 5). Once the samples were mounted, the chamber was closed and then evacuated to 10^{-6} torr. Each sample was individually placed in position for irradiation by raising or lowering the platform via electronic control from the cyclotron's operational control area. The scintillator was positioned into the beam to observe the beam profile and make sure it was fairly uniform. The center of each glass could be aligned with the beam to an accuracy of 0.2 mm.

Once a glass was positioned into the beam line, the proton beam would be turned on and its current monitored by a Faraday cup located several feet behind the chamber at the end of the beam line. A current integrator

measured the incident flux and automatically shut the beam off when a preset total charge was reached. At that time, the platform would be adjusted to position another sample into the beam line. Once all the glasses were irradiated to a certain fluence, the chamber's vaccum was broken, and the samples were taken out for transmission measurements.

Transmission Measurements

The transmission spectra of the glasses were measured by a Perkin-Elmer Model 200 spectrophotometer. This is a double-beam, grating spectrophotometer which is designed to measure transmissions in the ultraviolet to visible range. A deuterium lamp was used as the light source for a scan from 2800 Å to 3700 Å, while a tungsten lamp was used from 3700 Å to 7000 Å. The bandpass was set at 1.0 nm. The glasses were marked so that they were positioned in the sample holder with the same orientation each time a transmission measurement was made. These measurements were taken approximately one hr after irradiation. During a calibration of the spectrophotometer, it was determined that the percent transmission measurements were reproducible to ±0.2 percent. The wavelength repeatability of the Perkin-Elmer was 2.0 Å.

The transmission scans of each proton-irradiated glass from 2800 Å to 7000 Å are shown in figures 6 to 8. As discussed previously, measurements were taken after each exposure to the 85-MeV protons from fluences of about 5×10^{11} p/cm^2 to 1.5×10^{14} p/cm^2. As expected, each glass exhibited different transmission curves, the particular response being dependent on the composition of the glass. The top curve in each figure indicates the transmission spectrum of the unirradiated sample; the other four curves show how the transmission degrades with each succeeding dosage of protons.

At the highest fluence, the transmission at 4000 Å of all 3 glasses decreased by more than 85 percent. The degradation was largest at the blue end of the spectrum and decreased as the wavelength increased. The deterioration was less severe above 6000 Å. At 6800 Å, transmissions decreased by 60 percent or less. LaK 21 and KzFS N4 maintained the largest transmission levels in the shorter wavelengths

while KzFS N4 and LF 5 changed the least in the longer wavelengths. These results are summarized in table 2.

One can compare the transmission curves produced by the 85-MeV proton irradiations (figs. 6-8) with the spectral responses of the 3 glasses to irradiation by 7.0-MeV electrons (figs. 9-11). The fluences of the 3 electron irradiations were 1.0×10^{12} e/cm^2, 5.0×10^{12} e/cm^2, and 1.0×10^{13} e/cm^2. It appears that for any one glass both protons and electrons produce similar degradation in the ultraviolet to visible range under study. It is evident that each glass is absorbing in a certain area of the spectrum, with that absorption growing as the dosages increase. By comparing the transmission curves produced by proton and electron irradiations, it can be seen that LaK 21 shows absorption areas around 6200 Å and 3900 Å, that KzFS N4 absorbs at approximately 4600 Å, and that LF 5 has a major absorption band around 3500 Å. However, to obtain a more rigorous analysis of those absorption bands, it is necessary to change the transmission data to their corresponding absorption coefficients. The resulting absorption curves were fitted by superposing Gaussian absorption bands. We found that for any one glass both protons and electrons produce absorption bands whose peaks are located at the same energies. This is expected, since the energies of the color centers are dependent on the glass, its defects and composition, rather than the type of radiation inducing the coloration. All the glasses examined exhibited three Gaussian bands in the near ultraviolet to visible region. However, each glass had its own unique fingerprint: LaK 21 with bands at 2.0 eV, 3.2 eV, and 4.6 eV; KzFS N4 with bands at 1.5 eV, 2.7 eV, and 3.8 eV; and LF 5 with bands at 1.7 eV, 2.7 eV, and 3.5 eV. All the resolved spectra also had a fourth Gaussian located with an absorption peak fitted at 5.5 eV or above. This high-energy band characterizes the shift in the absorption edge toward longer wavelengths as the irradiation dosage increases.

Where these bands will be located in any particular glass is dependent on a number of variables which include whether the glass was made under reducing or oxidizing conditions, the types and amounts of impurities in the glass, the polarizing power of the network modifiers, the number of nonbridging oxygens, the coordination number of the cations, and the amount of multivalent additives. Since the composition of the Schott glasses is

proprietary information, it is beyond the scope of this study to attribute each center to a particular kind of electron or hole trap. However, other studies of multicomponent glasses have found that most color centers in the visible region can be attributed to hole trapping, while bands located at energies less than 2.0 eV are due to electron trapping.

As long as the color centers are not affecting one another (i.e. the density of the centers is small), the shape of each band as measured by the half-width U will not change with increased irradiation. Since the band is Gaussian, its half-width will be constant as the number of centers increases. In comparing the half-widths of a particular band for any one glass in tables 3 to 5 for proton or electron irradiations, it is seen that these half-widths do not differ by more than 0.1 eV. Cases where bandwidths fluctuate more than 0.1 eV are believed to be due to the lack of information at wavelengths above 7000 Å. This made a fit to any Gaussian below 1.8 eV difficult and may have affected the parameters of the other Gaussians to a minor extent.

The largest variation of half-widths occurred in the resolution of LaK 21. The maximum induced absorption produced by the 5.1×10^{11} p/cm^2 fluence was very low (<1.3). Thus, the low-energy Gaussians were not well developed. Their fitted half-widths varied appreciably from those found at the higher dosages. The half-widths of the bands at the two higher proton dosages for all the glasses are a more reliable gauge of the structure of the Gaussian bands since the absorption bands have developed fully after those heavier irradiations.

Although proton and electron irradiations produce the same color centers in any one glass, it can be seen by comparing the induced absorption spectra for both irradiations that there are differences between them. Figure 12 compares the induced absorption spectrum of LF 5 after a proton irradiation of 1.5×10^{14} p/cm^2 with its spectrum after an electron irradiation of 1.0×10^{13} e/cm^2. It can be seen that the protons induced a greater absorption at the lower end of the spectrum. This situation reverses at the higher energies. In that area the electron irradiation produced the largest effect. To better observe and analyze this phenomenon, one must compare absorption growth curves. A plot of induced absorption versus dose showed that the induced absorption increased linearly on a

log-log scale up to about 10^6 rad and then quickly attained a saturation level.

Color Center Interpretation of Results

It is instructive to discuss the induced absorption in terms of color centers. The relation between induced absorption and concentration of color centers is given by Smakula's equation (A. Smakula, Z. Physik 59, 603, 1930). In terms of the half-width U of a Gaussian band, the equation becomes (D.L. Dexter, Phys. Rev. 101, 48, 1956)

$$Nf = 0.87 \times 10^{17} \frac{n}{(n^2 + 2)^2} U\alpha_m$$

where N is the concentration of color centers in a particular band, n is the index of refraction of the material, U is given in eV, α_m is the induced absorption at the peak of the band, and f is the oscillator strength (a measure of the strength of the particular electronic transition causing the absorption). This derivation assumes that the width of the absorption band arises from the interaction of the color center with the lattice vibrations.

In computing color center densities, U and α_m are easily obtained from the resolved induced absorption spectra. However, there are no measurements of f for the glasses under study. Values from 0.2 (the oscillator strength of a color center in fused silica) to 1 have been used as an approximation for glass. The value may also vary for each different color center in a particular glass. In this study, f = 1 was used in calculating N for each band of each glass. The results are tabulated in tables 6 to 8. The maximum density obtained in this study was $\sim 10^{17}$ color centers per cubic centimeter. This agrees with published results for other types of glass (Paul W. Levy, J. Amer. Ceramic Soc. 43, 389, 1960).

As can be seen from Smakula's equation, the color center density N is directly proportional to α_m (since under ideal conditions the half-width U would be constant). Therefore, the absorption growth equation can be related to color densities. This leads to

$$N = A' (1 - e^{-b\Phi})$$

where Φ is the total dose (in rads) and A' and b are constants which depend on the wavelength and the glass type. An equation of this form has been previously obtained through kinetic coloring theories (K.J. Swyler, W.H. Hardy II, and P.W. Levy, IEEE Transactions on Nuclear Science, NS-22, 2259, 1975).

The data in tables 6 to 8 were fitted to this equation using the color center densities of each band in a particular glass with its corresponding dose in rads. Figures 13 and 14 exhibit the typical response of all three glasses to electron and proton irradiations—a linear growth of the color center density at low fluences and a rapid saturation at a dose of around 10^6 rads. The solid line through the data points was generated using the parameters A' and b from the fitting process. Those parameters, both for the electron and proton irradiations, are listed in table 9. The effects observed in the absorption growth curves are also present in figures 15 and 16, where the color center densities as a function of the total absorbed dose for the electron irradiations are compared with the densities produced by the proton irradiations. As in the absorption growth curves, the saturation levels of the electron irradiation data fall below those of the protons for low-energy color centers while the situation reverses at higher energies.

It appears that protons favor formation of low-energy color centers more than the electrons, while the electrons have a greater influence in creating centers at the higher energies for the range of energies studied here and for the glasses being considered. This type of behavior (a separate response in color center formation to different types of radiation) has been observed in alkali halides. It has been reported (F. Fischer, Z. Physik 154, 534, 1959) that there are minor yet distinct differences between the coloration by X-rays and by electrons on LiF, NaF, and NaCl.

ELECTRONIC COMPONENTS

Introduction

As part of our investigation of electro-optical instruments, we determined effects induced by electrons incident on metal-oxide-semiconductor field effect transistors (MOSFETs) similar to those used in circuits of astronomical satellites. We chose MOSFETs which operate in the enhancement mode because these are used as logic gates. Both n-channel and p-channel MOSFETs were investigated. In particular, we irradiated the 2N-4351 n-channel and 2N-4352 p-channel Motorola MOSFETs and the n-channel MOSFET from a CD 4007AE COS/MOS dual complementary plus inverter manufactured by RCA. This report of our results for MOSFETs is taken largely from the thesis of Mark D. Skeldon who received his Master of Science degree from Old Dominion University in 1977.

An n-channel MOSFET consists of two channels of n material which are inlaid on a substrate of p material as illustrated in figure 17. A layer of insulator material, in this case SiO_2, is placed over the channels. The metal gate electrode is placed on top of the insulator and extends from the source to the drain channels of the semiconductor. In the p-channel MOSFET the n and p materials are interchanged.

In the enhancement mode MOSFET, the gate must be forward biased to produce active majority carriers in the channel located beneath the gate and insulator material between the source and drain channels. In an n-channel MOSFET, a positive voltage applied to the gate will draw electrons into this channel, causing this channel to effectively become n material and allowing a low-resistance conduction path to exist between the source and drain channels. The resistance in the channel is controlled by the applied gate voltage. Application of a large forward bias to the gate will draw more majority carriers into the channel, thereby lowering the resistance from source to drain and allowing more current to flow. At zero or reverse bias gate voltage, no useful channel conductivity exists and little or no current will flow from source to drain; this causes the device to turn off. In the p-channel MOSFET, forward biasing is through increasing negative voltage. The

application of a negative voltage to the gate will draw holes into the channel, lowering the source-to-drain resistance and allowing current to flow through the semiconductor. Thus, in these devices, the application of a forward bias to the gate enhances the flow of current through the channel.

The CD4011AEs tested contain four dual input NAND gates. A dual input NAND gate consists of two n-channel enhancement mode MOSFETs connected in series with V_{SS} and the output voltage (V_{out}) and two p-channel enhancement mode MOSFETs connected in parallel with V_{DD} and V_{out} as shown in figure 18. A low signal (0 V) applied to input A or B will turn off the corresponding n-channel MOSFET and turn on the corresponding p-channel MOSFET causing V_{out} to be at the supply voltage. Application of a high signal to input A or B will turn off the corresponding p-channel MOSFET and turn on the corresponding n-channel MOSFET; however, the only time V_{out} will be tied to V_{SS} is when both n-channel devices are turned on, in other words, when both inputs A and B are high. In this manner V_{out} will be high whenever input A or B (or both) is low, and V_{out} will be low only when inputs A and B are both high.

The damage mechanism in MOSFETs, both n-channel and p-channel, has been investigated by many researchers. It is believed that the primary mechanism for threshold voltage shifts in these devices is due to radiation-induced space charge buildup in the gate oxide. The radiation produces electron hole pairs in the oxide layer through ionization. The holes which are relatively immobile build up in the oxide layer. The electrons, however, are mobile and drift towards the more positive electrode where they can leave the oxide. This positive charge buildup in the oxide causes the gate electrode to appear more positive to the semiconductor than is actually the case. Therefore, smaller values of positive gate voltage are required to produce the original drain current in the n-channel MOSFET, whereas larger values of negative gate voltage are required to produce the original drain current in the p-channel MOSFET.

Irradiation causes a change in the gate voltage vs. drain current characteristics of a MOSFET. In order to investigate these changes more extensively, it was necessary to perform many tests on the device under

irradiation. A computer was used to perform these tests. The peripheral devices of the computer applied voltages to the device, read output voltages from the device, and the computer analyzed these data rapidly to select and store only the useful information.

The experiment centered around the LSI-11 computer as illustrated in the block diagram of figure 19.

Testing Procedure

The testing of p-channel and n-channel MOSFETs was performed by irradiating the devices in the circuit configuration shown in figure 20. The gate voltage VG and the supply voltage VS were supplied by the two D/A channels of the computer. The voltage drop across the 377 Ω resistor, VD, was measured by the A/D of the computer upon program request.

Data for the drain current vs. gate voltage were obtained by a simple FORTRAN program directing two D/As to supply 10 V to VS and -5 V to VG; VG was then incremented by 1 bit of the D/A (0.0098 V) while sampling VD for each increment until VG reached +5 V. These values for VG and VD were saved on disk. A second program used the above data to calculate the drain current for each value of the gate voltage; the results were then displayed with the plotter.

Data for the threshold voltage vs. dosage curves were obtained by another FORTRAN program. Provisions were made in this program to specify the time interval between tests of the device and the values of VG and VS to be applied during this interval. These voltages were continuously supplied by the D/As while the computer was in a delayed looping process. The time period between tests was dependent on the number of delay loops, which was one of the specified input parameters. At the end of this looping process, VS was set to 10 V and VG was set to -5 V; VG was then incremented by one bit of the D/A until only the least significant bit of the A/D was set high. This corresponds to 0.0794 V or 0.21 mA of current flowing through the 377 Ω resistor. The value of VG for this drain current (threshold voltage) was then saved, and the original specified values of VG and VS were applied before the computer restarted its delay looping to repeat the process. In this manner the

threshold voltage was known as a function of time and could be translated into a function of dosage. This information was displayed for that specified biasing of the device.

Testing of the dual input NAND gates was performed by a simple FORTRAN program. Five volts were applied by a power supply as the supply voltage to the device. One input of each gate was tied to the supply voltage, and the second input was incremented by one bit of the D/A while sampling the output voltage for each increment. A predetermined number of these tests was performed continuously for timing purposes, and only the input and output voltages of the last test were stored on a disk. A number of these tests was performed and displayed graphically.

The program which accumulates the threshold voltage vs. dosage data for these gates is a modified version of the previous program. This program obtains the threshold voltage of the gates by calculating the value of the input voltage for which the output voltage is half the supply voltage (2.5 V). This is done by taking all the points with output voltages between 1 and 3.5 V and fitting these points to a straight line. Once the equation of this line is known, the value of the threshold voltage is determined by using the output voltage value of 2.5 V and by substituting into the equation of the line to determine the threshold voltage. This threshold voltage value and the slope of the line were then the only points saved on disk for each test. The slopes of the lines were compared and found to be in close agreement. The threshold voltages were taken for a known time interval apart and were plotted as a function of time of exposure and translated into dosage.

The devices were irradiated with electrons from a 40-mCi ^{90}Sr source. Several thicknesses of shielding were used to degrade the energy of the electrons.

Results and Discussion

Both n- and p-channel MOSFETs are sensitive to electron irradiation. The drain current of the p-channel MOSFET as a function of gate voltage shows that the characteristic shape of the drain current vs. gate voltage curve does not change with accumulated dosage; however, the gate voltage

necessary to produce a given drain current decreases with accumulated dosage. This is illustrated in figure 21. The drain current of the n-channel MOSFET as a function of gate voltage was not measured due to delays in shipment of these devices.

The threshold voltage shift in n- and p-channel MOSFETs depends on VG, the gate voltage, and VS, the supply voltage applied during irradiation. This is illustrated in figures 22 to 27 where the variations in threshold voltage vs. dosage are shown for various biasing conditions. There apparently exists a linear relationship between the threshold voltage and the accumulated dosage. The slope of this linear relationship depends on the values of VG and VS applied during irradiation. These slopes are summarized for various biasing conditions for both devices in table 10.

The rate at which the threshold voltage changes in both devices also depends on whether the device was previously irradiated. If the device was irradiated using one set of biasing conditions and was later irradiated with a second set of biasing conditions, the rate of change of the threshold voltage in the second case would be different than if the device had been initially irradiated with that biasing. One notable example of this effect is that n-channel MOSFETs irradiated with VG = +5 V and VS = 0 V can be annealed to approximately their original threshold voltage with continued irradiation by changing the biasing to VG = 0 V and VS = 0 or 10 V as shown in figure 28. Devices originally irradiated with VG = 0 V and VS = 0 or 10 V experience degradation in threshold voltage.

The damage produced in n- and p-channel MOSFETs is long lasting. The decreased value of the threshold voltage remained fixed within a few tenths of a volt for periods of up to 30 days when kept at room temperature with no power applied. To remove the damage produced in these devices, we annealed them by heating in an oven to 300 °C. A minimum of one hour was required at this temperature to restore the device to within a few tenths of a volt of the original threshold voltage but always less than the original threshold voltage. Heating to 300 °C for extended periods of up to 30 hr did not damage the devices; however, increases in the threshold voltage ceased after 1 hr of heating. Once annealed in this

manner the devices functioned normally with no effects from previous irradiations. Devices were irradiated with a particular biasing, annealed and reirradiated with another biasing. This procedure was repeated as many as 10 times. Each time the damage produced followed the linear relations summarized in table 10.

Various thicknesses of aluminum shielding were used to investigate the relation between the energy of the electrons and the damage produced. The tests were performed on p-channel MOSFETs irradiated with VG = -5 V and VS = 0 V. Shielding was inserted at the beginning of the test and removed at the middle of the tests. Slopes of the threshold voltage vs. dosage are shown in figures 29 and 30.

In one case the cover of a p-channel MOSFET was removed and the device was irradiated. A more rapid degradation due to the lack of the shielding was noticed. After irradiation the device was exposed to ultraviolet radiation from a mercury penlight source. The penlight had to be placed within 0.1 cm of the device before significant annealing was noticed. Once annealing began, the original threshold value was attained within 10 min. Additional exposure to the ultraviolet radiation increased the threshold voltage beyond the original value. A second irradiation and ultraviolet anneal of the same device were performed, and the results are shown in figure 31.

Our study with the n-channel MOSFET of the CD4007AE showed degradations similar to the 2N4352 n-channel MOSFET. However, the rate of change of the threshold voltage was less due to the difference in package shielding and dosage received.

The switching characteristics of the COS/MOS dual input NAND gates are affected by electron irradiation. After irradiation the output voltage from the device switched from high to low with lower values of the input voltage. This is shown in figure 32, where the rightmost curve is the normal characteristic curve with no irradiation and was reproduced several times over a period of several days with no change. The curves to the left show the effect of continued irradiation. The leftmost curve is the switching characteristic of the gate after approximately 5.2×10^5 rads or 2.44×10^{11} e/cm^2. All four gates on one CD4011AE degraded at

approximately the same rate, as can be seen in figure 33, which shows how the threshold voltage changes for the four gates of an irradiated CD4011AE.

These gates appeared to suffer long-term damage due to irradiation as did their component transistors. The decreased value of the threshold voltage remained fixed for several days. To remove some of the damage, we maintained these devices for several hours at 150 °C, which was the highest temperature their packaging could withstand. Values of the threshold voltage for the four gates on three separate deivces after irradiation are shown in figure 34. The device indicated by the broadened line was heated to 150° C after the fourth day.

To determine what effect heating had on the threshold voltage of these gates, a device was monitored while it was repeatedly heated and cooled. The device was heated to 150° C and then allowed to cool to room temperature for intervals of 10 min. The results showed that heating the device to 150° C lowered the threshold voltage by 0.15 to 0.20 V, and cooling the device to room temperature restored the original threshold voltage.

Since the threshold voltage shifts due to irradiation with ^{90}Sr have been shown to be approximately linear at these dosages, the data contained in this report can be used to estimate the accumulated dose of electron irradiation from ^{90}Sr received by 2N-4351 or 2N-4352 MOSFETs. Since the p-channel MOSFET is more radiation-sensitive than the n-channel MOSFET, it can be used to more accurately estimate the amount of radiation produced by a ^{90}Sr source. In order to do this, the value of the threshold voltage must be measured before exposure. During exposure to the electron irradiation, the biasing of the device must be held fixed at known values. After exposure to the ^{90}Sr source, the value of the threshold voltage must be measured again. An approximation for the accumulated dose can be calculated as follows:

$$\text{Accumulated Dose} = \frac{\text{Change in threshold voltage due to irradiation} - \text{Threshold voltage before irradiation}}{\text{Rate of change of threshold voltage (from table 10)}}$$

After the device has been irradiated and the biasing removed, testing of the change in threshold voltage can be made as much as 30 days after exposure provided it is kept at room temperature with no power applied. Before the device is used again for this purpose, it must be annealed to within a few tenths of the original threshold voltage, preferably by heating it to 300° C for 1 hr with all leads grounded. This procedure for monitoring electron irradiation can be repeated with the same device as many as 10 times and possibly more.

In order to monitor electron fluences from other beta sources, similar experiments must be conducted using mono-energetic electrons to obtain data on the energy dependence of the damage produced in these devices. Once these data have been accumulated on these and other MOSFETs, it may be possible to use them as radiation-monitoring devices in spacecraft.

SILICON PHOTODIODES

Introduction

Silicon PIN photodiodes intended for use on the IUE to sense the bright solar signal were investigated to determine their sensitivity to electron and proton irradiation. These devices are state-of-the-art diodes consisting of a p-n junction with a doping profile tailored in such a way that an intrinsic layer, "i region," is sandwiched between a p-layer and an n-layer. The sensitivity range and frequency response can be optimized by carefully modifying the intrinsic layer. Although these devices are not as sensitive as photomultipler tubes, they are relatively cheap, low-power, compact devices with a wide spectral response. In a terrestrial orbit they are exposed to a radiation environment made up predominantly of energetic protons and electrons; therefore, it is important to have some understanding of the possible effects of radiation on their spectral response.

Radiation effects were investigated by bombarding silicon PIN photodiodes with electrons and with protons. Samples with intrinsic region resistivities of 10 and 400 ohm-cm and various thicknesses of anti-reflection (AR) coatings were studied. The AR coating enhances the spectral response in certain regions of the spectrum. Most of the devices

studied in this work were fabricated using the diffusion of p and n regions into a high-resistivity (less than 1 ohm-cm) semiconductor substrate. A 40-mCi ^{90}Sr beta source and proton synchrocyclotron were used to simulate Earth's radiation belts. The beta spectrum of the ^{90}Sr source provides a good simulation for Earth's electron belts. The synchrocyclotron, which provides proton energies from 30 to 600 MeV, allows simulation of cosmic rays.

A substantial amount of work exists on the effects of irradiation on silicon solar cells. Although similar to PIN photodiodes in that they are both p-n junction type devices, they differ in their junction characteristics and mode of operation. Photodiodes are used for signal detection while solar cells are used to convert solar radiation directly to electrical energy. Thus, most of the radiation damage studies in solar cells have been directed toward understanding mechanisms responsible for the reduction of their output power, whereas little work has been published on the irradiation-induced degradation in spectral response of PIN photocathodes.

Dr. C.S. Reft, a postdoctoral research associate employed under NASA grant NSG-5053, was extensively involved in the silicon photodiode study. Much of the present section was taken from a paper which Dr. Reft and the authors of this report are preparing for publication.

Experimental Technique

The spectral response of the diodes was determined prior to irradiation by measuring the photoconductive current as a function of wavelength from 350 to 1100 nm. Monochromaticity was achieved by focusing light from a tungsten halogen lamp onto the entrance slit of a Beckman quartz prism monochromator. The diodes were positioned at the exit slit of the monochromator. The bandwidth was approximately 15 nm. To minimize the effect of fluctuations in the light source and electronics, the signal from each test sample was compared to a similar unirradiated reference diode. This was accomplished by coupling a double-beam attachment to the output slits of the monochromator. The movable mirror in the double-beam attachment reflected the monochromator light to either the sample or reference diode. Repeated measurements of a diode's spectral response showed that the ratio of sample to reference photocurrents was reproducible within one percent.

The quantity of interest for a photodiode exposed to radiation is the change in photoconductive current over its spectral range. Thus the degradation $R(\lambda)$ is defined here as the decrease in spectral response of the diode due to irradiation. The irradiation-induced degradation at various wavelengths is given by the change in the ratio of the two photocurrents as a function of absorbed dose. The degradation can be written as

$$R(\lambda) = \frac{\left(\frac{I_s}{I_r}\right)_o - \left(\frac{I_s}{I_r}\right)}{\left(\frac{I_s}{I_r}\right)_o} = 1 - \frac{I}{I_o} \qquad (1)$$

where I_s and I_r are the sample and reference photocurrents and I_o and I are the sample photocurrents before and after irradiation, respectively. From the disintegration rate of the calibrated ^{90}Sr source, the absorbed energy in rads was determined by integrating over the beta energy distribution. The accuracy of the calculated dosage was ±23 percent with this technique. This uncertainty is due to the combined uncertainties in the source calibration (±20 percent) and in the distance measurement (±10 percent) between the source and sample. For the proton irradiations the absorbed dose was calculated by using the proton fluence (measured with a Faraday cup) in conjunction with the diode thickness and the specific energy loss (dE/dx) of the incident protons.

Discussion of Results

PIN photodiodes are characterized by the resistivity of the intrinsic region and the thickness of the AR coating. The diodes sometimes are encapsulated with a protective window. We investigated the radiation characteristics of the five types of diodes whose specifications are shown in table 11. Note that types A and A* are identical except that A* is encapsulated and covered with a Corning 7052 glass window. Our tests included at least three samples of each of the five types.

Figure 35 shows the degradation of $R(\lambda)$ for types A*, G, and R. We note that type R, which has a low resistivity (10 ohm-cm), is the most

radiation resistant of these three types. Sample type A* shows a pronounced degradation peak [$R(\lambda)$ = 55 percent] at 450 nm. Beyond this the degradation drops to 6 percent at 800 nm and then increases gradually with wavelength. The degradation of type G is very small ($\approx$ 1 percent) up to about 700 nm. Beyond about 800 nm, there is increasing degradation in both A* and G at rates which, as we will discuss subsequently, are related to the different absorbed doses.

Returning now to the peak near 450 nm, we note from table 11 that A* and G have the same resistivity (400 ohm-cm) but differ in 2 respects: (1) A* has no AR coating whereas G has a 400-nm coating, and (2) A* is encapsulated with a 7052 glass window while G is not sealed. In separate tests with type A, B, and G, which differ only in the thickness of the AR coating, we found that the degradation varied as much among samples of the same type as it did among different types. Thus we conclude that the pronounced degradation near 450 nm in sample type A* is associated with the encapsulating 7052 glass window.

We found that beyond about 800 nm electron irradiation of sample types A, B, and G produced essentially the same degradation per unit absorbed dose. Figure 36 shows typical results for three different fluences. As shown in table 11, these three types of diode differ in AR coating thickness but have the same resistivity. The fact that all three types exhibit the same degradation per unit absorbed dose suggests that the irradiation-induced changes occur in the silicon. This is consistent with the fact that sample type R is the most radiation resistant as shown in figure 35. Type R samples had an intrinsic layer resistivity of 10 ohm-cm compared to 400 ohm-cm for the other 3 types. The low resistivity of the intrinsic layer implies a high impurity content and, therefore, a more disordered crystal structure which would be less sensitive to displacement damage. The other three types have a higher resistivity and correspondingly lower impurity content relative to the type R samples. Their crystal structure would be more sensitive to displacement damage effects. That all of these samples exhibit essentially the same degradation behavior is consistent with their having the same resistivities.

Referring again to figure 36, we note that the divergence between equidose curves increases with wavelength. This characteristic is made

explicit in figure 37, which uses the data in figure 36 to show the degradation as a function of dose at several wavelengths.

Some annealing studies were performed to determine whether the spectral response of the diodes would be recovered. Essentially no recovery occurred at room temperature over a period of two months. Annealing the diodes to 100° C for 1-hr intervals produced very little recovery.

We have made a preliminary investigation of radiation effects produced by 600-MeV protons incident on type A, B, and G diodes. Again we find nearly the same degradation in these three types. Figure 38 shows both electron and proton results for an encapsulated high-resistivity diode. This diode was irradiated to 0.35 Mrad with ^{90}Sr electrons; then an additional 0.1 Mrad was deposited by 600-MeV protons. In the region associated with the degradation peak at the low wavelength end, the protons produced less than five percent additional degradation. This suggests that at these wavelengths protons and electrons are about equally effective in producing radiation damage per unit absorbed energy. On the other hand, protons are much more effective in the wavelength region associated with degradation induced in silicon. At 1000 nm, for example, 0.35 Mrad from ^{90}Sr electrons produced a degradation of about 7 percent, whereas an additional 0.1 Mrad from 600-MeV protons increased the degradation to 35 percent. Comparing these percentages with analogous results deduced from figure 36 for the increase in degradation expected from an additional 0.1 Mrad from electrons, we infer that at these wavelengths and irradiation levels 600-MeV protons are about 5 times as effective as ^{90}Sr electrons in producing degradation per unit of absorbed energy.

Theory

To obtain a more quantitative description of the damage process, the observed degradation $R(\lambda)$ must be related to the measured photodiode currents. Under normal operating conditions the current (W. Gärtner, Phys. Rev. 116, 84, 1959) is given by

$$I = I_o\left(1 - \frac{e^{-\alpha W_o}}{1 + \alpha L_o}\right) \qquad (2)$$

where I_o is the incident photon current, α is the absorption coefficient for silicon, and W_o and L_o are the depletion width and minority carrier diffusion length in the diode before irradiation, respectively. The total current given in this equation consists of two contributions: one $(e^{-\alpha W_o})$ due to carriers generated inside the depletion width, the other $(1 + \alpha L_o)$ due to carriers generated in the adjacent bulk material and diffusing into the junction. Combining equations (1) and (2) shows that the degradation is related to the current by

$$R(\phi) = 1 - \frac{I}{I_o} = \frac{\dfrac{e^{-\alpha W}}{1 + \alpha L} - \dfrac{e^{-\alpha W_o}}{1 + \alpha L_o}}{1 - \dfrac{e^{-\alpha W_o}}{1 + \alpha L_o}} \qquad (3)$$

where W and L are the depletion width and minority carrier diffusion length after irradiation, respectively. In the case of solar cells, it is generally assumed that the depletion width does not change with irradiation, but that the effect of irradiation is a decrease in the diffusion length. Unlike solar cells, PIN diodes have large depletion widths (20 to 100 μm), and therefore a significant portion of the current is due to electron-hole pairs generated inside the depletion width. This is in agreement with the observed pulse height distributions (which will be discussed shortly) in that the pulse height spectrum for a typical PIN shows that the depletion width is the main contribution to the charge accumulated. Thus irradiation-induced changes in the depletion width will affect the diode current considerably more than would be expected in a solar cell.

The simplest way to include the effects of irradiation on the depletion width is to assume that the radiation-induced defects can be simulated by impurity dopants whose characteristics will depend on the position of the defects in the band gap. Therefore the effective doping density will be increased with radiation, that is,

$$N(\Phi) = N_D(0) + \sigma\Phi \tag{4}$$

where $N(\Phi)$ is the effective dopant density, $N_D(0)$ is the impurity doping density, and σ is the cross section for defect production. Since the depletion width is inversely proportional to the impurity doping density, an increase in the effective dopant density would decrease the depletion width. With these assumptions the depletion width can be written as

$$W = B[N_D(0) + \sigma\Phi]^{-1/2} \tag{5}$$

In this equation, $B = \sqrt{(2\varepsilon_s kT/q^2)}$, where ε_s is the static dielectric constant and $q = 1.6 \times 10^{-19}$ C. This gives $B = 1.17 \times 10^4$ cm$^{-1/2}$ at room temperature. We can write equation (5) in the form

$$(B/W)^2 = N_D(0) + \sigma\Phi \tag{6}$$

In this treatment the degradation is attributed to changes in the depletion width. This will be especially true if L_o is less than 10 μm. From the measured degradation $R(\lambda)$, the depletion width W can be obtained using equation (3) and assuming that the minority carrier diffusion length L does not change appreciably at these levels of irradiation. Setting $L = L_o$ and rearranging equation (3), the depletion width W is given by

$$W = -\frac{1}{\alpha} \ln\left[e^{-\alpha W_o} + R(\lambda)\,(1 + \alpha L_o - e^{-\alpha W_o})\right] \tag{7}$$

Knowing W_o and L_o, the depletion width can be calculated from the measured degradation. By measuring $R(\lambda)$ at six different wavelengths after each irradiation, an average depletion width $\overline{W}$ was obtained. In figure 39, $(B/\overline{W})^2$ is plotted as a function of fluence for a typical diode of 400 ohm-cm resistivity having a depletion width of 30 μm at 10-V bias and a minority carrier diffusion length of 5 μm before irradiation. The data can be fitted to a straight line where the slope and intercept are σ and $N_D(0)$, respectively. We get

$\overline{\sigma} = 0.49\ cm^{-1}$

$N_D(0) = 1.6 \times 10^{13}\ cm^{-3}$

These values are in reasonable agreement with theoretical results which predict $N_D(0) = 1.5 \times 10^{13}\ cm^{-3}$ for 400 ohm-cm silicon and $\sigma = 0.3\ cm^{-1}$ for electron irradiation (H. Matarẽ, Defect Electronics in Semiconductors, Wiley-Interscience, 1971 and J. Corbett, Electron Radiation Damage in Semiconductors and Metals, Academic Press, 1966). Our interpretation is also consistent with the radiation resistance of type R diodes. For these diodes the resistivity is 10 ohm-cm, which converts to an impurity doping density of about $5 \times 10^{4}\ cm^{-3}$. Using a defect cross section of $0.4\ cm^{-1}$, the effective dopant density has increased less than 3 percent after an exposure of $3.6 \times 10^{13}\ e/cm^{2}$.

Pulse Height Spectra

The size distribution of output pulses produced by proton irradiation of PIN photodiodes can be used to study additional characteristics of mechanisms associated with the degradation. The purpose of these measurements was to determine the photocurrent due to proton irradiation of the PIN diode. We found that the pulse height could be understood in terms of electron-hole pairs created within the depletion width by the energy deposited by the incident protons.

In view of the fact that the induced pulse is expected to be proportional to the depletion width, we used a Centronic diode having a large depletion width (about 150 μm at 15 V). The Centronic signal was much more easily separated from the noise than were signals obtained with smaller depletion width diodes such as the United Detector A, B, and G types (38 μm at 15 V) which we used in other tests. Figure 40 shows a typical pulse height distribution observed for a Centronic diode during irradiation with 50-MeV protons. We recorded pulse heights using both 256 and 512 channels. The pulse height response of the detection system was calibrated by injecting a known charge to a load capacitor. The peak of the proton-induced pulses corresponded to charges of $(19 \pm 1) \times 10^{-15}$ C for 256 channels and to $(20.5 \pm 1) \times 10^{-15}$ C for 512 channels. This value can be compared to

the amount of charge expected as a result of creation of electron-hole pairs in the depletion width. The charge pulse created by the passage of an ionizing particle is given by

$$Q = \frac{qE}{E_o}$$

where q is the charge of the electron, E is the energy deposited by the particle in the depletion region, and E_o is the amount of energy required to produce one electron-hole pair (3.62 eV for silicon). For a 150-μm depletion width, a 50-MeV proton deposits about 0.35 MeV. This corresponds to a charge pulse of about 15.5×10^{-15} C, which is 25 percent lower than the experimental value of $(20 \pm 1) \times 10^{-15}$ C. This is good agreement considering that the depletion width is accurate to about 20 percent. Moreover, the calculated value is probably a little low because some pairs will be created outside the depletion region but within the diffusion length for minority carriers. These charge carriers will add a contribution to the total charge. These results indicate that the observed pulse height spectrum is in good agreement with that expected on the basis of creation by the incident proton of e-h pairs, mainly within the depletion region of the diode.

ULTRAVIOLET WINDOW MATERIALS

Introduction

Some crystals exhibit fluorescence and phosphorescence when bombarded by charged particles. This radiation-induced signal can significantly affect real-time data acquisition by optical-electronic devices operating in a radiation environment. We have studied radiation effects which occur when optical windows and filters are exposed to radiation which simulates Earth's outer electron belt. Our measurements included both the integrated output and the spectral distribution of the emitted light.

Phosphorescence Induced by ^{90}Sr Electrons

In the first series of experiments, the magnitude of the phosphorescence signal as well as its decay was studied as a function of exposure dose. A photon counting system was used to measure the phosphorescence signal from the samples. An ITT FW130 (S-20 photocathode; 7056 glass window) photomultiplier tube detected the signal from the sample before and after exposure to radiation. This signal was then processed by a pulse amplitude discriminator, and the output pulses were counted by a Beckman frequency meter and recorded on a Digitec printer.

As a check on the sensitivity and reproducibility of the photon counting system and also to obtain some preliminary data, phosphorescence was looked for in a number of samples exposed to electrons from a 40-mCi ^{90}Sr source. These samples were KCl, MgF_2, and NaCl. The KCl was chosen because it is the target in the SEC vidicon tube; MgF_2 (Harshaw high purity) was investigated because of its use as a UV window material; and NaCl was selected for convenience.

Phosphorescence from KCl was observed for almost two hours after exposure to radiation. Phosphorescence was observed from the NaCl samples for almost 24 hr, whereas signals from the MgF_2 samples persisted for almost 4 hr. IRTRAN 2, which is used for windows in the near IR, also exhibited a strong phosphorescence.

Phosphorescence Induced by 3.5-MeV Electrons

To investigate radiation-induced phosphorescence at higher energies and dosages, the Linac at SREL was used. Single crystals of KCl and NaCl were exposed to 3.5-MeV electrons with a total flux of about 5×10^{12} e/cm^2 at a rate of 1.2×10^{10} e/cm^2-sec. Approximately three minutes elapsed between the end of the irradiation and the beginning of the phosphorescence measurements. Negligible phosphoresence was observed; however, both samples were significantly colored. The KCl sample was bluish purple while the NaCl sample had a yellowish color. This coloration is presumably due to the creation of color centers in the crystals by the irradiating electrons. This phenomenon has been previously observed and studied in the alkali halides. The coloration disappeared after two days at room temperature, indicating that the defects annealed out at this temperature.

Spectral Distribution of Fluorescence

We measured the spectral distribution of the fluorescence emitted by crystals exposed to our 40-mCi ^{90}Sr source. The crystals were mounted to the entrance slit of a one-meter evacuable McPherson monochromator. The monochromator has a bandwidth of about 3 nm and can scan from 60 to 600 nm. The detector, which was connected to the exit slit of the monochromator, was an EMR model 542F photomultiplier tube with a MgF_2 window and CsTe photocathode. The photomultiplier tube was used in both the photon counting and current integrating modes. This system was calibrated for the 254-nm Hg line by measuring the intensity of the Hg line with a calibrated NBS photodiode at the entrance and exit slits of the monochromator. The analysis showed that the efficiency of this system was about 15 percent at 254 nm for detecting photons which are produced in the irradiated sample.

Due to its transmission characteristics, MgF_2 is widely used in UV optical systems. Thus it is of interest to determine whether MgF_2 exhibits radiation-induced fluorescence. The fluorescence spectrum obtained for a highly polished single crystal of MgF_2 (Harshaw, 2-mm thick) is shown in figure 41, where the logarithm of the radiation-induced photon count rate measured by the photomultiplier is plotted as a function of wavelength. Two broad emission bands were observed at about 180 and 210 nm. The fluorescence spectra of BaF_2, CaF_2, and SrF_2 crystals are also shown in figure 41. These crystals along with MgF_2 form an isoelectronic series of group II-A elements with fluorine. Therefore, they were studied to provide additional information on the fluoresence of MgF_2. The CaF_2 was a highly polished single crystal (Harshaw, 2-mm thick). The BaF_2 (4-mm thick) and SrF_2 (7-mm thick) were unpolished single crystals. The fluoresence spectra of CaF_2 and SrF_2 are similar, with each having one strong broad emission band centered around 265 and 275 nm, respectively. The fluorescence spectrum of BaF_2 has bands located around 195, 220, and 280 nm. Using the 254-nm calibration of the system in conjunction with the data of figure 41, we calculated a fluorescence yield expressed as the number of 254-nm photons per steradian per MeV of incident electron energy deposited. Values ranged from 0.3 MeV^{-1} $ster^{-1}$ for UV grade MgF_2 to 27 MeV^{-1} $ster^{-1}$ for CaF_2. The decrease

in signal beyond 300 nm is due to the cutoff of the CsTe photocathode and to the decreasing efficiency of the grating which is blazed at 150 nm.

Single crystals of the following widely used optical window materials were investigated: Al_2O_3 (Melles Griot, WSA-005, 2-mm thick), LiF (Harshaw, 2-mm thick), and SiO_2 (3-mm thick). The fluorescence spectra of these materials are given in figure 42. All of the materials exhibit fluorescence between 130 and 350 nm. Al_2O_3 shows a small emission peak around 175 nm and a strong broad emission peak around 275 nm. The spectrum of LiF shows relatively constant fluorescence between 150 and 310 nm with small emission peaks around 180 and 280 nm. The SiO_2 spectrum exhibits a relatively constant fluorescence between 180 and 290 nm with a small emission peak near 210 nm. Below 180 nm there is a very rapid decrease in fluorescence which is due to the transmission properties of our SiO_2 sample. Here again the decrease beyond 300 nm is due to the cutoff of the CsTe photocathode and to the decreasing efficiency of the grating.

Irtran 2, which is used as a window material in the near infrared, was investigated for fluorescence. A large radiation-induced fluorescence was found near 464 nm using an ITT-FW130 PMT (S-20, 7056 glass).

As optical filters may also be used in astronomical satellites, a study of their irradiation-induced fluorescence was undertaken. The Corning 9863 filter was studied because it is one of the components in the UBV system used in astronomical photometry. A fluorescence spectrum having a broad emission peak near 280 nm was observed for this filter.

SUMMARY

We measured long-term degradation and transient interference in instruments and components subjected to a radiation environment which simulates Earth's outer electron belt.

We found that when an unshielded IUE ultraviolet converter is irradiated by a 40-mCi ^{90}Sr source positioned so as to approximate the peak flux in Earth's outer electron belt, the electron-induced output of the converter is the same as that produced by an incident UV flux (254 nm) of 10^8 photons/cm^2-sec. The image dissector tube used as the

main component of the fine error sensor (FES) underwent a degradation of about 5 percent when exposed to 10^{12} e/cm^2 from ^{90}Sr. Bombardment of the FES induced an output of 0.5 counts per incident electron for flux ratos ranging from 0.1 to 1.3 × 10^7 e/cm^2-sec. Irradiation of the SEC camera tube with 1.7 × 10^{11} e/m^2 from ^{90}Sr did not produce serious deterioration of the stored image. However, there was an increase in the relative number of small pulses in the output, which indicates a general increase of the background signal.

Schott glasses similar to those of the FES were irradiated with 2- to 7-MeV electron beams at dosages up to 10^{14} e/cm^2. Results of the transmission measurements were used to make calculations which resulted in recommendations regarding optimum arrangement and shielding of glasses in the FES. We also measured degradation induced by 85-MeV protons incident on Schott glasses. Transmission measurements extended from 280 to 700 nm. The absorption spectra were fitted with three Gaussian bands in the near UV to visible region. A fourth Gaussian was associated with the absorption edge. For any one glass, we found that protons and electrons produced absorption bands with peaks at the same energies but with different saturation levels.

We invostigated effects induced by ^{90}Sr electrons incident on MOSFETs similar to those used in circuits of astronomical satellites. For a p-channel MOSFET we found that the characteristic shape of the drain current vs. gate voltage curve does not change when irradiated with electrons. However, the gate voltage necessary to produce a given drain current decreases with accumulated dosage. We observed a linear relationship between the threshold voltage and the cumulative dosage for both n- and p-channel MOSFETs. The slope of the linear relationship depended on the gate and supply voltages applied during irradiation.

Silicon PIN photodiodes were irradiated with electrons from ^{90}Sr and with 600-MeV protons. Samples tested were United Detector Technology types A, B, and G. We measured changes in the spectral response of these diodes from 350 to 1100 nm for absorbed doses up to 1.25 Mrad. With the exception of samples encapsulated by a Corning 7052 glass window, all diodes showed little degradation (less than 5 percent) at wavelengths below 700 nm. Encapsulated type A diodes showed a strong degradation

peak (about 55 percent) at 450 nm. High-resistivity (400 ohm-cm) samples degraded considerably more than low-resistivity (10-ohm-cm) samples: for example, at 1000 nm the 10 ohm-cm samples degraded 3 percent after 0.7 Mrad of ^{90}Sr electrons, whereas the corresponding degradation was 20 percent for the 400 ohm-cm samples. The observed degradation was interpreted in terms of changes in the depletion width of the dicde.

We investigated luminescence induced by electrons incident on several UV window materials with emphasis on MgF_2. The spectrum of fluorescence induced in MgF_2 had 2 broad emission bands at 180 and 210 nm. We calculated the fluorescence yield in terms of the number of 254-nm photons per steradian per MeV of incident electron energy absorbed. We found a value of 0.3 MeV^{-1} $ster^{-1}$ for MgF_2.

APPENDIX A

PROTON-INDUCED COLORING OF MULTICOMPONENT GLASSES

Reprinted from APPLIED OPTICS, Vol. 18, page 3342, October 1, 1979

Proton-induced coloring of multicomponent glasses

M. F. Bartusiak and J. Becher

Proton-induced absorption over the 280–700-nm region and growth of that coloring with increasing dosage of proton radiation were determined for three Schott glasses used as focusing elements in the International Ultraviolet Explorer. It was found that the absorption spectra for each glass can be fitted with three Gaussian shaped bands in the near UV–visible range, while a fourth Gaussian characterizes the absorption edge. For doses up to 10^7 rads, the dependence of the induced absorption α on total dose Φ is accurately described by the saturating exponential function $\alpha(\lambda,\Phi) = \alpha_s[1 - \exp(-b\Phi)]$, where α_s and b are constants dependent on the wavelength and glass type. The proton irradiation results were then compared to the effects of electron irradiation on those same three types of glass. For any one glass, it was determined that electrons and protons produced absorption bands with peaks at the same energies but with different saturation levels. For the glasses and wavelength region investigated, proton irradiation induced higher absorption saturation levels α_s in the longer wavelengths, while electron irradiation induced greater absorption in the shorter wavelengths.

Introduction

Meteorological satellites, orbiting astronomical telescopes, and exploratory spacecraft all carry with them complex optical systems whose transmission can be severely affected by the harsh radiation environment of space. Radiation-induced darkening of a spacecraft's refractive components can lower expected signal levels. Most investigations into this effect have used either electron or gamma-ray irradiation to simulate a space environment, mainly because of the easier accessibility of such sources for long-term studies. Detailed information on the coloring of glass by other types of radiation encountered in space, in particular protons, is limited. Yet there is a great need to examine proton-induced effects since solar flares, galactic cosmic radiation, and a large portion of the inner Van Allen belt radiation are composed of energetic protons and, depending on the orbit and the spacecraft's shielding, could be the main influence in degrading the transmission of a material. As a result of these concerns, the study described here was undertaken.

This paper will describe the coloring induced by 85-MeV protons in three Schott glasses representative of glass types used in space applications. They are now being used as focusing elements in the International Ultraviolet Explorer Fine Error Sensor. It will be shown that the absorption (i.e., coloring) induced in each glass by the radiation can be resolved into three optical absorption bands in the near UV–visible range. In addition, it will be discussed how that absorption grows with increasing dosages of protons, thus providing the means to predict degradation in any of the three glasses for a particular fluence of proton radiation. Similar analyses were performed on data obtained from a previous study on the effects of 7.0-MeV electron irradiation on those same three types of glass.[1] It will be shown that protons and electrons produce absorption bands with peaks at the same energies for any one glass but with different absorption saturation levels after irradiation to doses around 10^6 rads.

Mechanisms of Coloring

The mechanisms involved in the coloration of transparent crystals and glasses by radiation are fairly well understood.[2,3] Ionization is the dominant factor. In ionization, the incoming radiation detaches electrons from atoms of the material, allowing them to move through the atomic network. A few percent of these free electrons and resulting positive holes can be trapped in defects within the material, such as ion vacancies, impurities, or nonbridging oxygens. Once the charge carriers are trapped, they are capable of absorbing light by electronic transitions; the exact frequency will depend on the environment surrounding the trapped electron or hole. These optically active sites are the well-known color centers.

When this work was done both authors were with Old Dominion University, Physics Department, Norfolk, Virginia 23508. M. F. Bartusiak is now with Boston University, Physics Department, Boston, Massachusetts 02215.

Received 11 June 1979.
0003-6935/79/193342-05$00.50/0.

Table I. Characteristics of Schott Glasses[12]

Type	Abbe number[a] ν_d	Density (g/cm^3)	Index of refraction[b] n_d
LaK 21	60.10	3.74	1.641
KzFS N4	44.30	3.20	1.613
LF 5	40.85	3.22	1.581

[a] $\nu_d = (n_d - 1)/(n_F - n_C)$, where n_F is the index of refraction at the blue hydrogen line (486.1 nm) and where n_C is the index of refraction at the red hydrogen line (656.3 nm).

[b] n_d is the index of refraction at the yellow helium line (587.6 nm).

Two aspects of this radiation-induced coloring were examined. First, the absorption induced by the radiation was determined over the wavelength region of interest (i.e., an induced absorption spectrum).[4] To measure this, the total absorption before irradiation (a combination of the true absorption of the material and the apparent absorption due to reflectivity at the surface) was subtracted from the total absorption after irradiation. Since the apparent absorption is not appreciably affected by irradiation, surface reflection effects subtract out this way. The quantity that results is known as the induced absorption α. Second, it was seen how this induced absorption grows as a function of the total dose.

The induced absorption spectrum (with wavelength converted to its equivalent photon energy) consists of the superposition of Gaussian shaped absorption bands, each corresponding to a different color center.[5] Each absorption band at energy E can be described as

$$\alpha(E) = \alpha_m \exp[-4 \ln 2[(E - E_0)/U]^2], \quad (1)$$

where E_0 is the photon energy in electron volts at the peak of the band, U is the full width at half-maximum, and α_m is the induced absorption at the band maximum. Growth of a radiation-induced absorption band in time at a constant flux has been found in investigations of alkali halides and glasses[6-9] to be described by one linear term and one or more saturating exponentials

$$\alpha(t) = \sum_{i=1}^{N} A_i[1 - \exp(-B_i t)] + \alpha_1 t, \quad (2)$$

where N is the number of exponential components, t is the time in seconds, A_i and B_i are the magnitude and growth constants, respectively, and α_1 is the slope of the linear component. Previous studies[10,11] have reported that one exponential component accurately describes radiation-induced absorption growth in a wide variety of glass types, particularly multicomponent Schott glasses.

In this investigation, the induced absorption was analyzed as a function of total dose Φ (in rads). Since Φ is related to time through the dose rate ϕ ($\Phi = \phi t$), Eq. (2) with $N = 1$ can be put into the alternate form

$$\alpha(\Phi) = \alpha_s[1 - \exp(-b\Phi)] + \alpha_l \Phi \quad (3)$$

This result requires the assumption that coloring is independent of the dose rate ϕ, behavior generally found to be true in previous studies of radiation effects on glass.[10,11] The $\alpha_s[1 - \exp(-b\Phi)]$ term is usually viewed as representing the absorption that arises as the defects already present in the material become populated with holes and electrons. Because of their limited number (around 10^{15}–10^{17}/cm^3), these color centers saturate to a final level α_s. Higher dosages then create new defects which proceed to populate as the linear function $\alpha_L \Phi$.

Glasses and Experimental Procedure

The glass samples used in both the 85-MeV proton and 7.0-MeV electron irradiation experiments were procured from Schott Optical Glass, Incorporated (U.S.) and polished at the National Aeronautics and Space Administration's Goddard Space Flight Center. The samples were circular disks, 2.5 cm in diameter and 0.2 cm thick. Before irradiation, the glasses were transparent from the near UV (around 300 nm) to the near IR. The proton and electron ranges for each glass were much greater than the 0.2-cm thickness, thus providing a relatively uniform energy deposition throughout the sample. Three types of glass were irradiated. Using Schott nomenclature, these glasses are LaK 21 (lanthanum crown), KzFS N4 (special short flint), and LF 5 (light flint). Along with being used in space applications, they represent a wide variety of chemical composition, physical properties, and degradation effects due to irradiation (Table I).

The proton irradiations were carried out at the University of Maryland at College Park using an isochronous cyclotron. The samples were irradiated to cumulative fluences ranging from 5.0×10^{11} to 1.5×10^{14} protons/cm^2 in a scattering chamber evacuated to 10^{-6} Torr. The beam flux was between 10^{10} and 6×10^{11} protons/cm^2-sec. Determinations of flux and fluence were made with a Faraday cup and current integrator. After irradiation to a certain fluence, the samples were taken out of the chamber and their transmission spectra measured by a Perkin-Elmer model 200 spectrophotometer over the 280–700-nm wavelength region. Using peripheral interface equipment, the transmission measurements together with their corresponding wavelengths were monitored and stored using a DEC LSI-11 computer. The samples were then placed back into the chamber for further irradiation.

The electron irradiations were performed at the Space Radiations Effects Laboratory in Newport News, Virginia, using a linear electron accelerator. The glasses underwent cumulative fluences from 10^{11} to 10^{13} electrons/cm^2. A Faraday cup was used to determine the flux of each irradiation. Following each room-temperature irradiation, transmission measurements were made with a Cary-14 spectrophotometer in the 300–700-nm UV–visible region.

Transmission measurements during both the proton and electron experiments were taken approximately 1 h after irradiation. It is believed the bleaching, which occurs after irradiation, slowed sufficiently during the time that transient absorption effects decayed out, and only long-term absorption (i.e., absorption that is relatively stable at room temperature) remained.

Since ionization is the major factor in the coloration of glass, each fluence in particles/cm^2 has been converted to rads (1 rad = 100 ergs/g).[13] This measures the amount of energy that was transferred to the glasses by the incoming particle and often corresponds with the effects observed. While the conversions varied slightly depending on the density of each glass, they were ~1.2 × 10^7 p/cm^2/rad for the 85-MeV protons and ~4.5 × 10^7 e/cm^2/rad for the 7.0-MeV electrons.

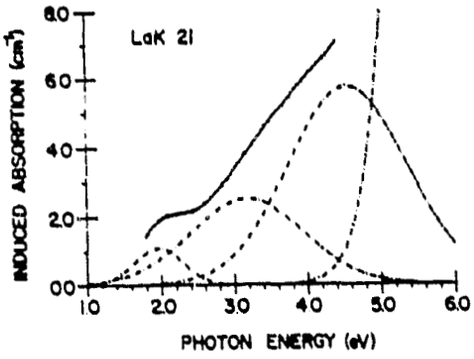

Fig. 1. The induced absorption spectrum of Schott LaK 21 after 85-MeV proton irradiation to a total dose of 3.0 × 10^5 rads. The dashed lines indicate the resolution of the spectrum into a series of Gaussian shaped bands. The solid line through the data points is the sum of the individual bands.

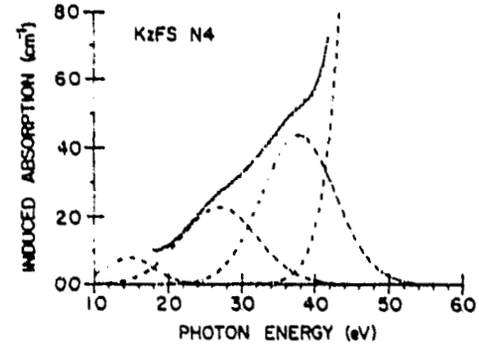

Fig. 2. The induced absorption spectrum of Schott KzFS N4 after 85-MeV proton irradiation to a total dose of 3.0 × 10^5 rads.

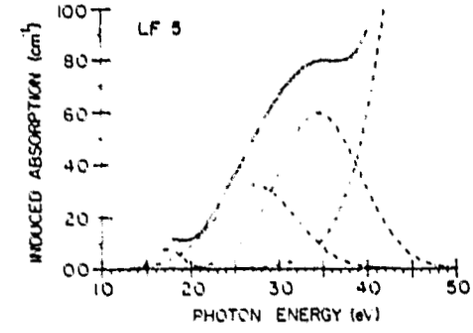

Fig. 3. The induced absorption spectrum of Schott LF 5 after 85-MeV proton irradiation to a total dose of 2.9 × 10^5 rads.

Induced Absorption Spectra

Examples of absorption spectra induced by proton irradiation of the three glasses under study are shown in Figs. 1, 2, and 3. The spectra were resolved into a series of Gaussian shaped bands using a computer program that performed a least-squares fit to a nonlinear function,[14] in this case a sum of Gaussians [each Gaussian being defined by Eq. (1)]. The solid line through the data points in each figure is the sum of the individual absorption bands (dashed lines). By inspection it can be seen that the data were fitted very accurately. All the glasses exhibited three Gaussian bands in the near UV–visible region. However, each glass had its own unique fingerprint of band energies and halfwidths. All the resolved spectra also had a fourth Gaussian located with an absorption peak fitted at 5.5 eV or above. This high energy band can be regarded as the shift in the absorption edge toward longer wavelengths as the irradiation dosage increases.

The electron-induced absorption spectra for each glass showed the same band structure as their proton-induced counterparts. As an example, in Fig. 4, it can be seen that 7.0-MeV electrons produced absorption bands in LF 5 with peaks located at the same energies as the proton-induced bands (Fig. 3). This was also true for LaK 21 and KzFS N4 The band parameters obtained from the fitting process are given in Table II. All spectra measured for each glass after the various doses could be resolved into these bands.

Where absorption bands will be located in any particular glass is dependent on a number of variables, which include whether the glass was made under reducing or oxidizing conditions, the types and amounts of impurities in the glass, and the concentration of network modifying oxides in the material.[15] Since the composition of Schott glass is proprietary information, it is beyond the scope of this study to attribute each center to a particular kind of charge carrier trap. However, other studies of multicomponent glasses have found that most color centers in the visible region can be attributed to hole-trapping.[15]

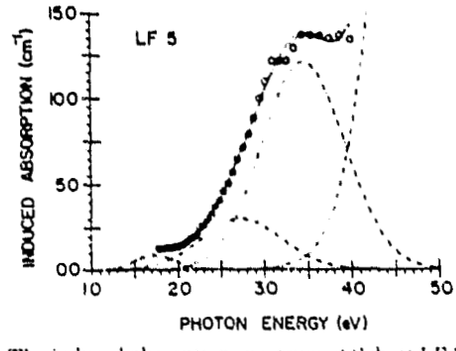

Fig. 4. The induced absorption spectrum of Schott LF 5 after 7.0-MeV electron irradiation to a total dose of 1.2 × 10^5 rads. Note that the bands are located at the same energies as the LF 5 proton-induced absorption spectrum. This was true for LaK 21 and KzFS N4 as well. However, there are minor differences in the band halfwidths generated by each type of radiation.

Table II. Absorption Spectra Components: Band Energies and Halfwidths

Type of irradiation	Glass	Band energy E_0 (eV)	Halfwidth L' (eV)
85-MeV protons	LaK 21	2.0	0.76
		3.2	1.8
		4.6	1.9
	KzFS N4	1.5	0.76
		2.7	1.2
		3.8	1.2
	LF 5	1.7	0.38
		2.7	1.1
		3.5	1.1
7.0-MeV electrons	LaK 21	2.0	0.80
		3.2	1.9
		4.6	1.9
	KzFS N4	1.5	0.8
		2.7	1.1
		3.8	1.4
	LF 5	1.7	0.55
		2.7	1.1
		3.5	1.1

Table III. Absorption Growth Parameters

Type of irradiation	Glass	λ (nm)	α_s (cm^{-1})	b (rad^{-1})
85-MeV protons	LaK 21	300	18	1.6×10^{-6}
		400	12	1.2×10^{-6}
		500	7.8	9.5×10^{-7}
		700	5.6	9.7×10^{-7}
	KzFS N4	400	11	1.3×10^{-6}
		500	6.4	1.3×10^{-6}
		700	3.4	8.8×10^{-7}
	LF 5	350	15	2.5×10^{-6}
		500	9.2	1.4×10^{-6}
		700	3.5	1.0×10^{-6}
7.0-MeV electrons	LaK 21	300	29	3.1×10^{-6}
		400	9.7	5.4×10^{-6}
		500	5.4	5.9×10^{-6}
		700	3.1	6.7×10^{-6}
	KzFS N4	400	17	2.4×10^{-6}
		500	6.7	3.8×10^{-6}
		700	2.5	4.8×10^{-6}
	LF 5	350	51	2.5×10^{-6}
		500	9.8	4.1×10^{-6}
		700	2.2	6.4×10^{-6}

Induced Absorption Growth Curves

As noted earlier, growth of induced absorption in any one band with increasing dose of irradiation has been accurately described in previous studies by Eq. (3). However, when an absorption spectrum consists of bands reasonably separated (as is the case in this investigation), Eq. (3) can also be used to describe the growth of the total induced absorption at a particular wavelength λ. For spectra which meet this condition, this simplifies the equation's use in practical applications. It has been reported that the $\alpha_L \Phi$ term can be set to zero since its contribution is negligible in the dose range under consideration ($\leq 10^7$ rads).[16] Thus, data obtained from both proton and electron irradiations of the glasses were fitted to the expression

$$\alpha(\lambda,\Phi) = \alpha_s[1 - \exp(-b\Phi)], \quad (4)$$

using a least-squares procedure. Constants α_s and b are dependent on λ and glass type. Their values were calculated at selected wavelengths, which spanned the entire spectrum under investigation. Some results for each glass are listed in Table III.

It can be seen from Table III that, while α_s changed rapidly with decreasing wavelength in all three glasses, the growth constant b remained relatively stable. For any one glass, b changed by no more than a factor of 2–3 for both the proton- and electron-generated growth curves. All the glasses had values for b falling in the same range (i.e., around 1.2×10^{-6} rad^{-1} for the proton-induced degradation data and about 5.0×10^{-6} rad^{-1} for the electron-induced degradation data). This behavior is consistent with previous findings on Schott glass[16] and provides a means for making rough estimations of the radiation-induced coloring of similar glass types.

Several absorption growth curves for LaK 21 after proton irradiation are shown in Fig. 5. Such curves typify the responses of all three glasses after either proton or electron irradiation. The solid line through the data points was computed using the constants α_s and b from the fitting process and indicates that Eq. (4) reasonably describes the growth of induced absorption at the selected wavelengths. The growth proceeded linearly on a log scale at the lower doses and then quickly attained a saturation level for a dose of around 10^6 rads. This same behavior has been reported in other types of electron-irradiated Schott glass.[11]

Comparison of Proton- and Electron-Induced Coloring

It has been shown that proton irradiation of the three glasses produced absorption bands with peaks at the same energies as those produced by electron irradiation. This agrees with the current model of coloration, which views the energies of color centers as being dependent on the glass, its defects, and composition. It was also shown that protons and electrons induced the same type of absorption growth with increasing dose. For doses up to 10^7 rads, the induced absorption α at wavelength λ exhibited a saturating exponential growth, thus providing the means to predict degradation in any of the three glasses for a particular fluence of proton or electron irradiation. However, the protons and electrons did not induce the same saturation levels α_s in any one

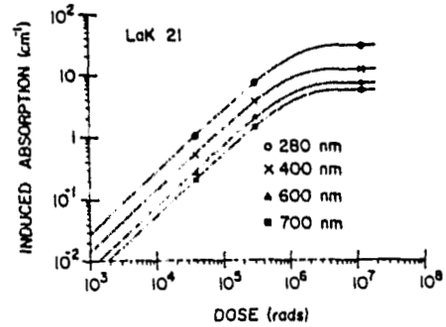

Fig. 5. The growth of induced absorption for Schott LaK 21 with an increasing dose of 85-MeV protons at selected wavelengths. All the glasses exhibited this saturating exponential growth during both the proton and electron irradiations for doses up to 10^7 rads.

glass for certain areas of the spectrum. In fact, a pattern is discerned as one compares the values of α_s in Table III. While the protons produced a higher absorption saturation level than the electrons at the longer wavelengths (around 700 nm), the reverse occurred in the shorter wavelengths (around 300 nm). In that area of the spectrum, the electrons induced a greater absorption.

The differences are not extreme at either end of the 280–700-nm spectrum, yet they are still larger than the fitted standard deviations (0.1–4%) of the saturating levels. For the three glasses tested, this indicates that the protons formed more low energy color centers at the saturation level than the electrons, while the electrons created a greater number of stable centers at the higher energies (at least for the range of energies being investigated). Should this finding hold for other glass types as well, it suggests that one must be careful in taking degradation effects produced by one type of charged particle and extrapolating effects produced by another type of radiation.

The authors express sincere thanks to W. Fowler and C. Reft for their help in the data acquisition and to L. C. Smith for assistance in the data analysis and computer graphing. This work has been supported by NASA grant NSG-5053.

References

1. J. Becher, C. S. Reft, and R. L. Kernell, "Radiation Studies of Optical and Electronic Components Used in Astronomical Satellite Studies," Old Dominion University Technical Report PGSTR-PH77-55 (1977).
2. E. Lell, N. Kreidl, and J. R. Hensler, in *Progress in Ceramic Science, Vol. 4*, J. E. Burke, Ed. (Pergamon, Oxford, 1966).
3. R. A. Wullaert *et al.*, in *Effects of Radiation on Materials and Components*, J. F. Kircher and R. E. Bowman, Eds. (Reinhold, New York, 1964).
4. As used in this paper, an absorption k is defined by Lambert's law $I = I_0 \exp(-kx)$, where I_0 is the light intensity entering the material, and I is the intensity after passage through a thickness x. Transmission T is defined as I/I_0.
5. P. W. Levy, J. Am. Ceram. Soc. 43, 389 (1960).
6. K. Lengweiler, P. L. Mattern, and P. W. Levy, Phys. Rev. Lett. 26, 1375 (1971).
7. P. W. Levy, P. L. Mattern, and K. Lengweiler, Phys. Rev. Lett. 24, 13 (1970).
8. P. W. Levy *et al.*, J. Am. Ceram. Soc. 57, 176 (1974).
9. P. L. Mattern, K. Lengweiler, and P. W. Levy, Solid State Commun. 9, 935 (1971).
10. M. Goldberg *et al.*, Nucl. Instrum. Methods 108, 119 (1973).
11. M. J. Treadaway, B. C. Passenheim, and B. D. Kitterer, "Transient Radiation Effects in Optical Materials," SAMSO-TR-75-174 (1975).
12. Schott Optical Glass catalog.
13. With the absorbed dose nearly uniform throughout the material, the fluence is converted to rads through the following equation: Dose = $1/\rho\ \Phi\ dE/dt \cdot 1.6 \times 10^8$ rads, where ρ is the density of the irradiated material in g/cm^3, Φ is the fluence in particles/cm^2, and dE/dt is the particle's stopping power in MeV/cm.
14. P. R. Bevington, *Data Reduction and Error Analysis for the Physical Sciences* (McGraw-Hill, New York, 1969).
15. A. Bishay, J. Non-Cryst. Solids 3, 54 (1970).
16. M. J. Treadaway, B. C. Passenheim, and B. D. Kitterer, IEEE Trans. Nucl. Sci. NS-22, 2253 (1975).

APPENDIX B

LIST OF PAPERS PRESENTED AT PROFESSIONAL MEETINGS

1. Becher, J.; Kernell, R.L.; and Reft, C.S.: Electron-Induced Luminescence in Ultraviolet Converter. Am. Phys. Soc., Vol. 22, 1977, p. 491. Presented at meeting of Southeast Section, Am. Physical Soc., Nov. 1976.

2. Reft, C.S.; Becher, J.; and Kernell, R.L.: The Effect of Electron Irradiation on an Image Dissector Tube: Bull. Am. Phys. Soc., Vol. 22, 1977, p. 499. Presented at meeting of Southeast Section, Am. Physical Soc., Nov. 1976.

3. Smith, L.C.; and Becher, J.: Special Image Effects in UV Converter During Electron Irradiation. Bull. Am. Phys. Soc., Vol. 22, 1977, p. 491. Presented at meeting of Southeastern Section, Am. Physical Soc., Nov. 1976.

4. Smith, L.C.; Becher, J., and Reft, C.S.: Photographic Technique for Analyzing the Effects of Irradiation on a UV Converter. Presented at meeting of Virginia Academy of Science, May 1976.

5. Reft, C.S.; and Becher, J.: The Electron Radiation Effects of Silicon Photodiodes. Bull. Am. Phys. Soc., Vol. 22, 1977, p. 42. Presented at meeting of Am. Physical Soc., Jan. 1977.

6. Reft, C.S.; Becher, J.; and Kernell, R.L.: Electron Radiation Effects on Silicon Photodiodes. Presented at IEEE Space Radiation Effects Conf. (Williamsburg, Va.), July 1977.

7. Reft, C.S.; and Becher, J.: The Effects of Proton and Electron Radiation on PIN Photodiodes. Bull. Am. Phys. Soc., Vol. 25, 1980, p. 313. Presented at meeting of Am. Physical Soc. (Chicago), Jan. 1980.

REFERENCES

Bartusiak, M.F.; and Becher, J.: Proton-Induced Coloring of Multicomponent Glasses. J. Appl. Opt., Vol. 18, Oct. 1979, pp. 3342-3346.

Baze, M.; Firminhac, R.H.; Horne, W.E.; Kennedy, R.C.; Measel, P.R.; Sivo, L.L.; and Wilkinson, M.C.: Radiation and Shielding Study for the International Ultraviolet Explorer, Boeing Report No. D180-18486-1, 1974.

Corbett, J.: Electron Radiation Damage in Semi-Conductors and Metals. Academic Press, 1966.

Dexter, D.L.: Phys. Rev., Vol. 101, 1956, p. 48.

Fischer, F.: Z. Physik, Vol. 154, 1959, p. 534.

Gärtner, W.: Phys. Rev., Vol. 116, 1959, p. 84.

Levy, Paul W.: J. Amer. Ceramic Soc., Vol. 43, 1960, p. 389.

Matare, H.: Defect Electronics in Semiconductors. Wiley-Interscience, 1971.

Skeldon, Mark D.: The Effects of Electron Irradiation on MOSFETS. Master's Thesis, Old Dominion University, Norfolk, Virginia, 1977.

Smakula, A.: Z. Physik, Vol. 59, 1930, p. 603.

Viehmann, W.; Eubanks, A.G.; Pieper, G.F.; and Bredekamp, J.H.: Appl. Opt., Vol. 14, 1975, p. 2101.

Table 1. Response of FES to irradiation with ^{90}Sr.

Filter (nm)	Positions Summed	Summed Count Rates ($\times 10^3$ counts/sec) Before	After	Day After
427.8	1-5	3.8	3.1	3.7
	6-10	4.7	4.5	4.8
	11-15	4.8	4.3	4.3
	16-20	4.7	4.5	4.6
	21-25	4.8	4.6	4.7
	1-25	22.8	21.0	22.1
530.0	1-5	32.8	29.7	31.4
	6-10	41.3	40.0	40.2
	11-15	41.1	39.8	41.2
	16-20	42.9	40.4	42.6
	21-25	42.6	40.6	42.3
	1-25	200.7	190.5	197.7
630.0	1-5	50.2	49.1	49.5
	6-10	68.3	63.0	69.0
	11-15	69.0	66.0	68.2
	16-20	69.9	67.0	69.0
	21-25	72.0	68.0	71.8
	1-25	329.4	313.1	327.5

Table 2. Transmission characteristics of LaK 21, KzFS N4, and LF 5 after 85-MeV proton irradiation.

Glass	Wavelength (Å)	Transmission Before Irradiation	Transmission After 1.5E14 p/cm^2	Percent Change
LaK 21	6800	0.93	0.36	61
	4000	0.93	0.13	86
	3000	0.63	0.03	95
KzFS N4	6800	0.93	0.50	46
	4000	0.91	0.12	87
	3000	0.31	0.00	100
LF 5	6800	0.90	0.43	52
	4000	0.90	0.04	96
	3000	0.003	0.00	100

Table 3. LaK 21-induced absorption spectra components for 85-Mev proton and 7.0-MeV electron irradiations.

Type of Irradiation	Dose (rad)	E_o (eV)	α_m (cm^{-1})	U (eV)
Proton	3.8E4	2.0	0.20	1.0
		3.2	0.34	1.2
		4.6	1.2	1.8
	3.0E5	2.0	1.1	0.76
		3.2	2.5	1.8
		4.6	5.8	1.9
	1.2E7	2.0	4.0	0.81
		3.2	8.5	1.8
		4.6	14.0	2.0
Electron	2.1E4	2.0	0.31	0.80
		3.2	0.69	1.9
		4.6	1.6	1.9
	1.0E5	2.0	1.2	0.80
		3.2	2.8	1.9
		4.6	7.7	1.9
	2.1E5	2.0	1.9	0.84
		3.2	4.1	2.0
		4.6	12.0	1.9

Standard Deviations Protons: E_o = ±0.3% α_m = ±2% U = ±2%

Standard Deviations Electrons: E_o = ±0.2% α_m = ±1% U = ±1%

Table 4. KzFS N4-induced absorption spectra components for 85-MeV proton and 7 0-MeV electron irradiations.

Type of Irradiation	Dose (rad)	E_o (eV)	α_m (cm^{-1})	U (eV)
Proton	3.9E4	1.5	0.00016	0.69
		2.7	0.24	1.3
		3.8	0.65	1.3
	3.0E5	1.5	0.80	0.76
		2.7	2.3	1.2
		3.8	4.4	1.2
	1.3E7	1.5	3.5	0.63
		2.7	6.0	1.3
		3.8	12.0	1.4
Electron	2.4E4	1.5	0.40	0.8
		2.7	0.52	1.1
		3.8	1.0	1.4
	1.2E5	1.5	0.90	0.8
		2.7	2.3	1.1
		3.8	5.6	1.4
	2.4E5	1.5	1.6	0.8
		2.7	3.5	1.1
		3.8	9.6	1.4

Standard Deviations Protons: E_o = ±0.3% α_m = ±2% U = ±2%

Standard Deviations Electrons: E_o = ±0.2% α_m = ±6% U = ±6%

Table 5. LF 5-induced absorption spectra components for 85-MeV proton and 7.0-MeV electron irradiations.

Type of Irradiation	Dose (rad)	E_o (eV)	α_m (cm^{-1})	U (eV)
Proton	4.1E4	1.7	0.04	0.56
		2.7	0.44	1.0
		3.5	1.1	1.1
	2.9E5	1.7	0.77	0.38
		2.7	3.2	1.1
		3.5	6.0	1.1
	1.3E7	1.7	2.7	0.43
		2.7	9.1	1.1
		3.5	10.0	1.1
Electron	2.4E4	1.7	0.18	0.42
		2.7	0.75	1.1
		3.5	2.2	1.1
	1.2E5	1.7	0.86	0.55
		2.7	3.0	1.1
		3.5	12.0	1.1
	2.4E5	1.7	1.1	0.39
		2.7	5.4	1.1
		3.5	16.0	1.0

Standard Deviations Protons: E_o = ±0.4% α_m = ±2% U = ±2%

Standard Deviations Electrons: E_o = ±1% α_m = ±7% U = ±7%

Table 6. LaK 21 color center densities after 85-MeV proton and 7.0-MeV electron irradiations.

Type of Irradiation	Dose (rad)	E_o (eV)	N (cm^{-3})
Proton	3.8E4	2.0	1.3E15
		3.2	2.6E15
		4.6	1.4E16
	3.0E5	2.0	5.4E15
		3.2	3.0E16
		4.6	7.1E16
	1.2E7	2.0	2.1E16
		3.2	1.0E17
		4.6	1.9E17
Electron	2.1E4	2.0	1.6E15
		3.2	8.5E15
		4.6	1.9E16
	1.0E5	2.0	6.0E15
		3.2	3.4E16
		4.6	9.5E16
	2.1E5	2.0	1.0E16
		3.2	5.2E16
		4.6	1.5E17

Standard Deviation Proton: N = ±3%

Standard Deviation Electron: N = ±1.4%

Table 7. KzFS N4 color center densities after 85-MeV proton and 7.0-MeV electron irradiations.

Type of Irridation	Dose (rad)	E_o (eV)	N (cm^{-3})
Proton	3.9E4	1.5	7.2E11
		2.7	2.1E15
		3.8	5.6E15
	3.0E5	1.5	4.0E15
		2.7	1.9E16
		3.8	3.5E16
	1.3E7	1.5	1.5E16
		2.7	5.1E16
		3.8	1.1E17
Electron	2.4E4	1.5	2.1E15
		2.7	3.8E15
		3.8	9.6E15
	1.2E5	1.5	4.8E15
		2.7	1.7E16
		3.8	5.1E16
	2.4E5	1.5	8.6E15
		2.7	2.6E16
		3.8	8.7E16

Standard Deviation Proton: N = ±3%

Standard Deviation Electron: N = ±8%

Table 8. LF 5 color center densities after 85-MeV proton and 7.0-MeV electron irradiations.

Type of Irradiation	Dose (rad)	E_o (eV)	N (cm^{-3})
Proton	4.1E4	1.7	1.6E14
		2.7	3.1E15
		3.5	8.0E15
	2.9E5	1.7	2.0E15
		2.7	2.4E16
		3.5	4.5E16
	1.3E7	1.7	7.9E15
		2.7	6.6E16
		3.5	7.6E16
Electron	2.4E4	1.7	5.2E14
		2.7	5.6E15
		3.5	1.7E16
	1.2E5	1.7	3.2E15
		2.7	2.2E16
		3.5	9.2E16
	2.4E5	1.7	3.0E15
		2.7	4.0E16
		3.5	1.2E17

Standard Deviation Proton: N = ±3%

Standard Deviation Electron: N = ±9%

Table 9. Color center density growth parameters for 85-MeV proton and 7.0-MeV electron irradiations.

Glass	Type of Irradiation	E_o (eV)	A' (cm^{-3})	b (rad^{-1})	A'b (cm^{-3} rad^{-1})
LaK 21	Proton	2.0	2.1E16	1.0E-6	2.1E10
		3.2	1.0E17	1.2E-6	1.2E11
		4.6	1.9E17	1.6E-6	3.0E11
	Electron	2.0	1.5E16	5.2E-6	7.8E10
		3.2	7.1E16	6.3E-6	4.5E11
		4.6	2.7E17	4.1E-6	1.1E12
KzFS N4	Proton	1.5	1.5E16	1.0E-6	1.5E10
		2.7	5.1E16	1.5E-6	7.7E10
		3.8	1.1E17	1.3E-6	1.4E11
	Electron	1.5	1.4E16	3.8E-6	5.3E10
		2.7	3.7E16	5.0E-6	1.9E11
		3.8	1.9E17	2.6E-6	4.9E11
LF 5	Proton	1.7	7.9E15	9.9E-7	7.8E09
		2.7	6.6E16	1.5E-6	9.9E10
		3.5	7.6E16	3.1E-6	2.4E11
	Electron	1.7	3.4E15	1.4E-5	4.8E10
		2.7	1.1E17	2.0E-6	2.2E11
		3.5	1.4E17	7.8E-6	1.1E12

Standard Deviations Protons: A' = ±7% b = ±3%

Standard Deviations Electrons: A' = ±10% b = ±2%

Table 10. Threshold changes for p and n channels.

VG	VS	No. of Runs	Change in threshold (V/Mrad)		
5	0	2	-10.92	-12.79	
5	10	2	-18.32	-17.68	
0	0	2	-4.08	-5.40	
0	10	2	-23.31	-21.21	
-5	0	10	-18.42	-21.76	
-5	10	3	-32.11	-30.21	-35.71
	p-Channel MOSFETs				
5	0	2	-3.02	-3.10	
5	10	1	-2.53		
0	0	2	-2.53	-0.51	
0	10	2	-4.34	-3.05	
-5	0	2	-17.78	-17.03	
-5	10	1	-16.91		
	n-Channel MOSFETs				

Table 11. Characteristics of silicon PIN photodiodes irradiated with electrons (^{90}Sr) and protons.

Diode Type	Resistivity (ohm-cm)	AR Coating (nm)	Active Area (cm^2)
A	400	0	0.20
A*	400	0	0.20
B	400	200	0.20
G	400	400	0.20
R	10	0	0.20

A* is the same as A, but is encapsulated and covered with Corning 7052 glass window.

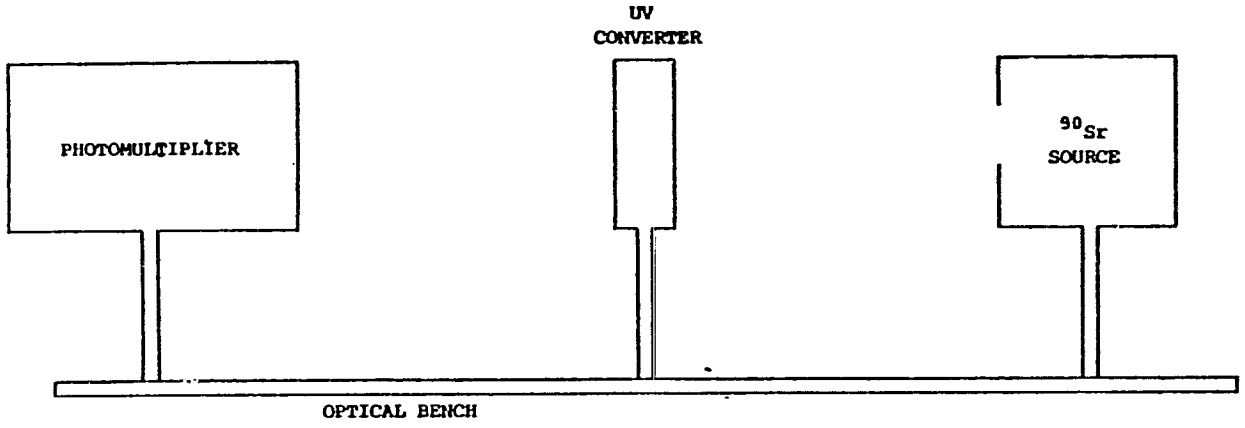

Figure 1. Sketch of experimental arrangement for ^{90}Sr radiation of UV converter (image intensifier).

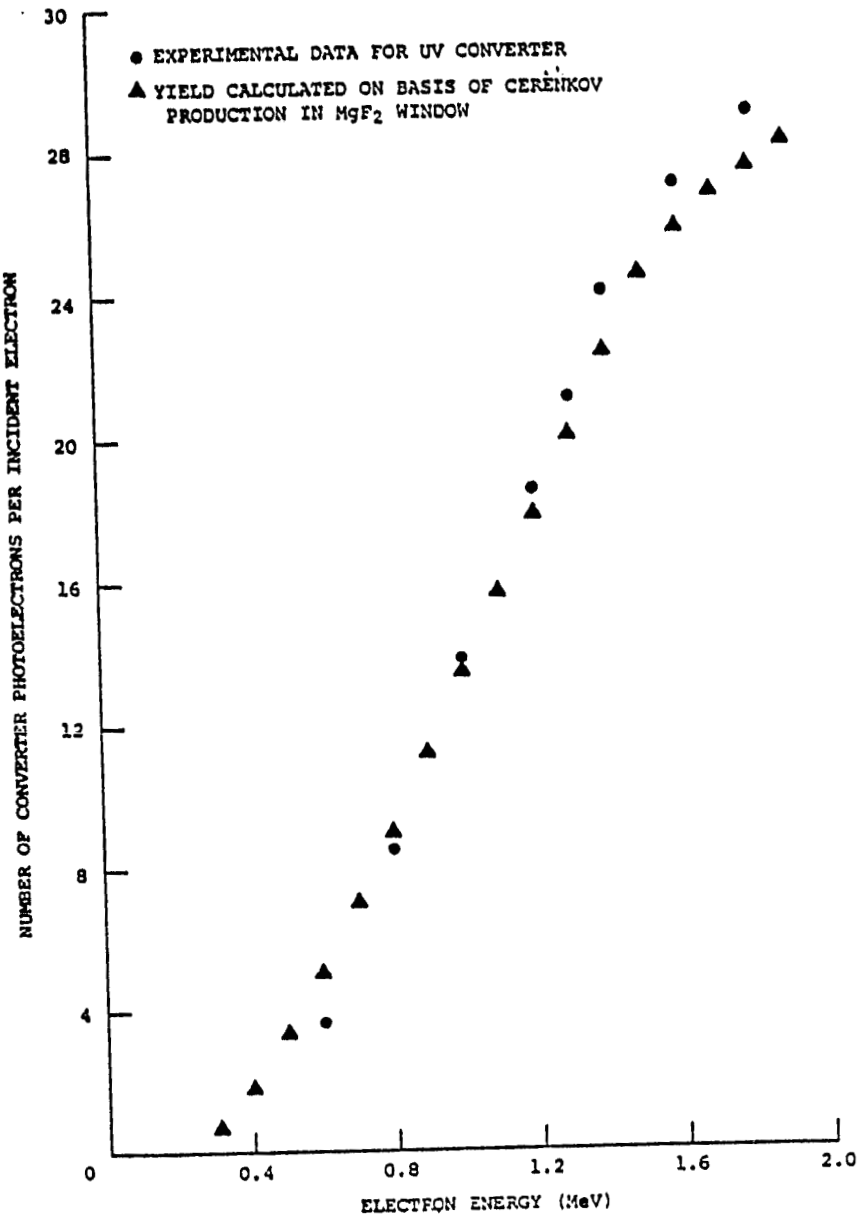

Figure 2. Energy dependence of the electron-induced signal in ITT UV converter model No. F4122.

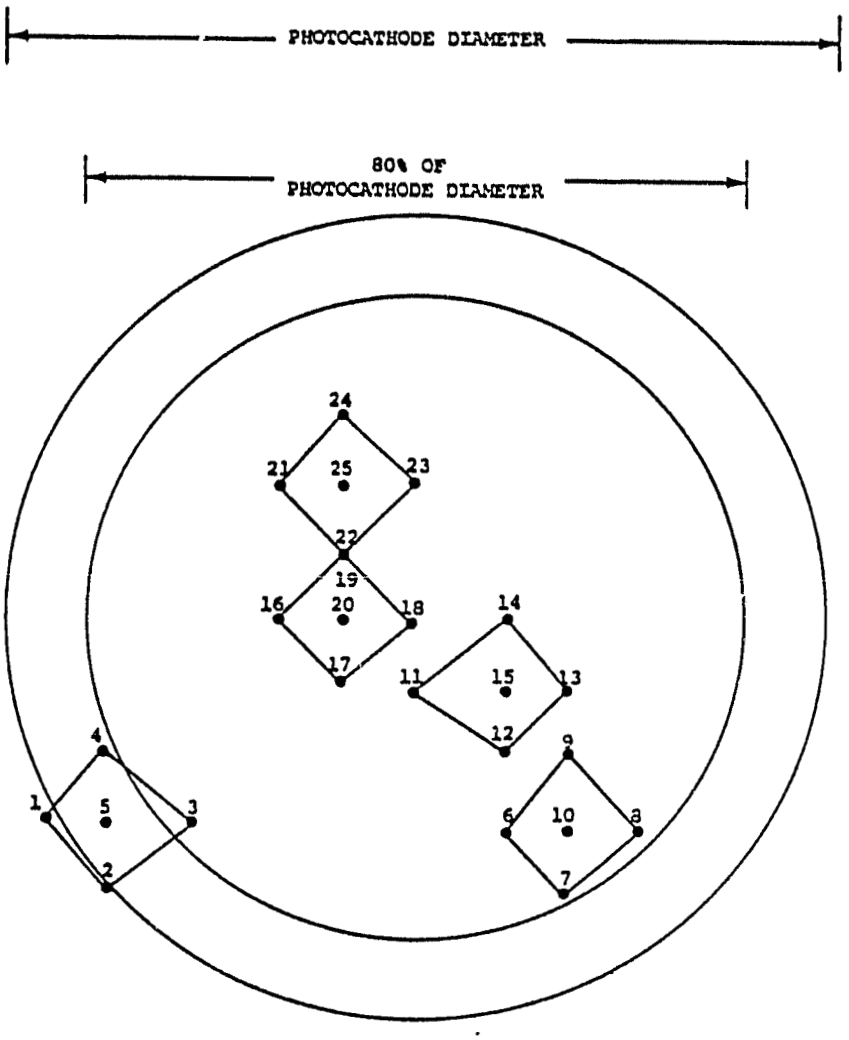

Figure 3. Surface of the image dissector photocathode.

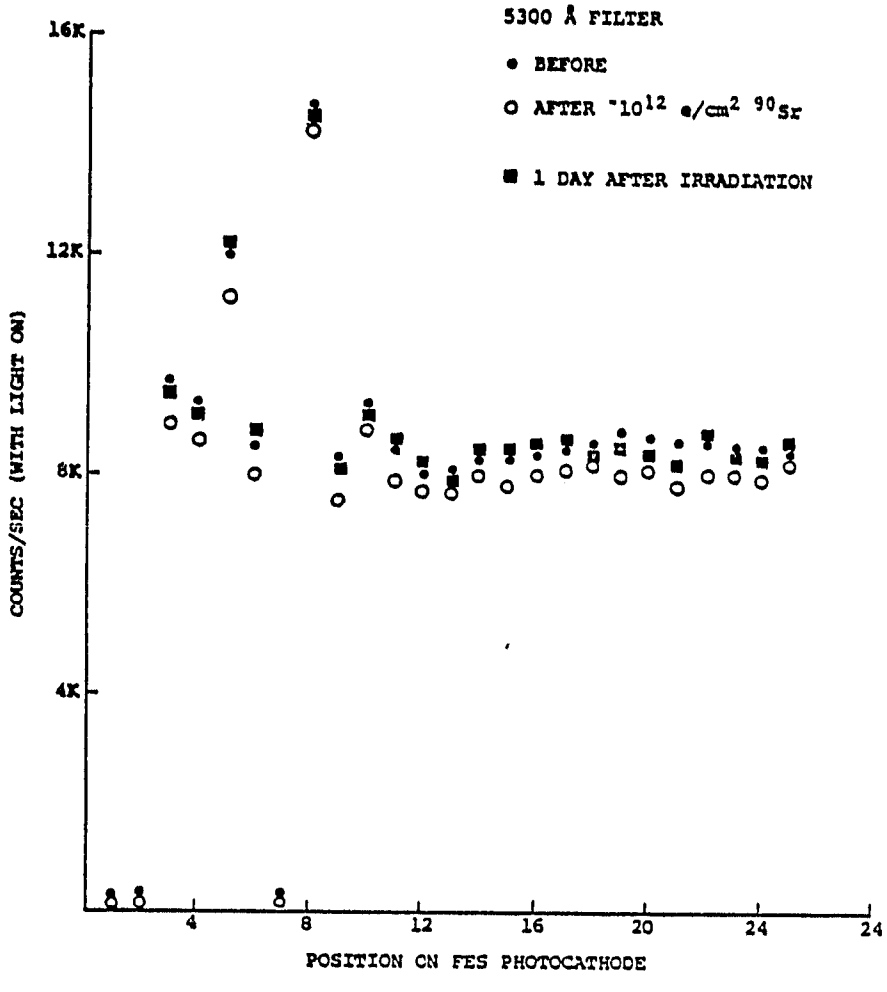

Figure 4. Count rate vs. position on surface of photocathode for the 530-nm filter before and after exposure to ^{90}Sr radiation.

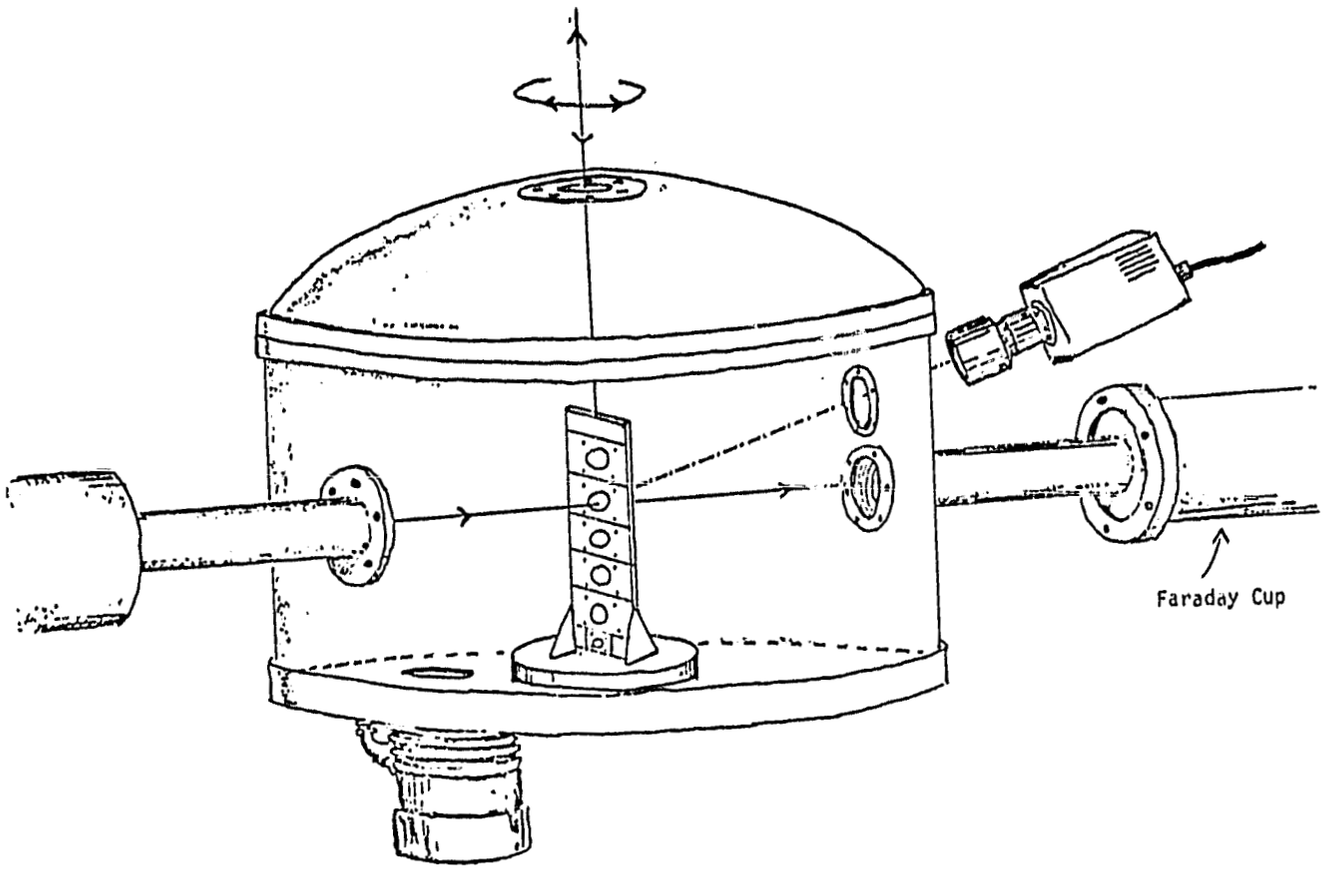

Figure 5. Schematic of scattering chamber, sample holder, and Faraday cup for proton irradiation.

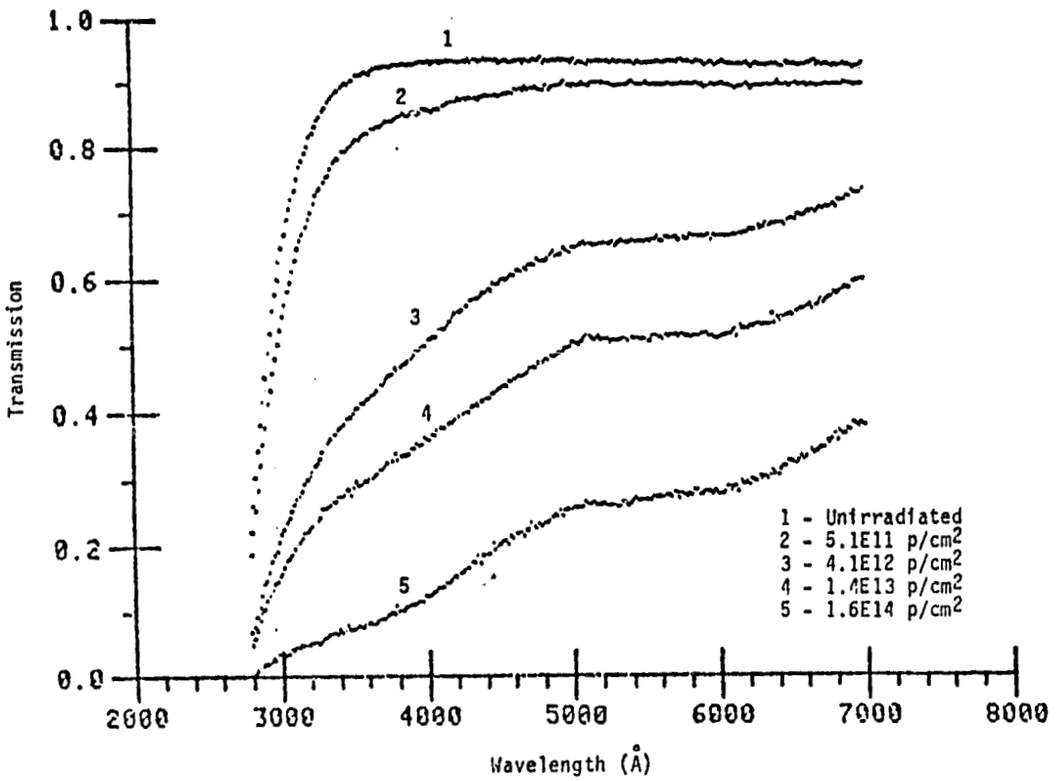

Figure 6. Transmission spectra of LaK 21 at several fluences of 85-MeV proton radiation.

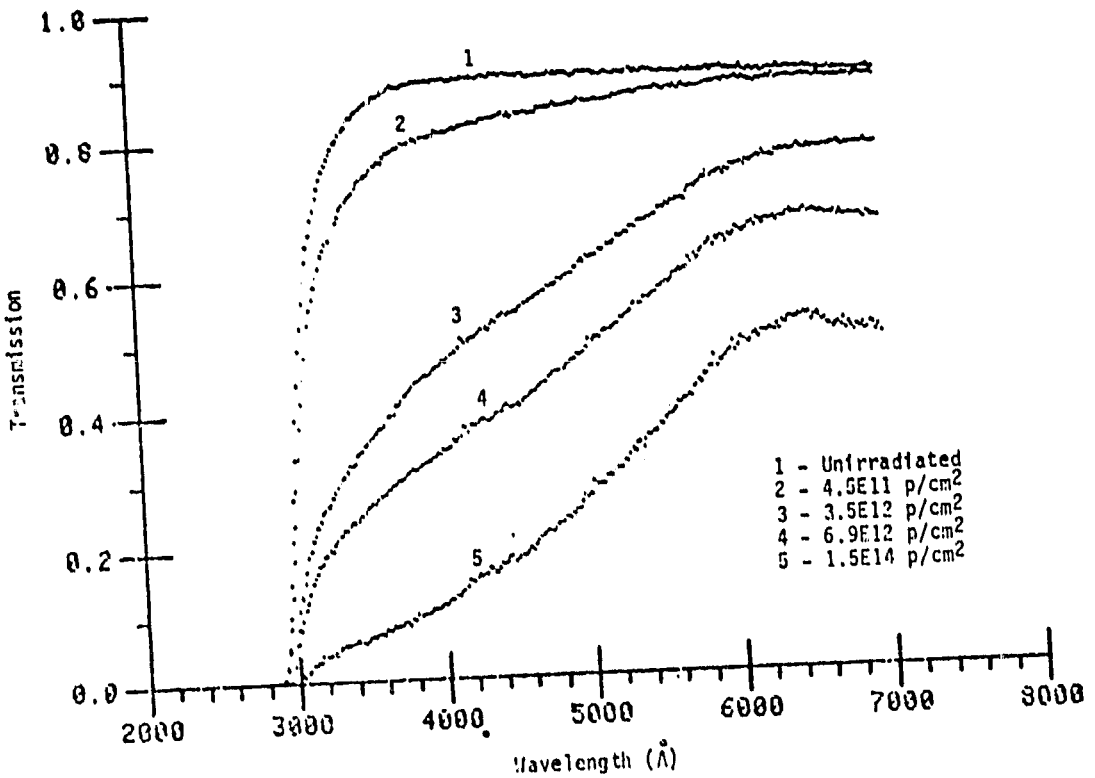

Figure 7. Transmission spectra of KzFS N4 at several fluences of 85-MeV proton radiation.

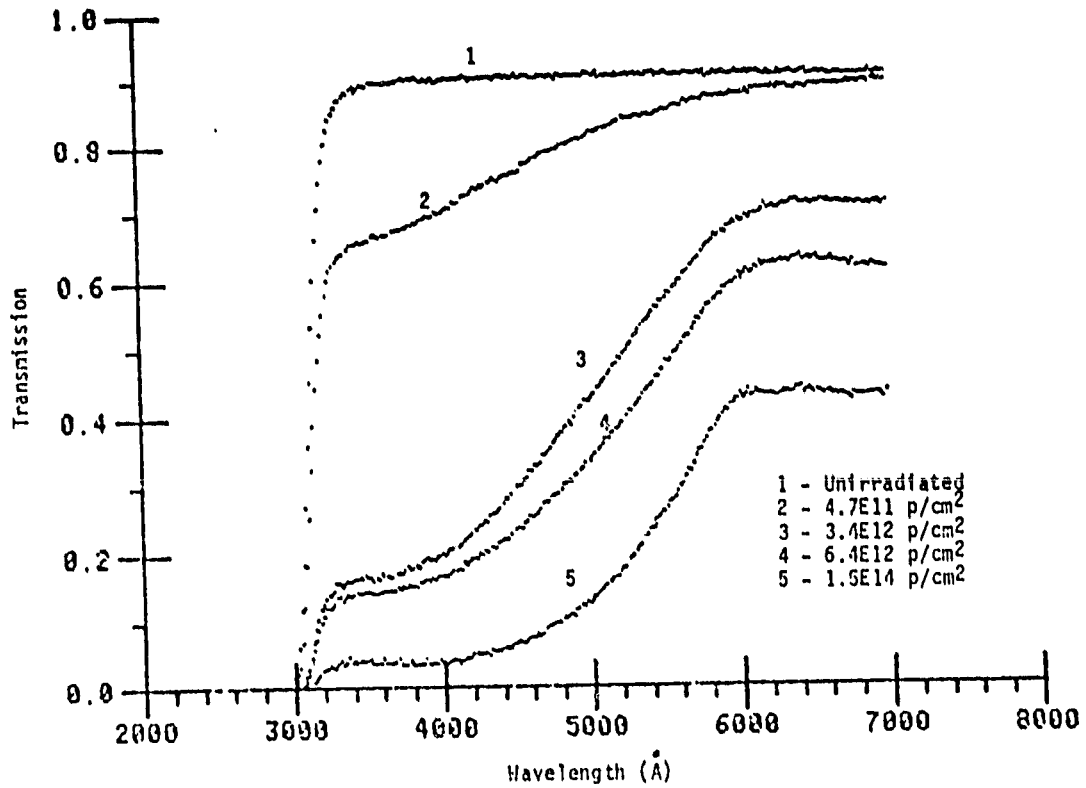

Figure 8. Transmission spectra of LF 5 at several fluences of 85-Mev proton radiation.

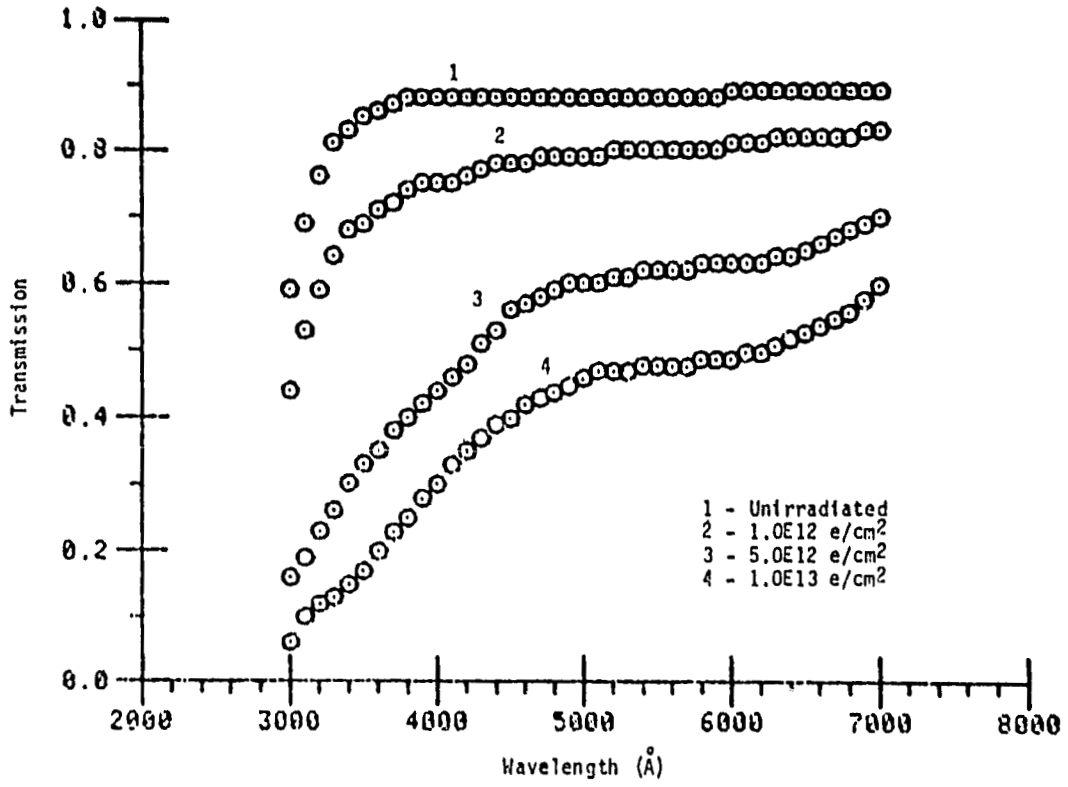

Figure 9. Transmission spectra of LaK 21 at several fluences of 7.0-MeV electron radiation.

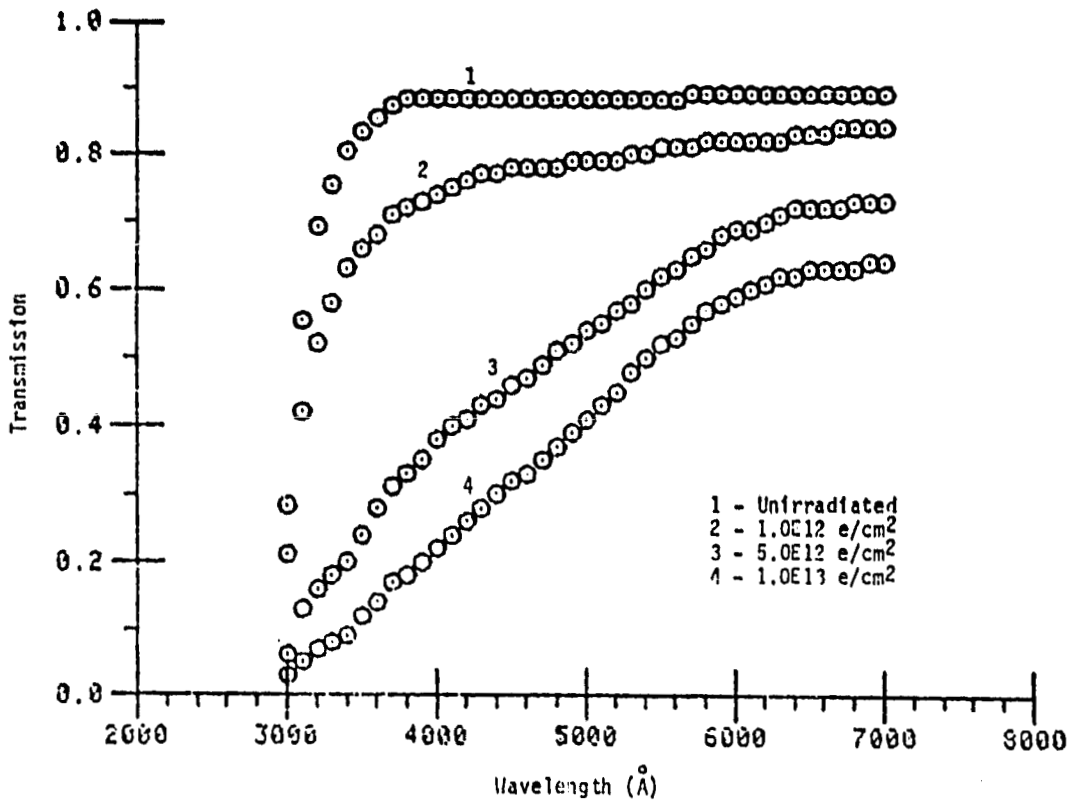

Figure 10. Transmission spectra of KzFS N4 at several fluences of 7.0-MeV electron radiation.

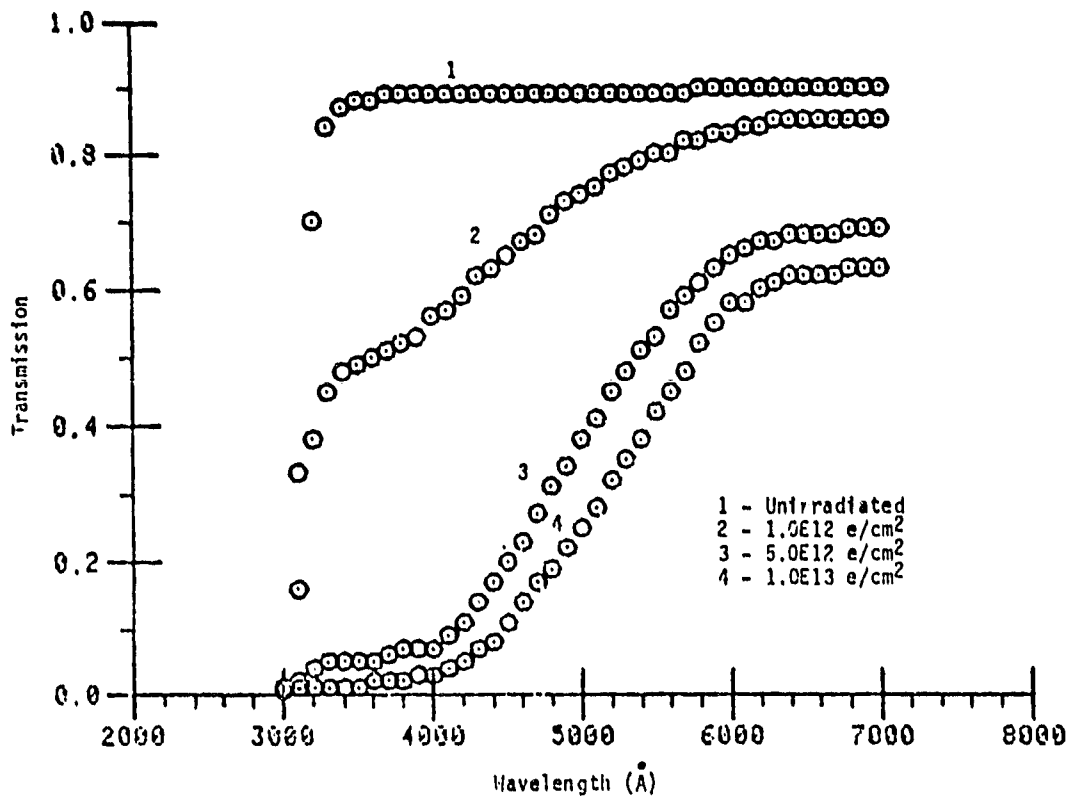

Figure 11. Transmission spectra of LF 5 at several fluences of 7.0-MeV electron radiation.

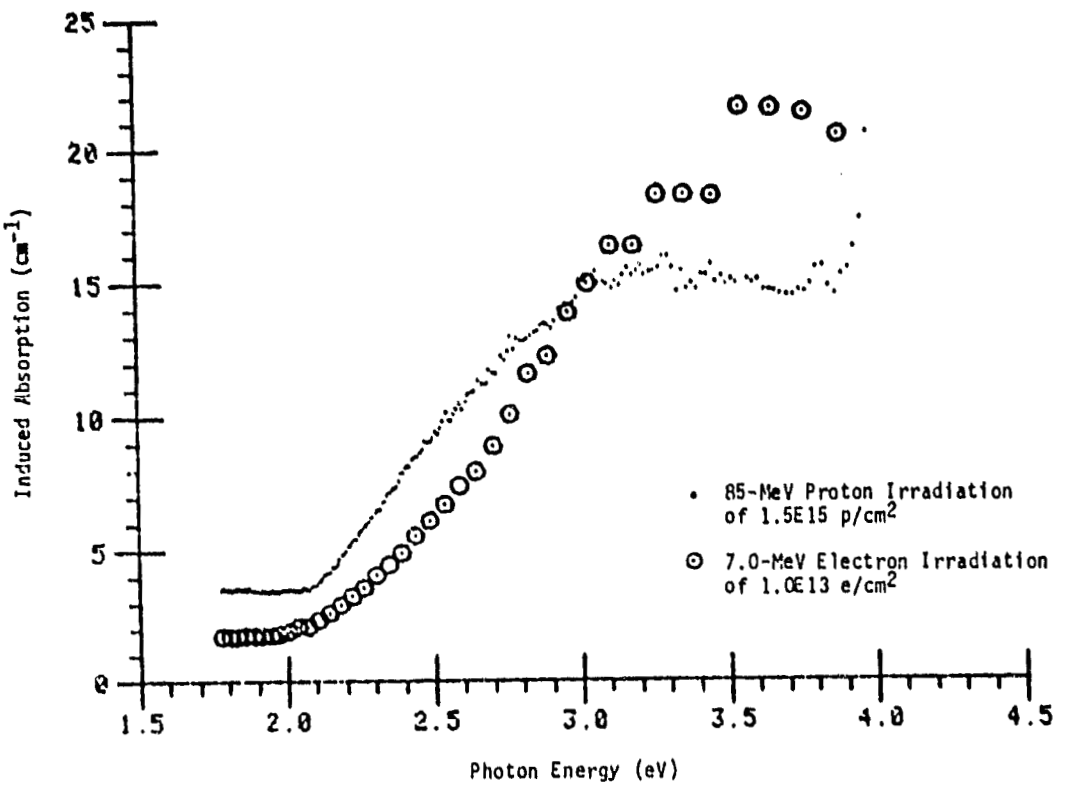

Figure 12. Comparison of induced absorption spectra for LF 5 after 85-MeV proton and 7.0-MeV electron irradiations.

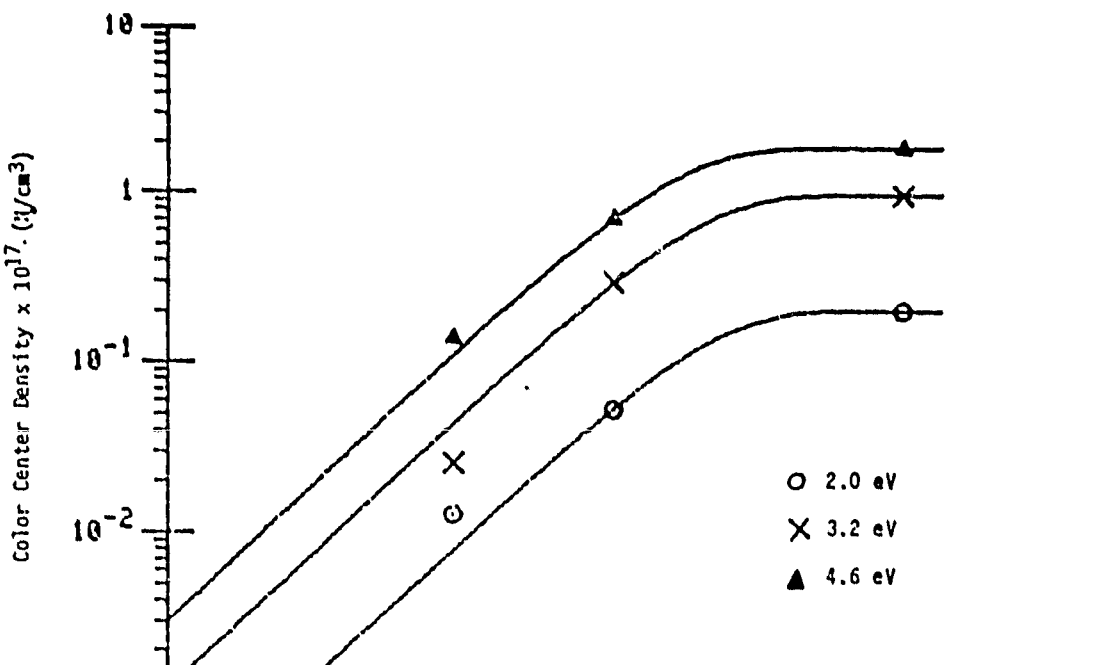

Figure 13. Growth of color center densities with increasing dose of 85-MeV protons for LaK 21.

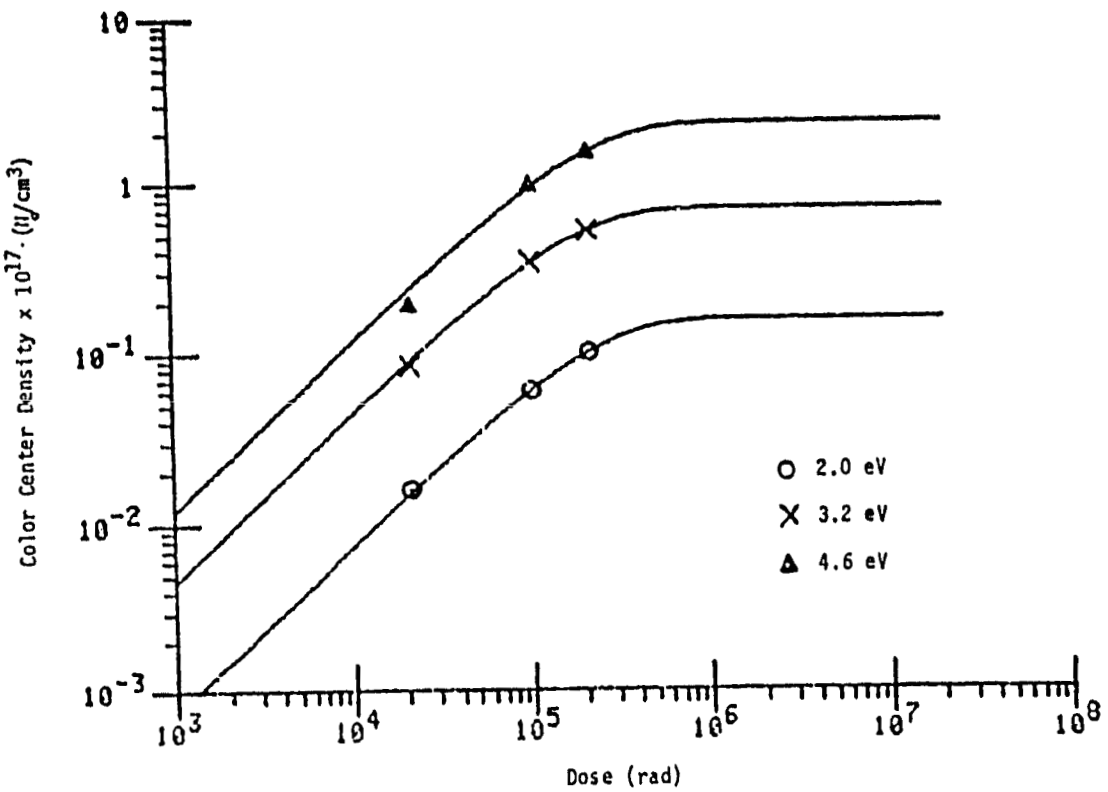

Figure 14. Growth of color center densities with increasing dose of 7.0-MeV electrons for LaK 21.

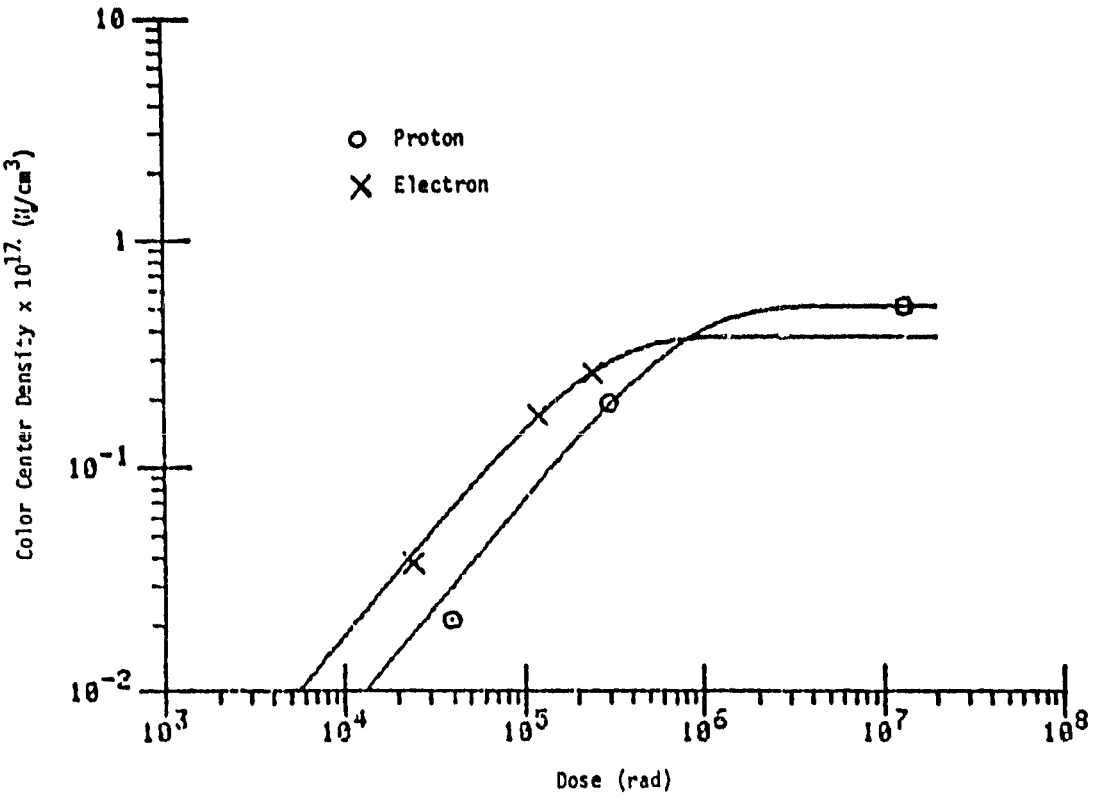

Figure 15. Color center density growth curves for KzFS N4 at 2.7-eV absorption band after 85-MeV proton and 7.0-MeV electron irradiations.

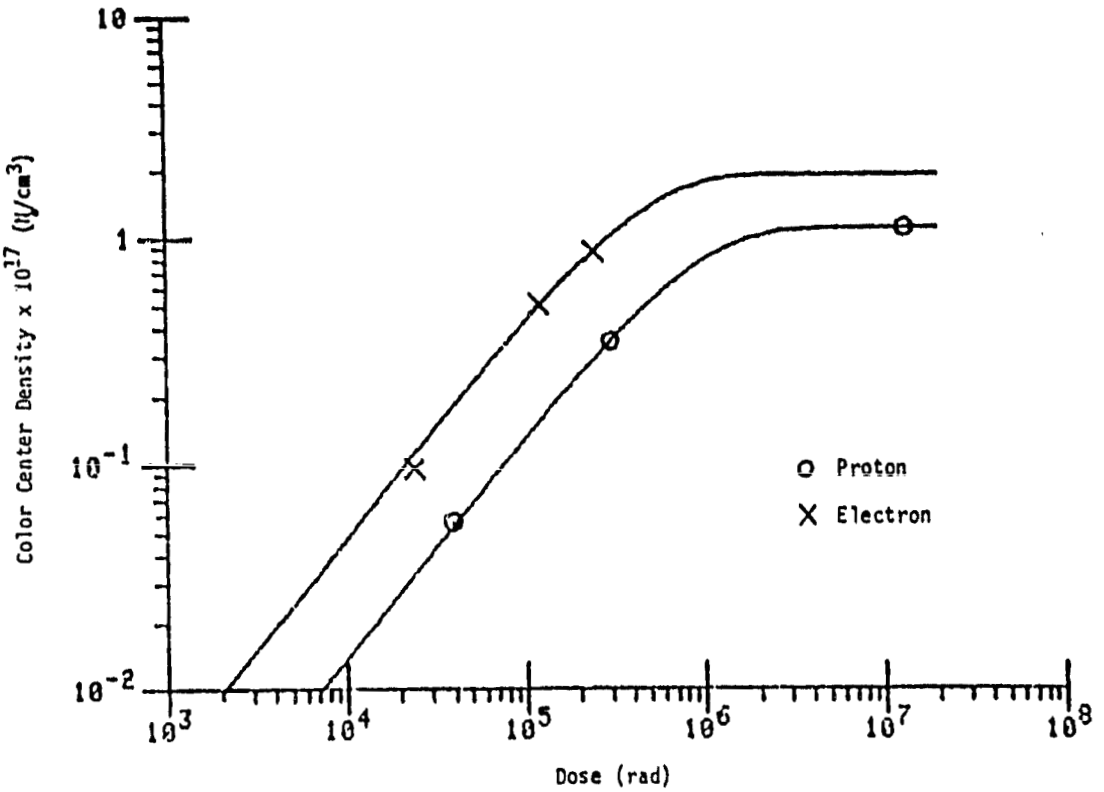

Figure 16. Color center density growth curves for KzFS N4 at 3.8-eV absorption band after 85-MeV proton and 7.0-MeV electron irradiations.

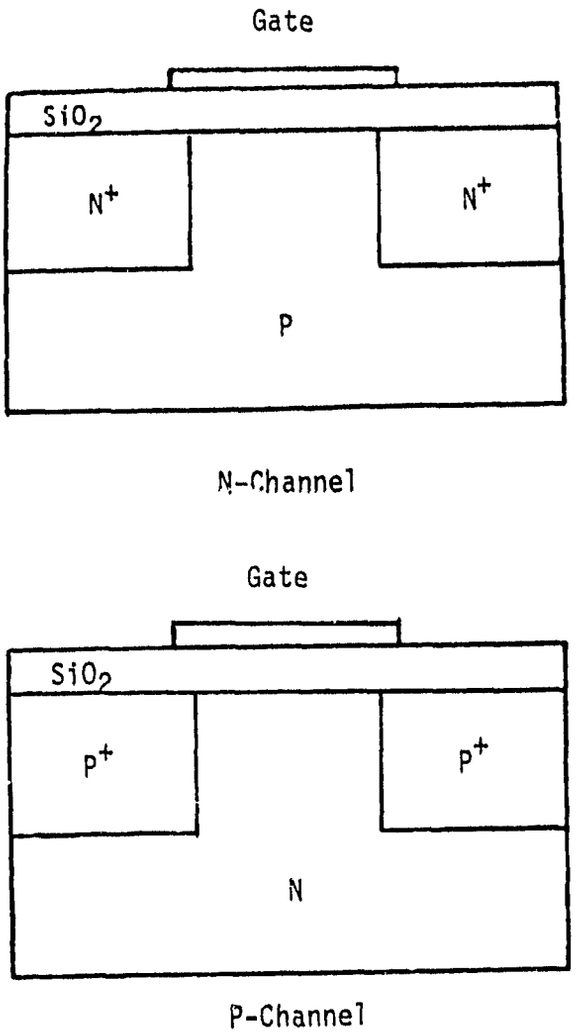

Figure 17. Enhancement mode MOSFETs.

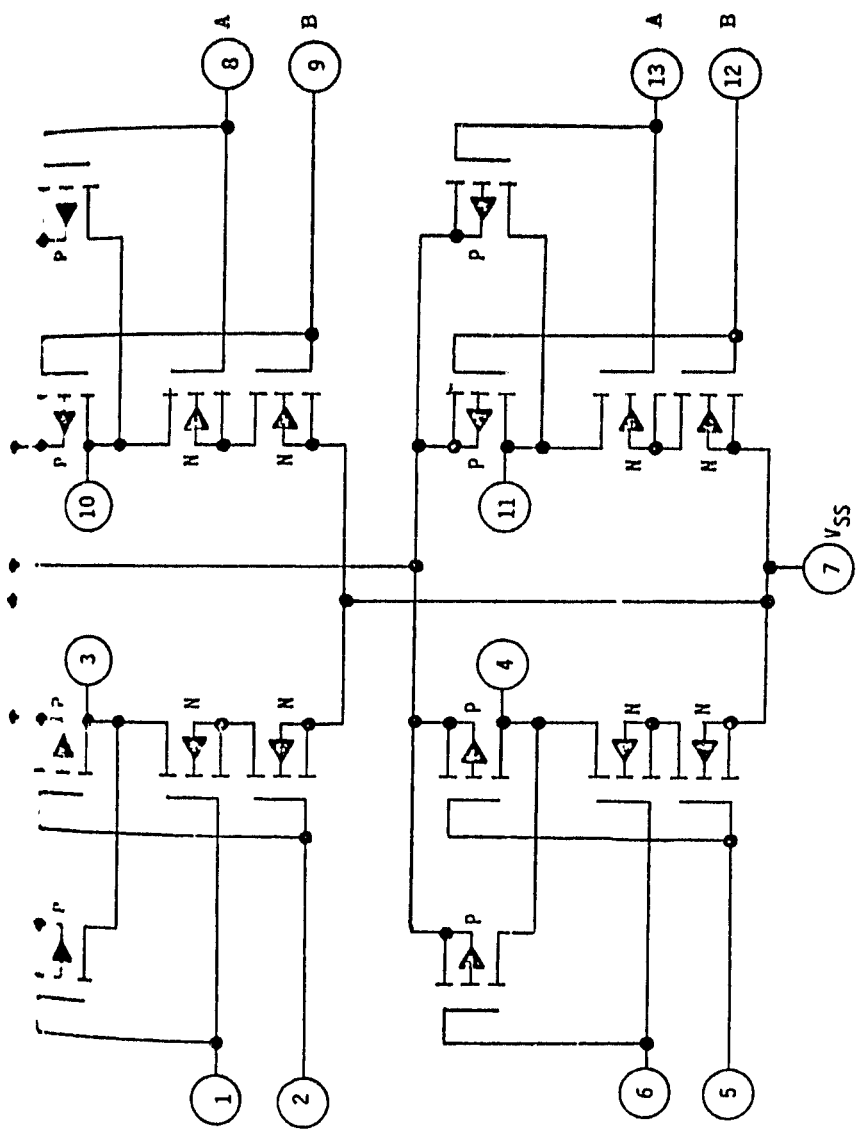

Figure 18. CD4011A dual input NAND gates.

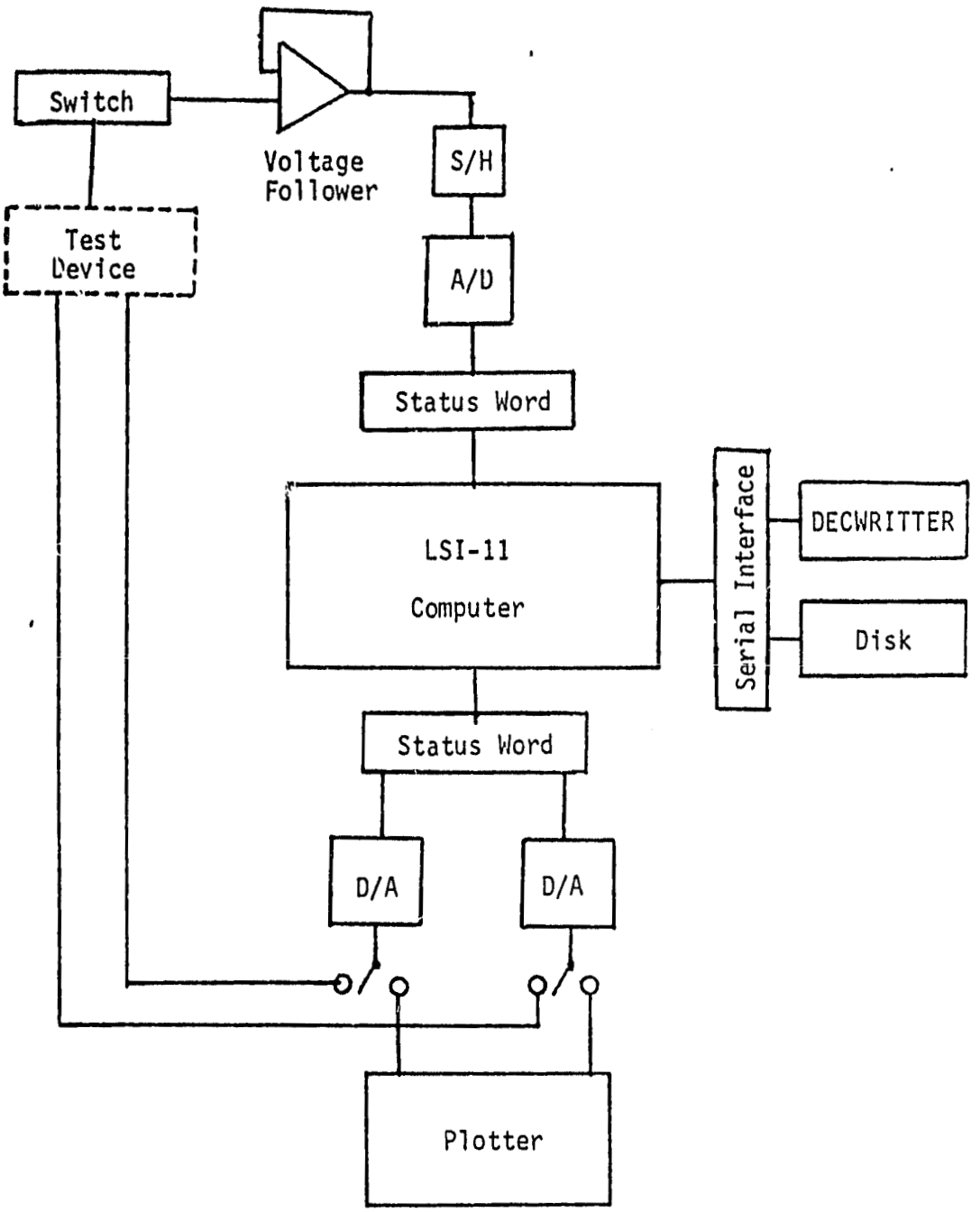

Figure 19. Block diagram of computer and peripheral equipment.

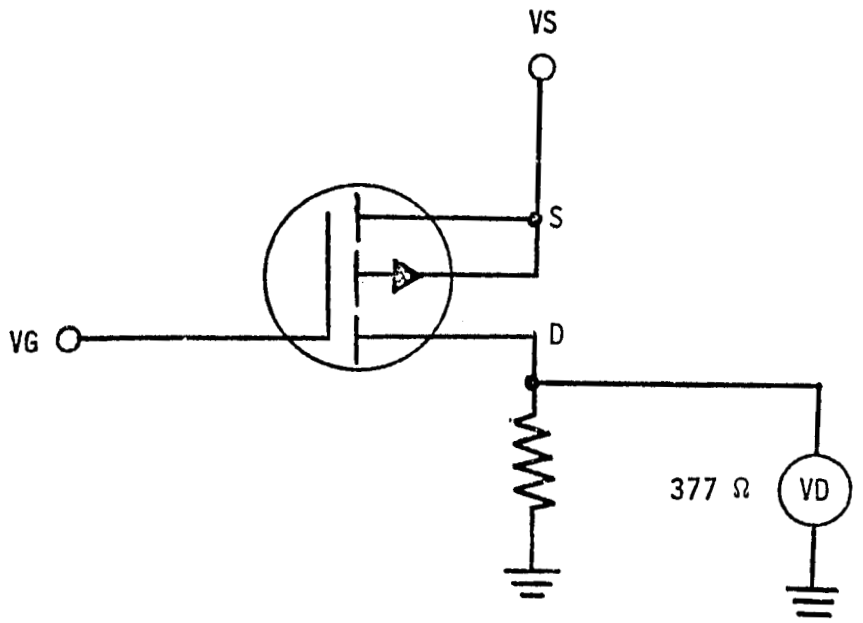

a. P-channel

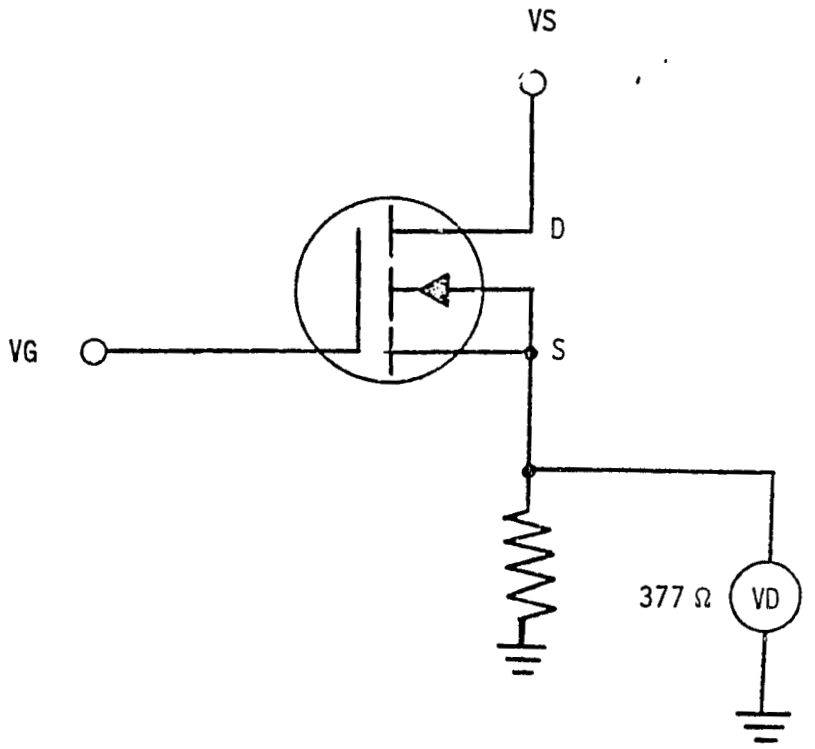

b. N-channel

Figure 20. Electronic configuration during irradiation.

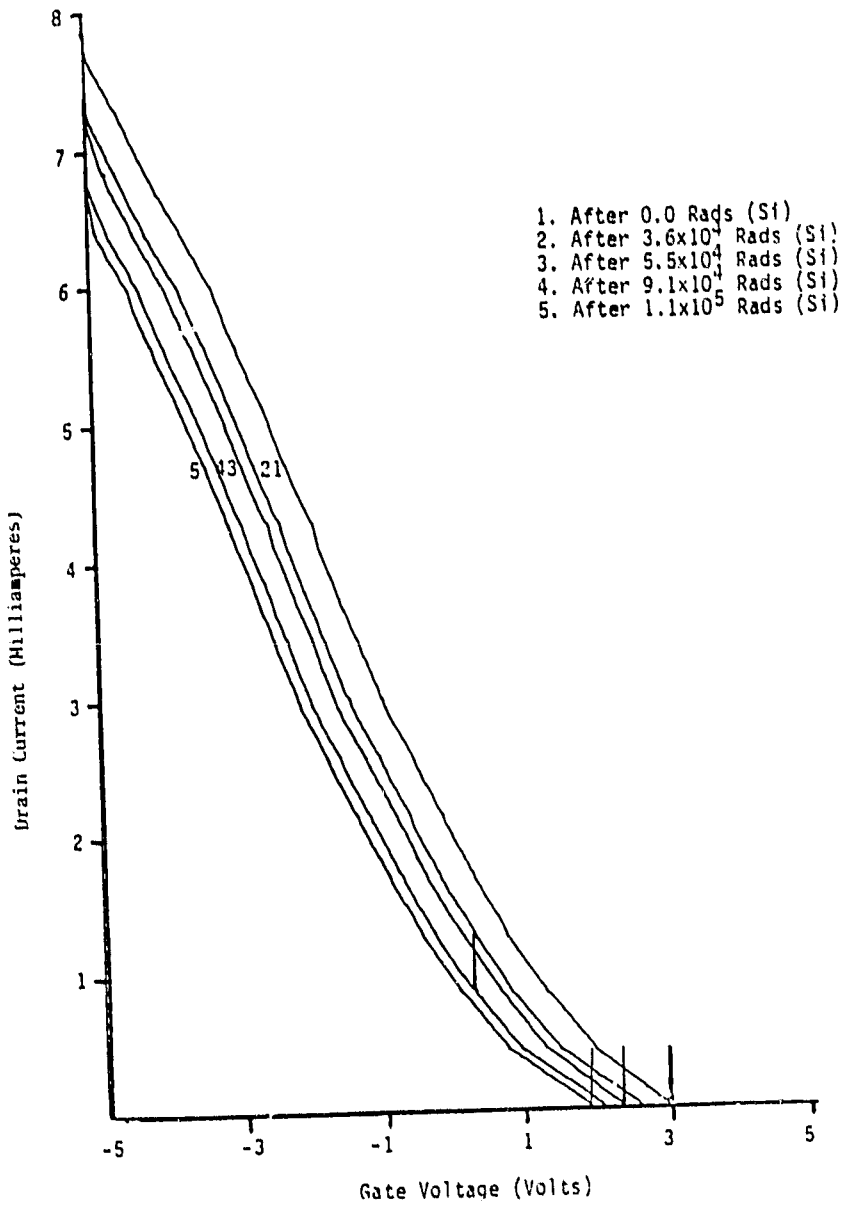

Figure 21. Drain current vs. gate voltage characteristics during irradiation of a 2N-4352 MOSFET.

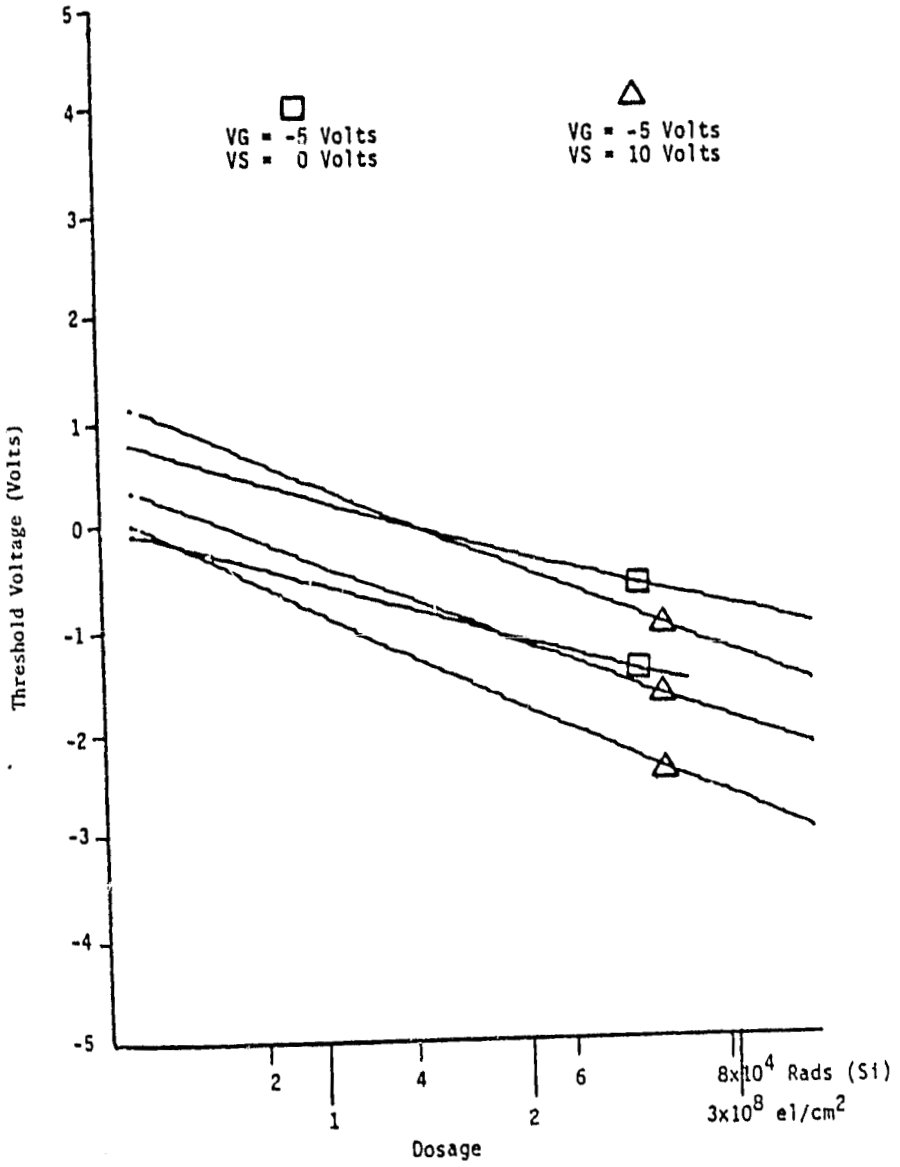

Figure 22. Threshold voltage of p-channel vs. dosage for specified bias voltages.

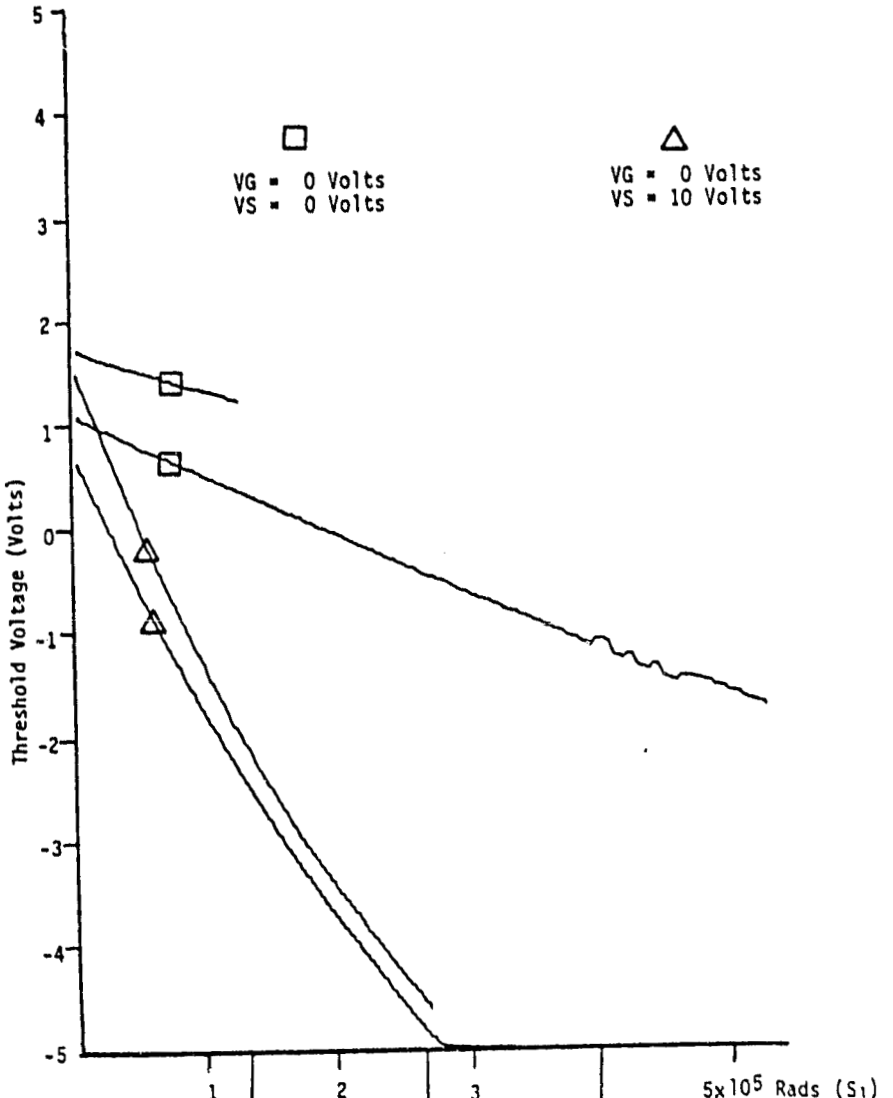

Figure 23. Threshold voltage of p-channel vs. dosage for specified bias voltages.

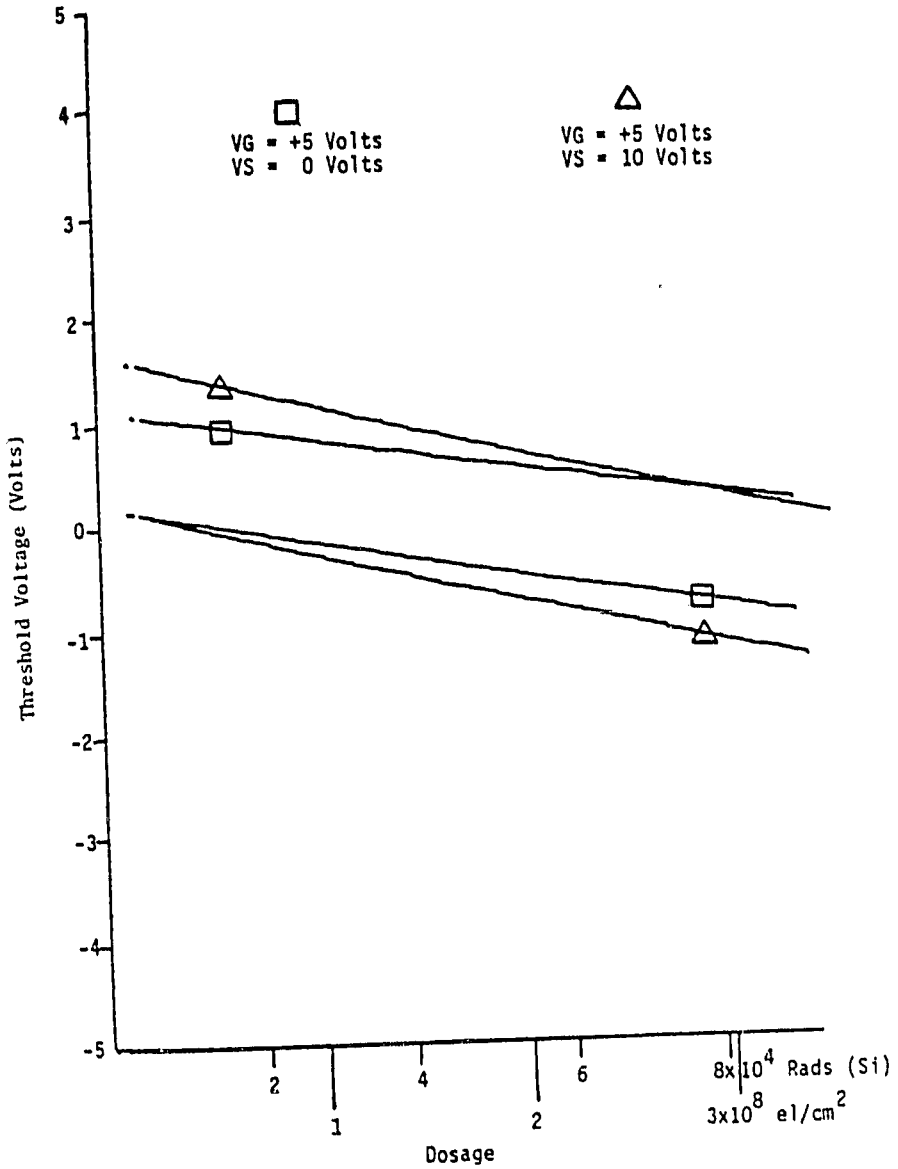

Figure 24. Threshold voltage of p-channel vs. dosage for specified bias voltages.

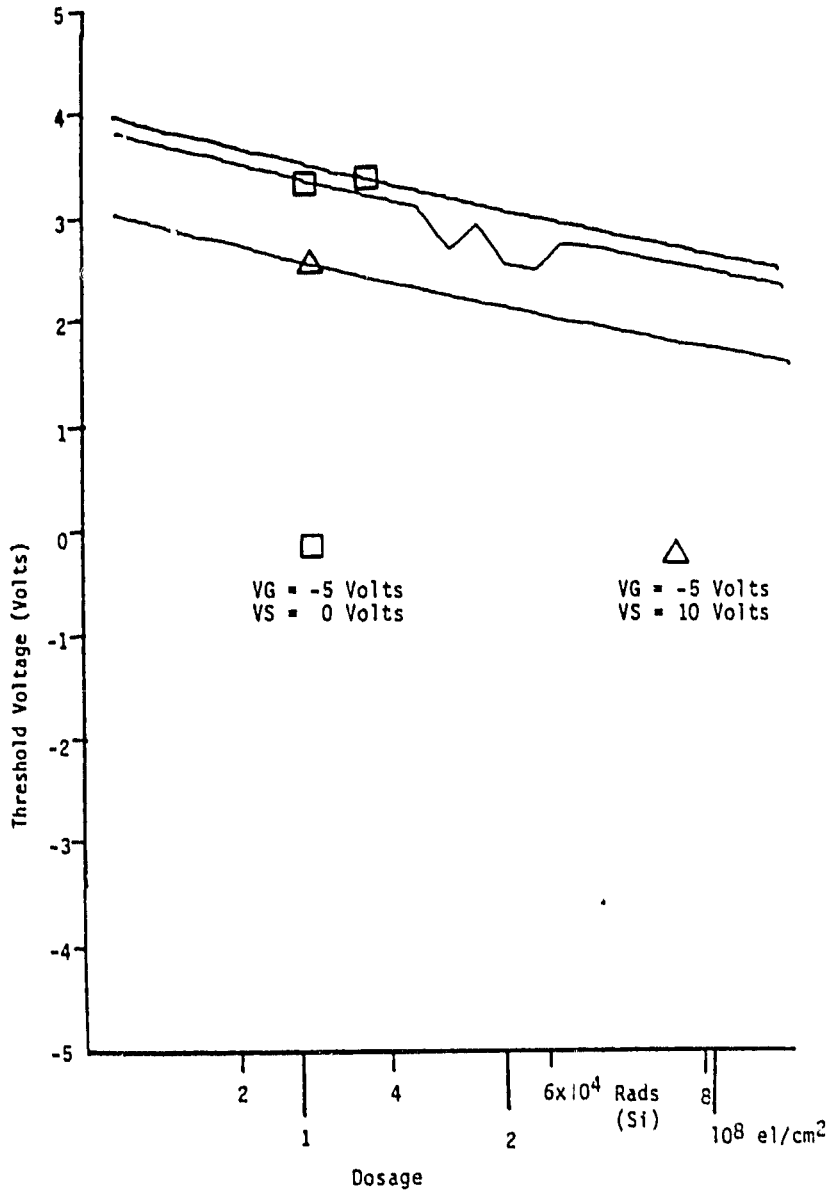

Figure 25. Threshold voltage of n-channel vs. dosage for specified bias voltages.

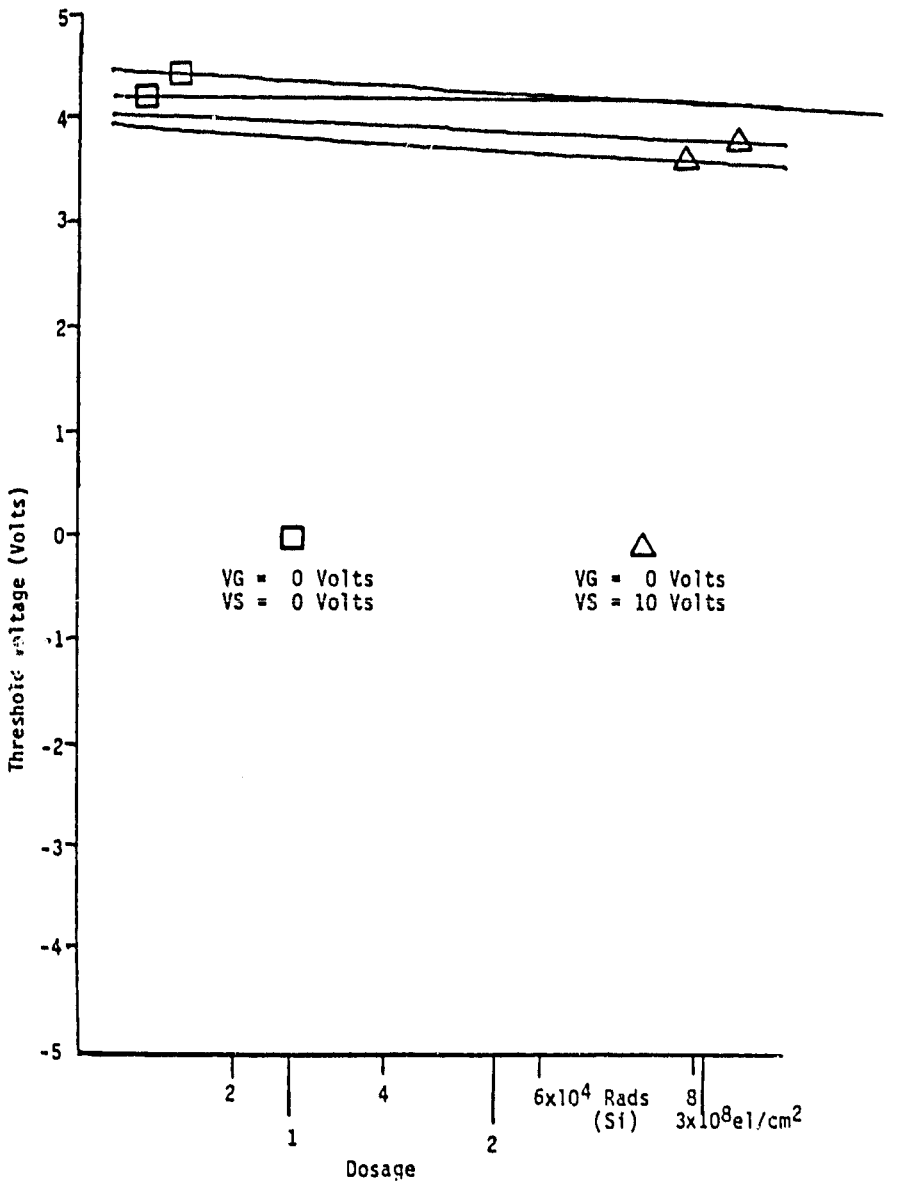

Figure 26. Threshold voltage of n-channel vs. dosage for specified bias voltages.

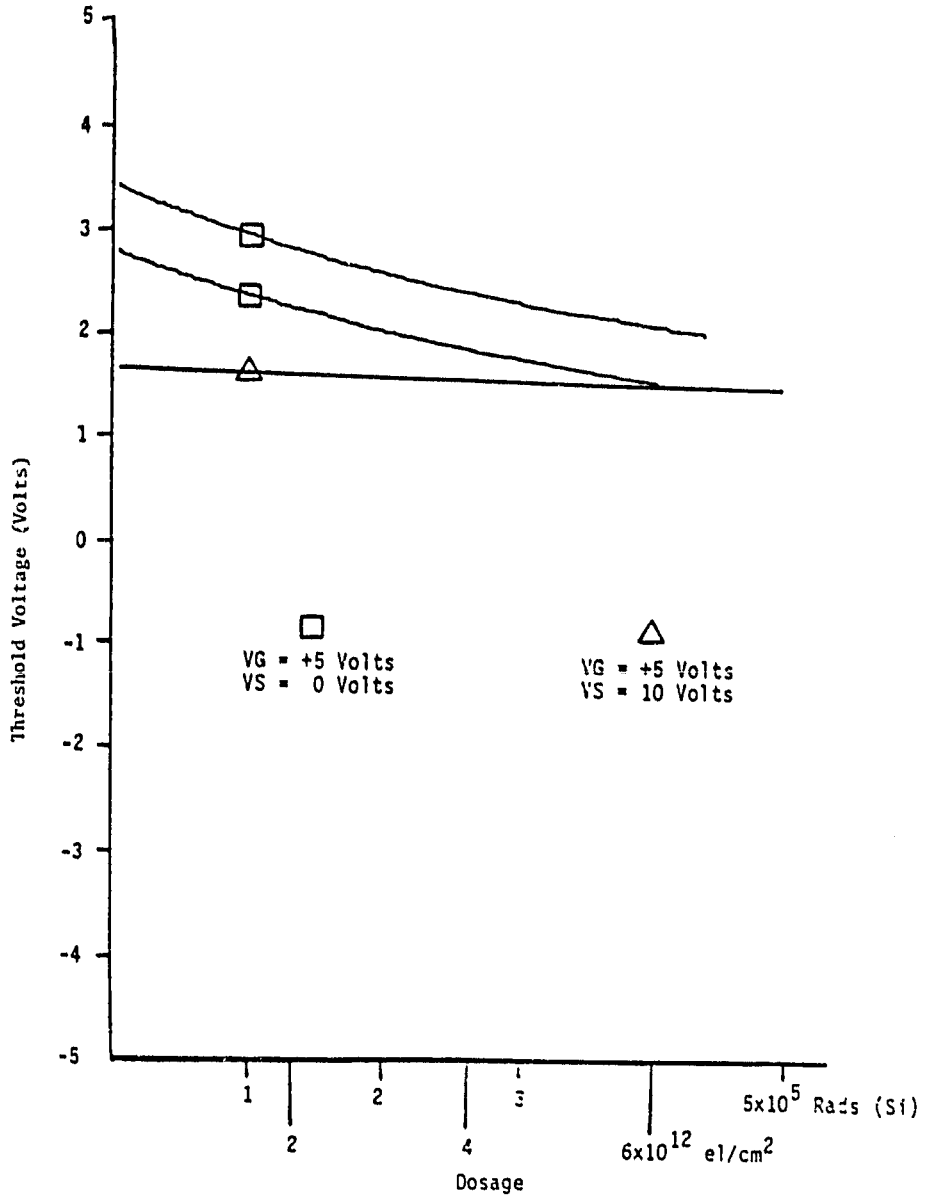

Figure 27. Threshold voltage of n-channel vs. dosage for specified bias voltages.

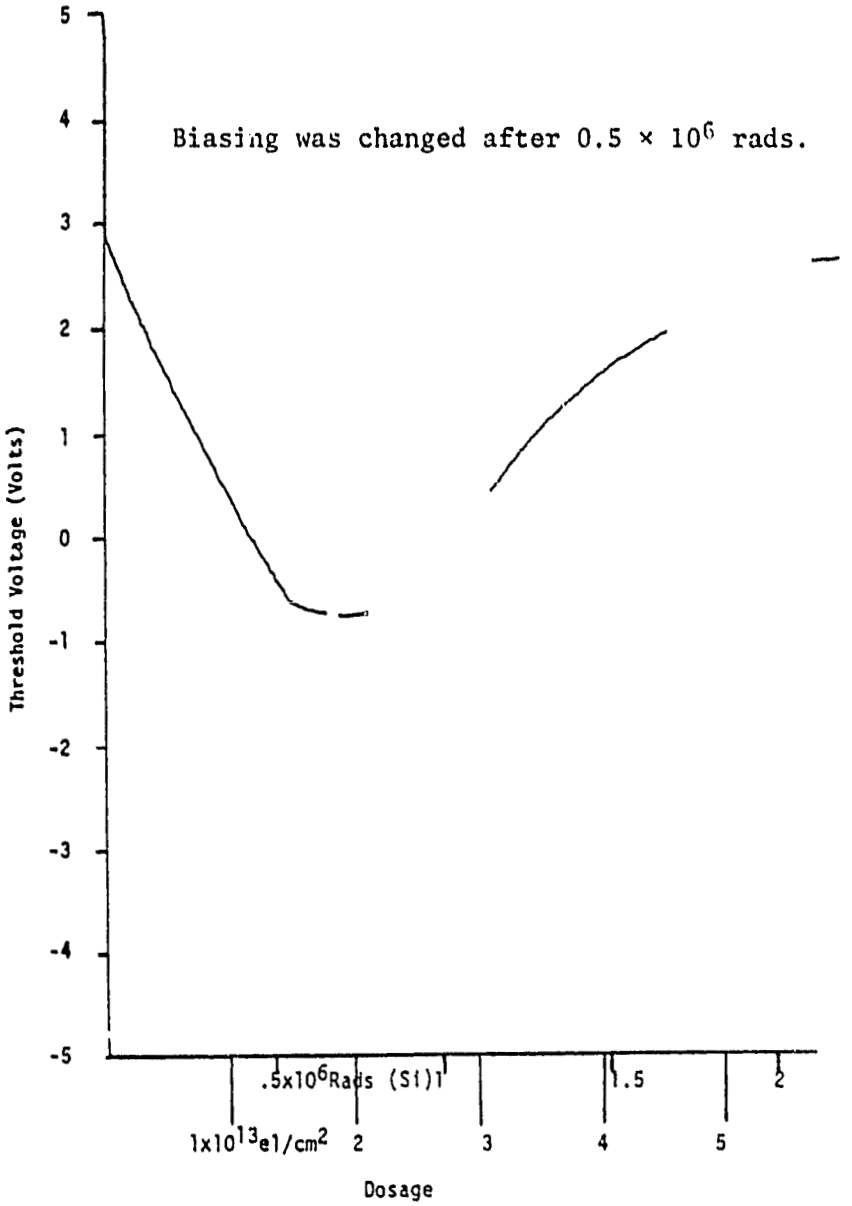

Figure 28. Threshold change in n-channel with irradiation anneal.

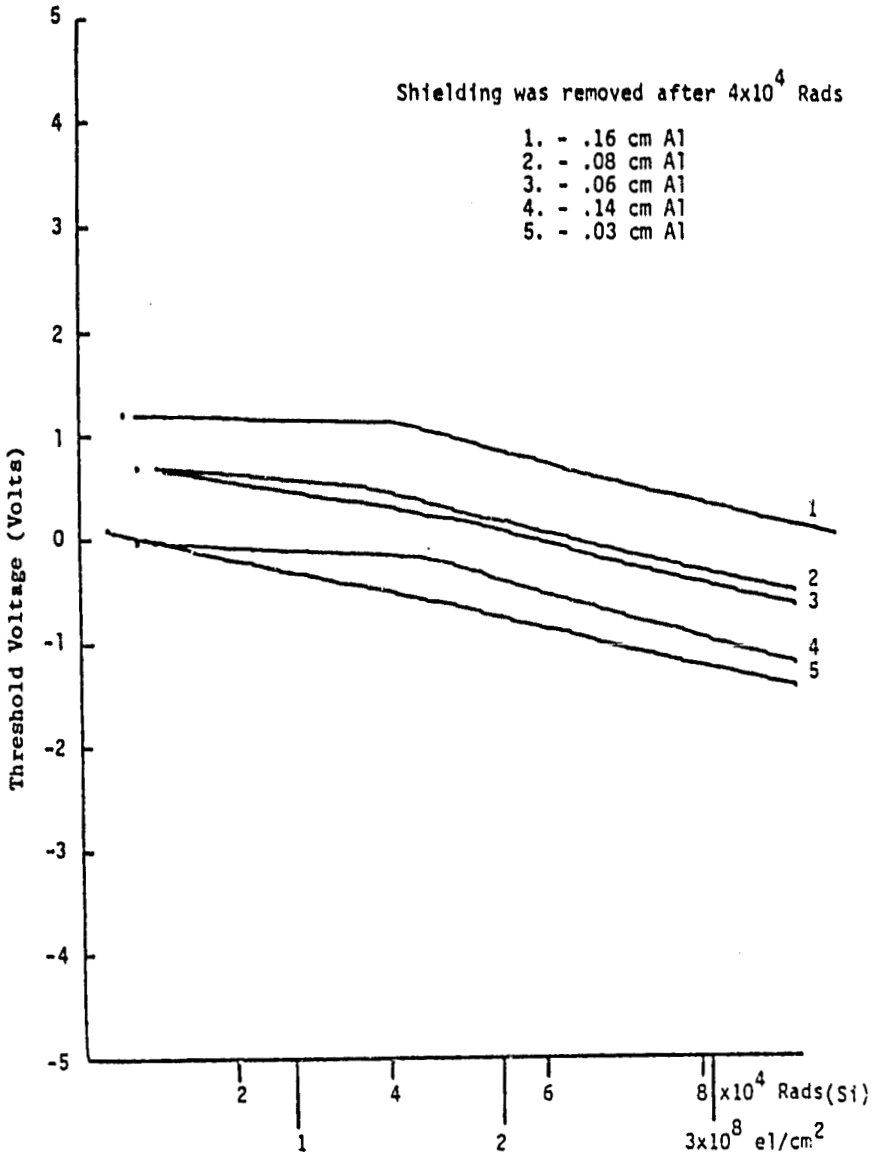

Figure 29. Threshold changes in p-channel due to irradiation using various thicknesses of aluminum shielding.

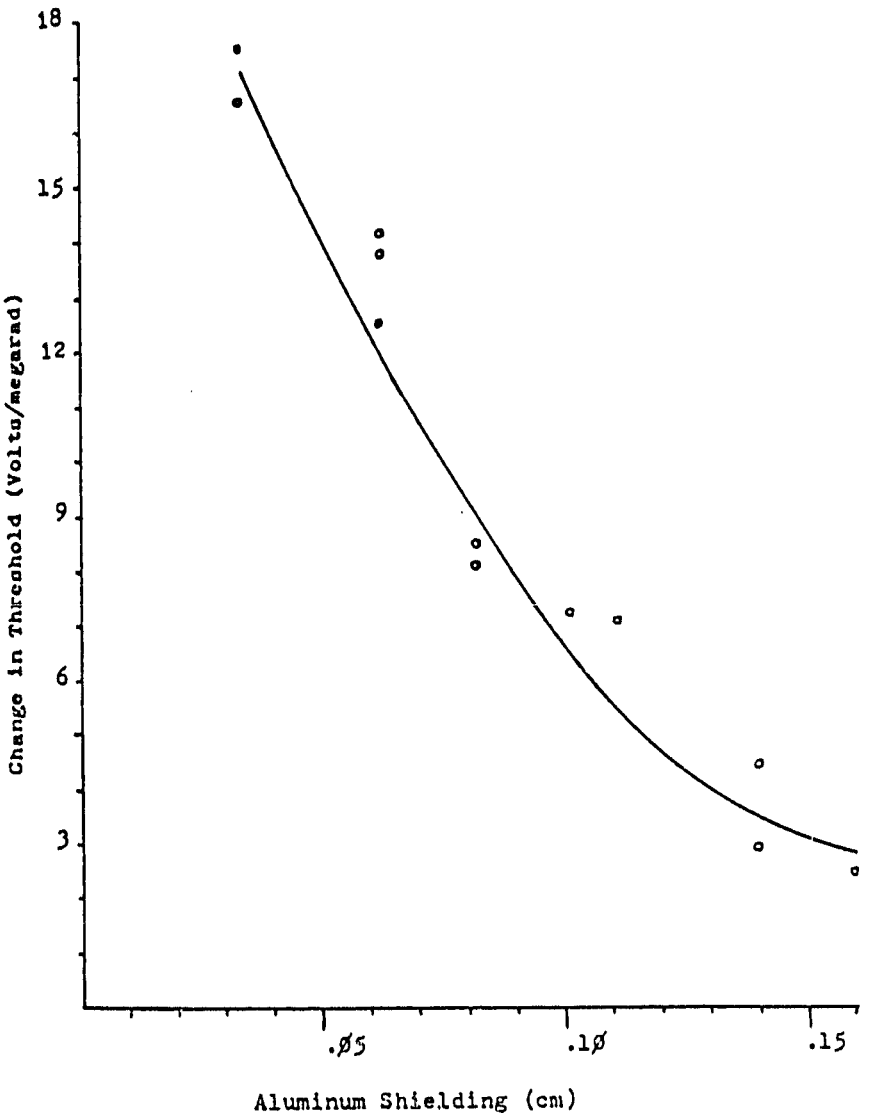

Figure 30. Rate of change of threshold voltage using various thicknesses of aluminum shielding.

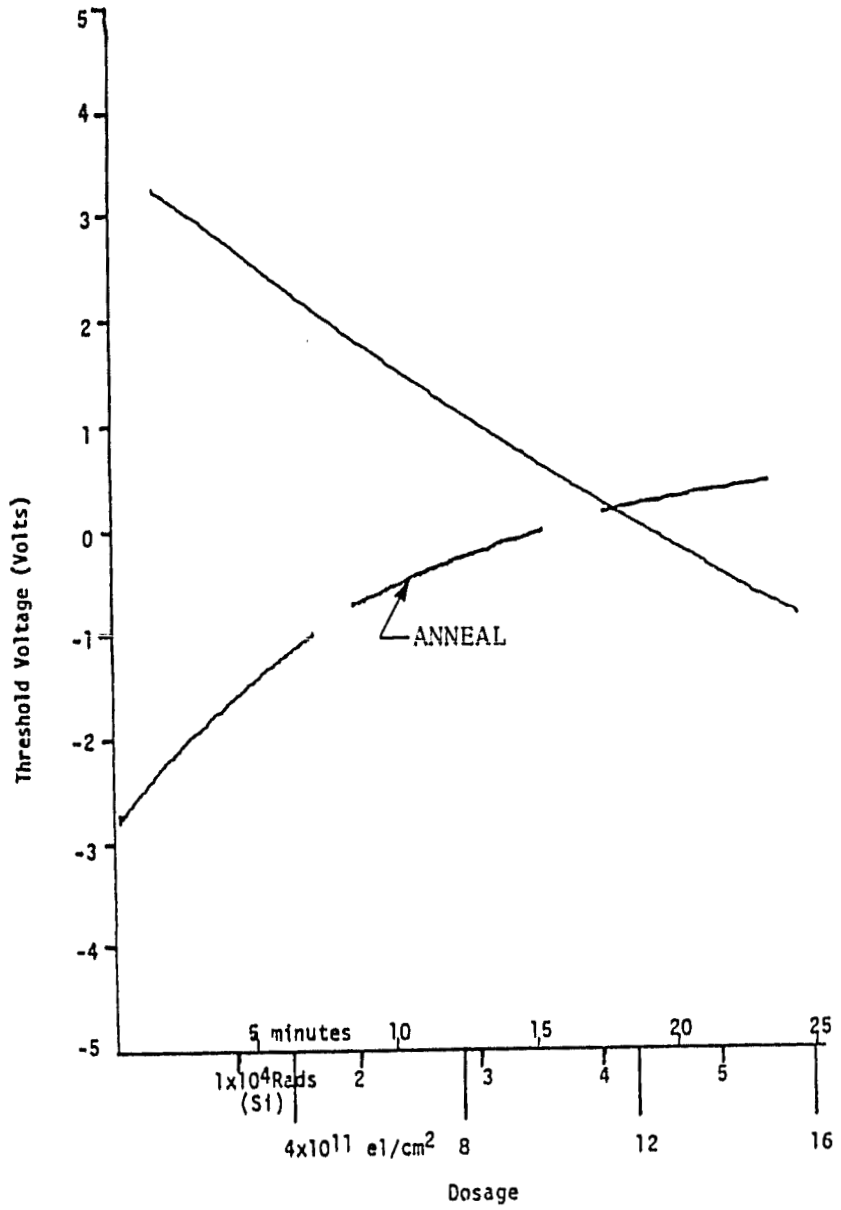

Figure 31. Threshold change in p-channel with ultraviolet light anneal.

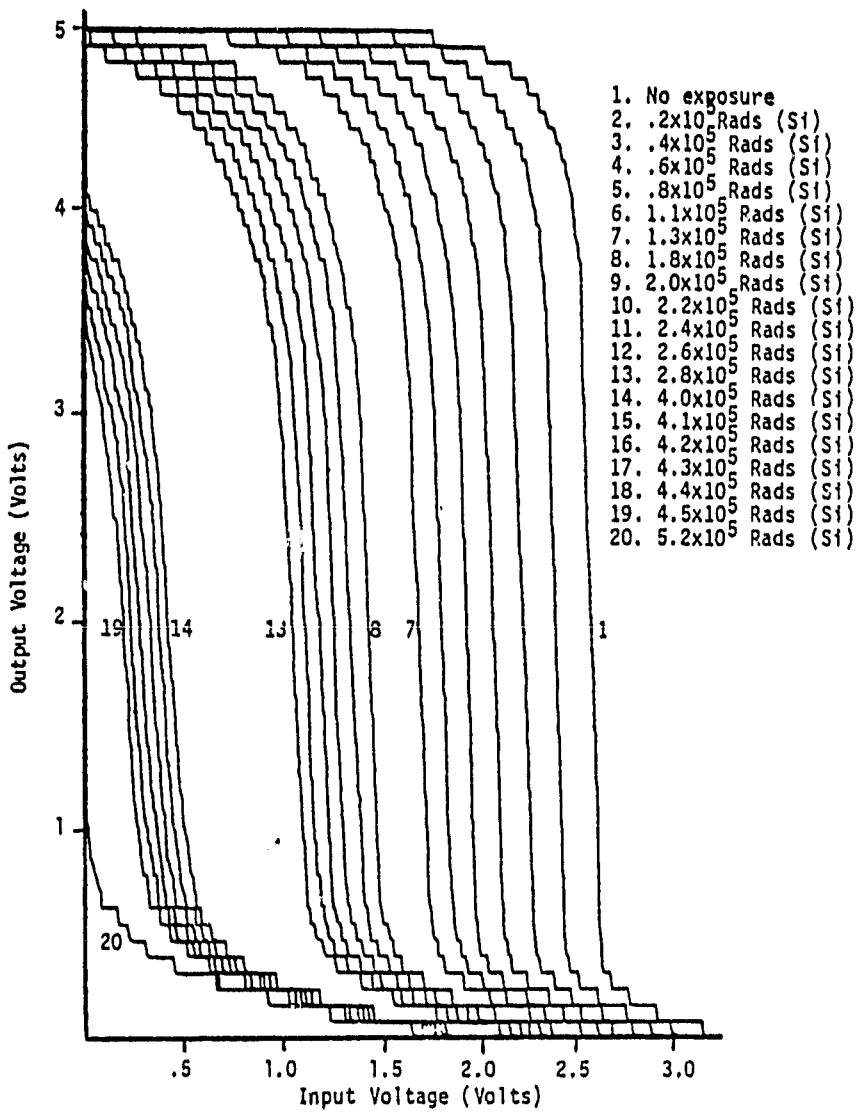

Figure 32. CD4011AE NAND gate switching characteristics during irradiation.

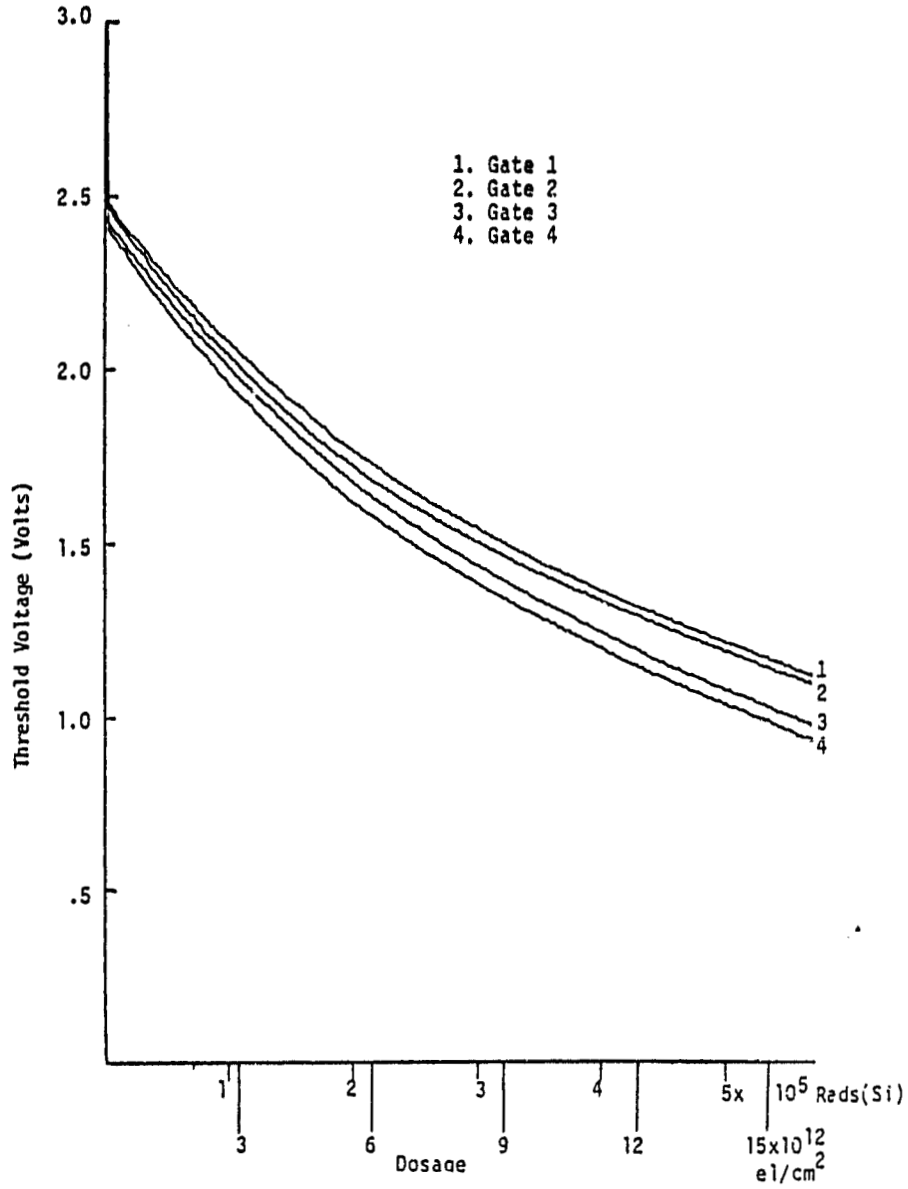

Figure 33. Threshold voltages of the four NAND gates of a CD4011AE during irradiation.

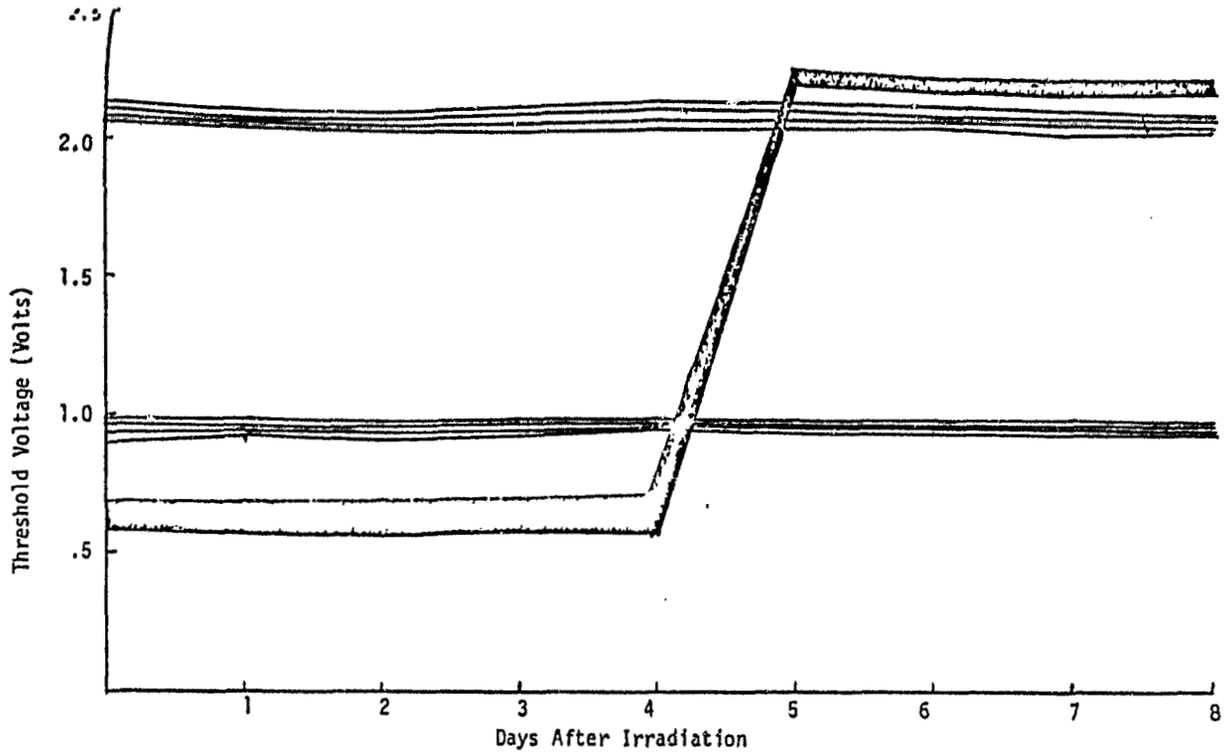

Figure 34. CD4011AE NAND gate threshold voltages after irradiation.

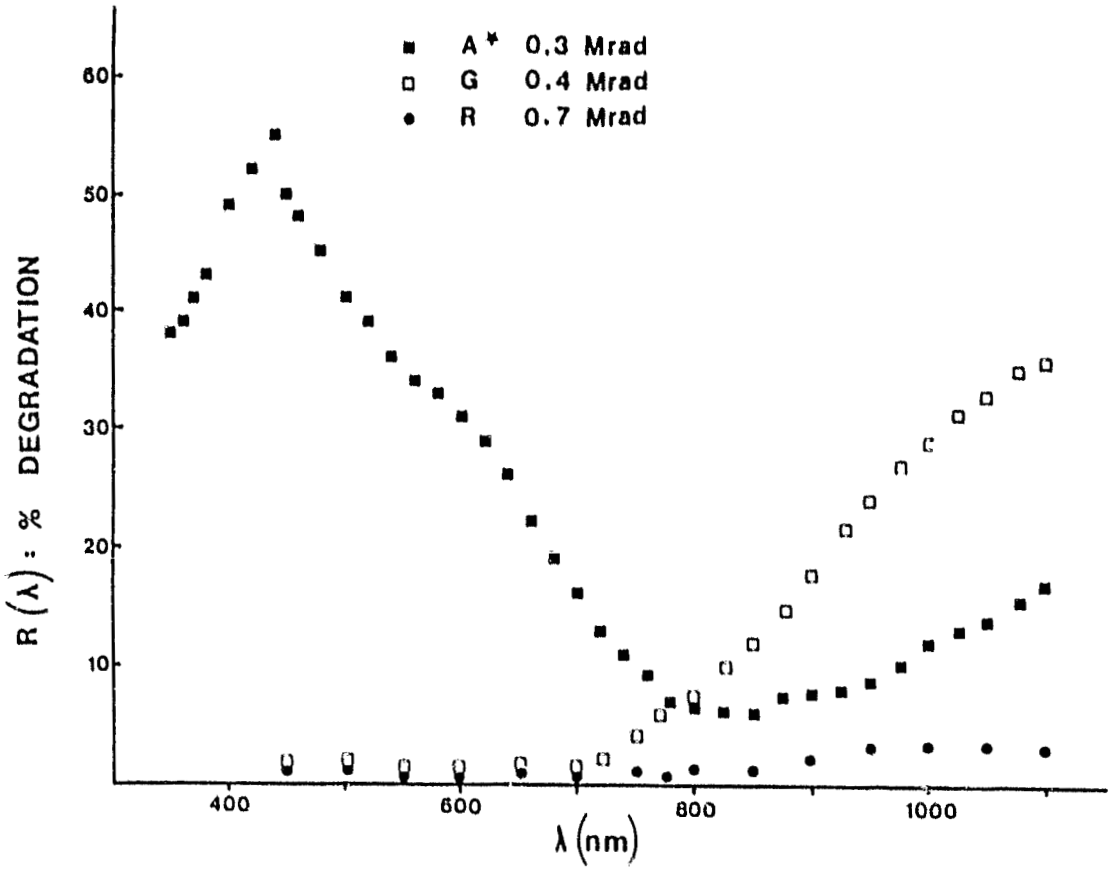

Figure 35. The effect of electron irradiation on the spectral response of various types of PIN photodiode.

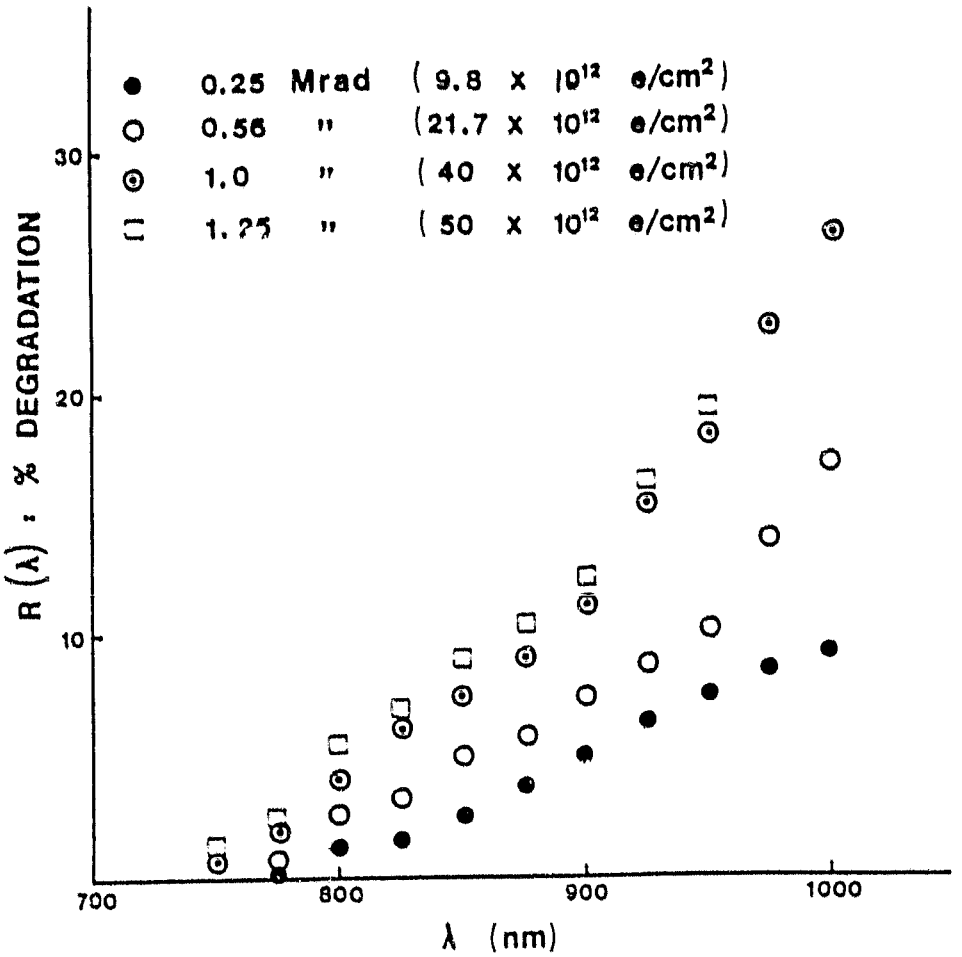

Figure 36. Degradation in spectral response with increasing fluence for photodiodes of type A, B, or G.

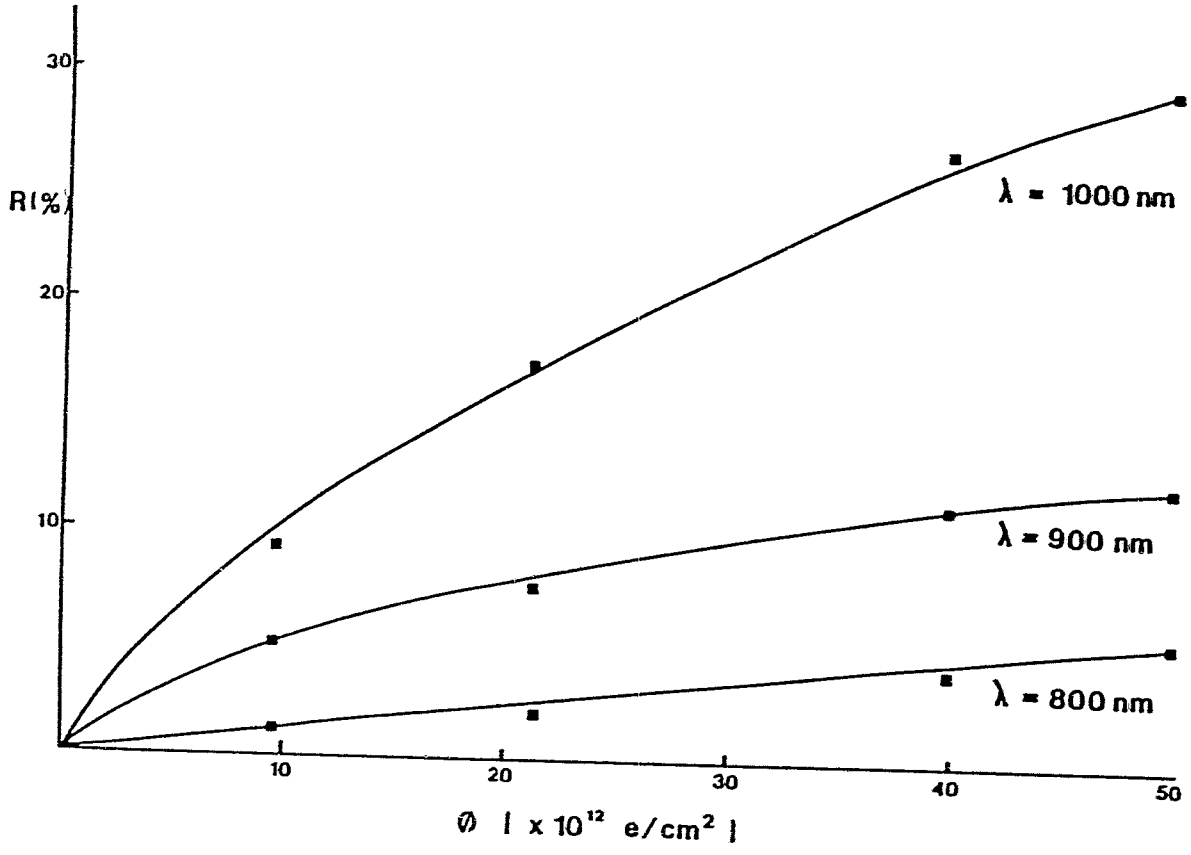

Figure 37. Irradiation-induced degradation of a typical PIN diode at selected wavelengths.

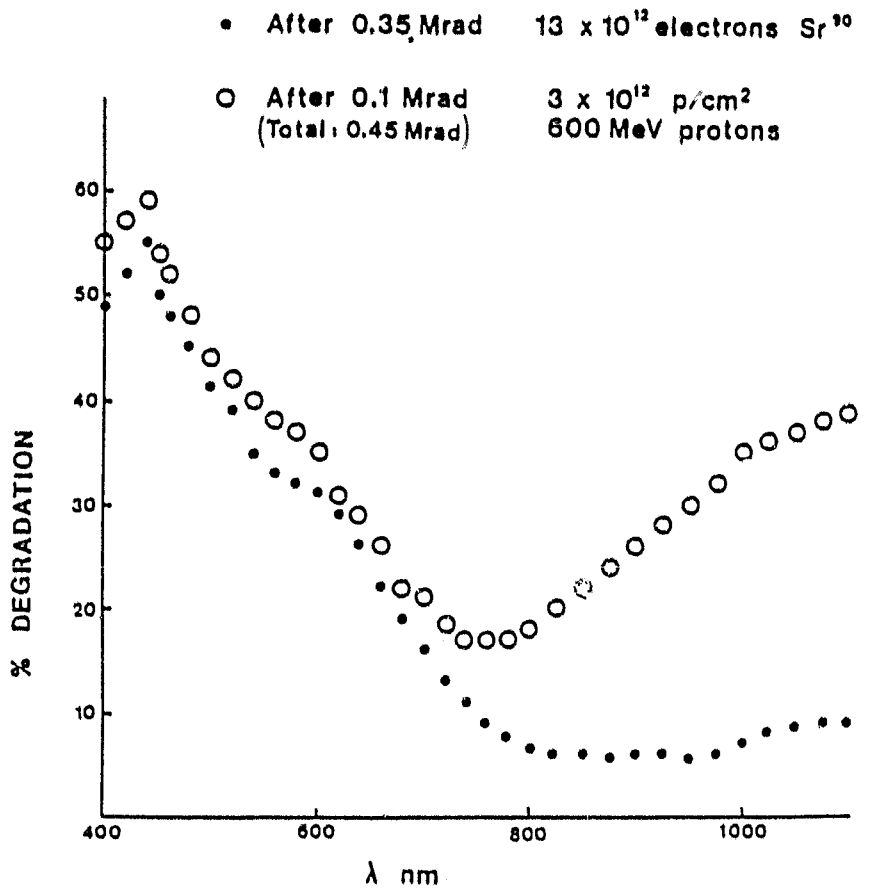

Figure 38. The effects of electron and proton irradiation on the spectral response of type A samples with 7052 glass window.

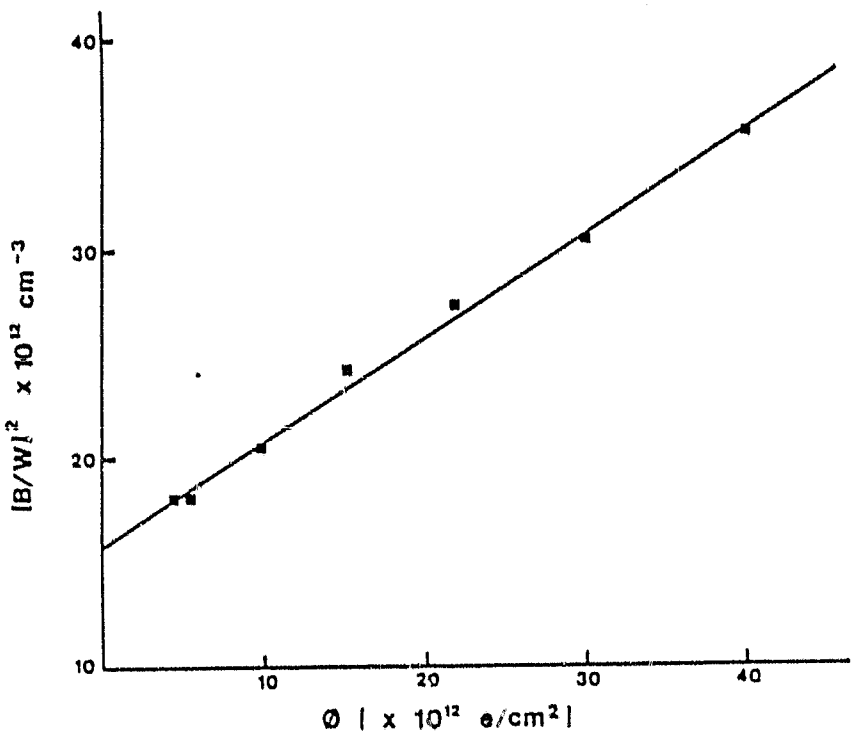

Figure 39. Experimental results used to determine impurity doping density for PIN photodiodes.

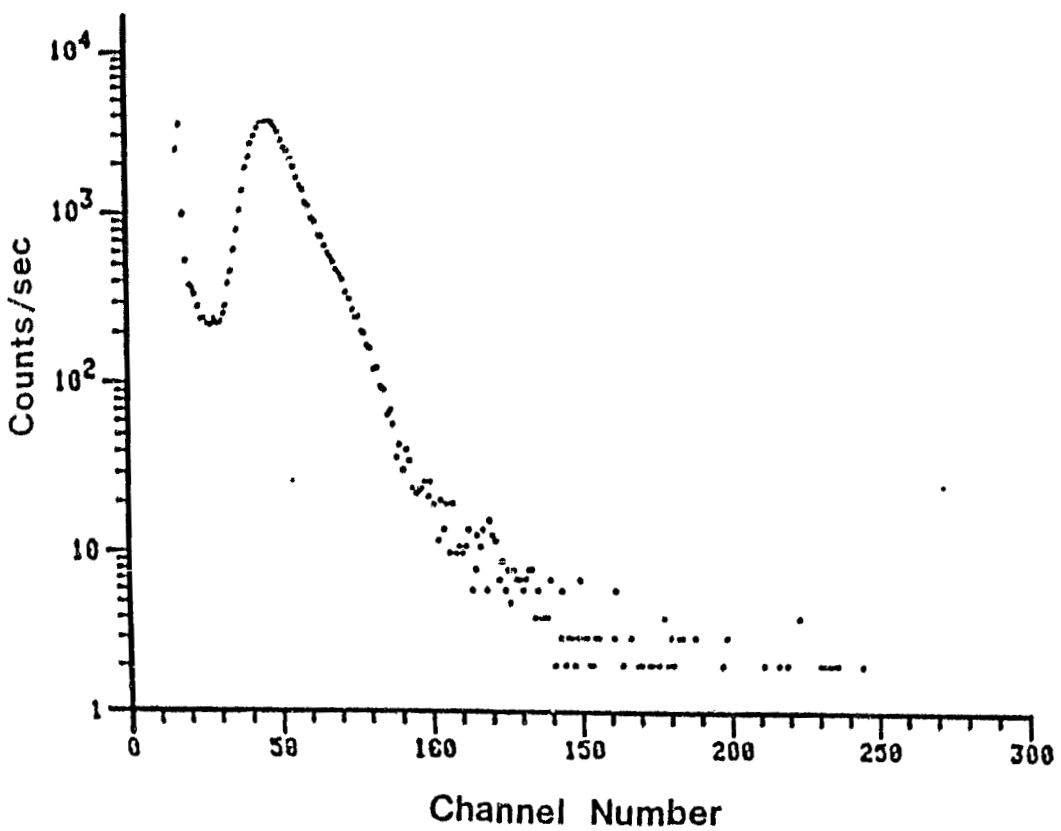

Figure 40. The pulse height spectrum of pulses induced in a Centronic PIN photodiode irradiated with 50-MeV protons.

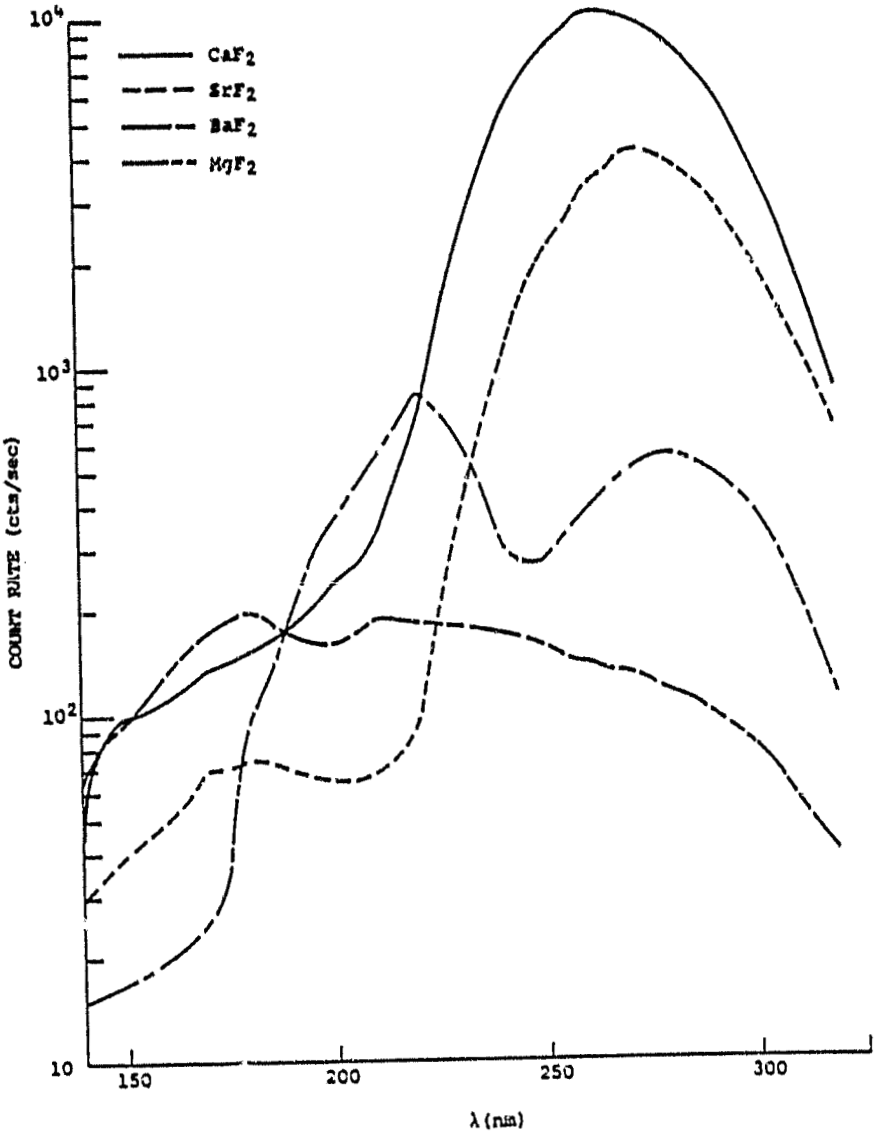

Figure 41. Electron-induced fluorescence of Group IIA—fluoride compounds.

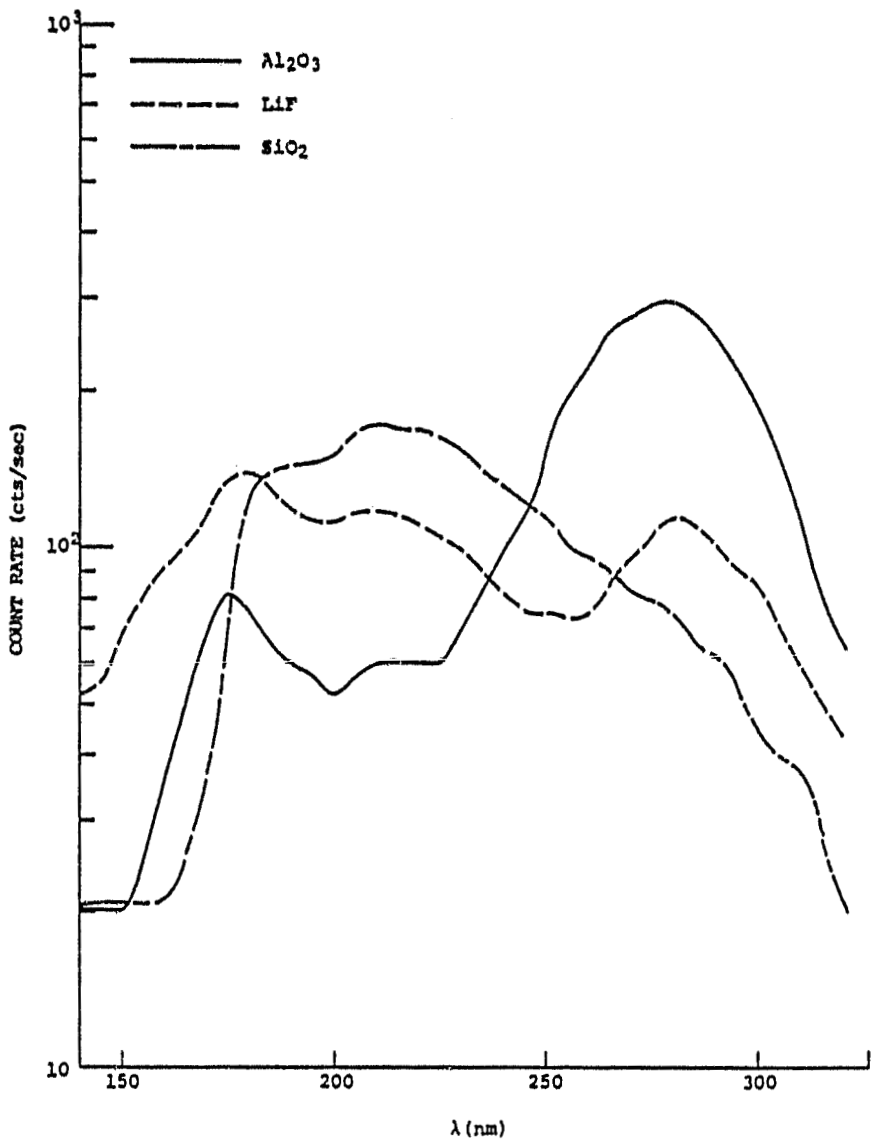

Figure 42. Electron-induced fluorescence spectra of some optical windows.